

INFORMATION TO USERS

This manuscript has been reproduced from the microfilm master. UMI films the text directly from the original or copy submitted. Thus, some thesis and dissertation copies are in typewriter face, while others may be from any type of computer printer.

The quality of this reproduction is dependent upon the quality of the copy submitted. Broken or indistinct print, colored or poor quality illustrations and photographs, print bleedthrough, substandard margins, and improper alignment can adversely affect reproduction.

In the unlikely event that the author did not send UMI a complete manuscript and there are missing pages, these will be noted. Also, if unauthorized copyright material had to be removed, a note will indicate the deletion.

Oversize materials (e.g., maps, drawings, charts) are reproduced by sectioning the original, beginning at the upper left-hand corner and continuing from left to right in equal sections with small overlaps. Each original is also photographed in one exposure and is included in reduced form at the back of the book.

Photographs included in the original manuscript have been reproduced xerographically in this copy. Higher quality 6" x 9" black and white photographic prints are available for any photographs or illustrations appearing in this copy for an additional charge. Contact UMI directly to order.

UMI

A Bell & Howell Information Company
300 North Zeeb Road, Ann Arbor MI 48106-1346 USA
313/761-4700 800/521-0600

UNIVERSITY OF OKLAHOMA

GRADUATE COLLEGE

ADVANCES IN ACOUSTIC STRESS CHARACTERIZATION

A Dissertation

SUBMITTED TO THE GRADUATE FACULTY

in partial fulfillment of the requirements for the

degree of

Doctor of Philosophy

By

JIANG LIQIANG

Norman, Oklahoma

1998

UMI Number: 9905627

UMI Microform 9905627
Copyright 1998, by UMI Company. All rights reserved.

**This microform edition is protected against unauthorized
copying under Title 17, United States Code.**

UMI
300 North Zeeb Road
Ann Arbor, MI 48103


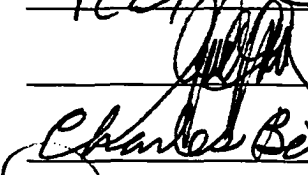
© Copyright by JIANG LIQIANG 1998

All Right Reserved.

ADVANCES IN ACOUSTIC STRESS CHARACTERIZATION

A Dissertation APPROVED FOR THE
SCHOOL OF AEROSPACE AND MECHANICAL ENGINEERING

BY



Charles Bert
Wain M. Eglen
Richard Land

ACKNOWLEDGMENTS

I would like to express my deep sense of gratitude to my advisor, Dr. Ronald A. Kline, for his patience, support, guidance, inspiration, challenge, and the wealth of information he has shared during the entire period of my graduate studies at the University of Oklahoma.

A special debt of gratitude is owed to Dr. Alfred G. Striz for his willingness to be the co-chair of my advisory committee, for carefully reading and correcting my original manuscript, and for providing valuable suggestions on this dissertation.

I would also like to express my sincere appreciation to Dr. Charles W. Bert, Dr. Davis M. Egle, and Dr. Landes for their serving on my advisory committee, teaching me relevant background courses, providing valuable advice for my studies, especially giving me support and trust in many aspects of life.

A special thanks is extended to Dr. Eva Drescher-Krasicka who initiated the idea of the scanning acoustic microscopy approach and provided support and experimental images for this dissertation.

I am greatly indebted to my wife Lianglin, my parents, as well as my other family members; no words can adequately describe my thankfulness for their constant understanding, love, sacrifice, and unprecedented emotional support. It is to them I dedicate my education.

Finally, with grateful heart, I submit my humble work to the Almighty God without whose guidance and blessing none of this could have been possible.

TABLE OF CONTENTS

	page
LIST OF FIGURES	vii
LIST OF TABLES	ix
ABSTRACT	x
 Chapter	
I. INTRODUCTION	1
II. THEORY OF ACOUSTOELASTICITY	14
III. A NEW SCANNING ACOUSTIC MICROSCOPY APPROACH TO IN-PLANE STRESS ANALYSIS	33
IV. USING RAYLEIGH WAVE DISPERSION TO CHARACTERIZE IN-PLANE STRESSES	72
V. CONCLUSIONS	108
REFERENCES	111
APPENDIX A RAYLEIGH WAVE DISPERSION EQUATIONS	118
APPENDIX B STRESS RESULTS OF FEA SIMULATION	127

LIST OF FIGURES

	page
Fig. 2.1 Coordinates for a material point at the natural, initial, and final configurations of a predeformed body	16
Fig. 3.1 Schematic diagram of acoustic microscopy	41
Fig. 3.2 Experimental loading facilities	43
Fig. 3.3 Wave propagation diagram	43
Fig. 3.4 FEA model for diametrically compressed disk	46
Fig. 3.5 Scanning acoustic microscopy image of a diametrically compressed disk ($P = 716 \text{ N}$) (Drescher-Krasicka, NIST)	50
Fig. 3.6 Scanning acoustic microscopy image of a diametrically compressed disk ($P = 910 \text{ N}$) (Drescher-Krasicka, NIST)	51
Fig. 3.7 Scanning acoustic microscopy image of a diametrically compressed disk ($P = 1110 \text{ N}$) (Drescher-Krasicka, NIST)	52
Fig. 3.8 Scanning acoustic microscopy image of a diametrically compressed disk ($P = 1310 \text{ N}$) (Drescher-Krasicka, NIST)	53
Fig. 3.9 Scanning acoustic microscopy image of a diametrically compressed disk ($P = 1510 \text{ N}$) (Drescher-Krasicka, NIST)	54
Fig. 3.10 Scanning acoustic microscopy image of a diametrically compressed disk ($P = 1700 \text{ N}$) (Drescher-Krasicka, NIST)	55

Fig. 3.11 Quantitative comparison between simulation and experimental results ($P = 716 \text{ N}$)	56
Fig. 3.12 Quantitative comparison between simulation and experimental results ($P = 910 \text{ N}$)	57
Fig. 3.13 Quantitative comparison between simulation and experimental results ($P = 1110 \text{ N}$)	58
Fig. 3.14 Quantitative comparison between simulation and experimental results ($P = 1310 \text{ N}$)	59
Fig. 3.15 Quantitative comparison between simulation and experimental results ($P = 1510 \text{ N}$)	60
Fig. 3.16 Quantitative comparison between simulation and experimental results ($P = 1700 \text{ N}$)	61
Fig. 3.17 Errors introduced using perturbation theory compared with full field theory	65
Fig. 3.18 Stress comparison between FEA and analytical solution for 716 N compressing load	66
Fig. 3.19 Stress comparison between FEA and analytical solution for 910 N compressing load	66
Fig. 3.20 Stress comparison between FEA and analytical solution for 1110 N compressing load	67
Fig. 3.21 Stress comparison between FEA and analytical solution	

for 1310 N compressing load	67
Fig. 3.22 Stress comparison between FEA and analytical solution	
for 1510 N compressing load	68
Fig. 3.23 Stress comparison between FEA and analytical solution	
for 1700 N compressing load	68
Fig. 3.24 Stress comparison between FEA and analytical solution	
for 1700 N compressing load	69
Fig. 4.1 Surface wave over a deformed half space	74
Fig. 4.2 Dispersion of Rayleigh waves for different surface strains	94
Fig. 4.3 Dispersion of Rayleigh waves for different linear coefficients	
of strain distribution	95
Fig. 4.4 Dispersion of Rayleigh waves for different quadratic coefficients	
of strain distribution	96
Fig. 4.5 Surface strain field reconstruction using Rayleigh waves of	
1, 5, and 10 MHz	97
Fig. 4.6 Linear strain field reconstruction using Rayleigh waves of	
1, 5, and 10 MHz	98
Fig. 4.7 Quadratic strain field reconstruction using Rayleigh waves of	
1, 5, and 10 MHz	99
Fig. 4.8 Surface strain field reconstruction using Rayleigh waves of	
2, 3 and 5 MHz	100

Fig. 4.9	Linear strain field reconstruction using Rayleigh waves of	
	2, 3 and 5 MHz	101
Fig. 4.10	Quadratic strain field reconstruction using Rayleigh waves of	
	2, 3 and 5 MHz	102

LIST OF TABLES

Table. 3.1	Material properties of aluminum alloy 6061-T6	44
Table. 4.1	Material properties of a mild steel	93
Table. 4.2	Wave length of Rayleigh waves corresponding to	
	certain frequencies	104

ABSTRACT

As a promising tool to characterize residual stresses in engineering structural components, acoustoelasticity has been the subject of a great deal of research over the past forty years. Although considerable achievements have been made, most approaches to ultrasonic stress analysis are limited in their utility due to their reliance on contact shear wave transducers which preclude the ability of scanning large areas, their inability to resolve the dependence of stress on depth, and their difficulties in taking accurate time delay measurements, resulting from coupling problems and the very small acoustoelastic effect observed for most practical materials. Recently, Drescher-Krasicka conducted a series of experiments to illustrate how scanning acoustic microscopy can be used to characterize applied and residual stresses by monitoring the peak amplitudes of the resultant signals of shear waves produced by mode conversion. In this study, a theoretical study and numerical simulations are performed to provide a quantitative correlation with the experiment results so as to lay a theoretical foundation and enhance the understanding for this new scanning technique. Based on the theory of finite deformations and the equation of motion, Christoffel equations in the presence of strains are derived. They are solved with first order perturbation theory to determine the two quasi-shear wave velocities. The acoustic microscope lens is modeled as launching a strong axisymmetric longitudinal lobe at oblique incidence. Two shear waves polarized in the directions of the

in-plane principal stress axes will be simultaneously generated by mode conversion at the water-specimen interface. Due to the constructive-destructive interference between the signals of the shear waves, the amplitude of the combined signal of the acoustic microscope turns out to be very sensitive to small changes in acoustic velocity produced by local stresses. The numerical simulation shows good agreement with the experimental results for a diametrically loaded disk case.

Another effort in this study is devoted to employing Rayleigh waves with a line-focused acoustic microscope to characterize the through-thickness residual stress distribution. Assuming the principal strain directions are known and strains are polynomially distributed with depth while uniform in the other directions, equations for the Rayleigh wave velocity change versus the initial static stress are derived with a first order perturbation approach. This information can be used to reconstruct synthetic in-plane stress distributions from frequency dependent Rayleigh wave velocity data.

CHAPTER I

INTRODUCTION

1.1 *Background Review*

In modern industry, NDE (Nondestructive Evaluation) procedures play an increasingly important role in material processing, product design, the analysis of service-life expectancy, and the quality control of manufactured products. The objective of nondestructive evaluation frequently goes beyond the detection of inhomogeneities because the overall strength of a component depends not only on the presence of an inhomogeneity and its general nature, but also on its location, size, shape, and orientation as well as the stress distribution (applied or residual). However, there is still a lack of a mature technique to characterize residual stresses in a general sense. Conventional X-ray techniques are only suitable for surface stress analysis. Neutron techniques are not feasible for in-field tests. Acoustoelasticity, which is essentially based on the relationship between the stress and the stress induced change in the wave propagation velocity has been considered one of the most promising tools for residual stress measurements and has been the subject of a great deal of research over the past forty years.

1.1.1 *Acoustoelastic Theory*

The earliest treatment of the residual stress problem with acoustoelasticity is attributed to Hughes and Kelly [1]. Assuming the material in stress-free state to be isotropic, they developed an analytical solution to the problem of wave propagation in a stressed solid based on the theory of finite deformations. Their approach resulted in an eigenvalue problem for the plane wave velocities as a function of second and third order elastic constants and strains. Toupin and Bernstein [2] and Thurston and Brugger [3] extended the analyses of Hughes and Kelly to more general cases to determine third order elastic constants in various crystals and isotropic materials. Their work is considered the early version of acoustoelasticity theory.

As acoustoelastic techniques developed, it was soon apparent that the assumption of initially isotropic material was inadequate to describe actual physical situations. Since the acoustoelastic effect is very small (typically the relative change of plane wave speed is $10^{-5}/\text{MPa}$ in aluminum and $10^{-7}/\text{MPa}$ in steel), any weak inhomogeneity and anisotropy in the material, which are usually neglected in the theory of elasticity, could result in large errors in stress measurements. Thus, since the 1970s, theoretical investigations in acoustoelasticity have been focused on developing methods to separate texture and stress induced anisotropy.

In 1973, Iwashimizu and Kubomura [4] developed a plane acoustoelastic method for slightly orthotropic materials, in which the orthotropy of the second order elastic constants are considered but the third order elastic constants are assumed to be isotropic.

In 1981, Okada [5] developed a more general plane acoustoelastic approach for slightly orthotropic materials. By comparing acoustoelasticity theory with anisotropic photoelasticity theory, he derived two equations relating the plane stress components and stress induced wave speed change as well as the acoustic axis rotation. The anisotropy of the material is characterized by three acoustoelastic constants determined by experiment. The breakthrough of the theory lies in the fact that the principal directions do not have to coincide with the texture directions as confines other methods; thus, the method can be used to solve general plane problems. Three years later, Okada [46] proposed adding a S parameter, which is essentially the summation of two shear wave velocities, so as to have three equations to determine three plane stress components. In his previous theory, numerical integration such as the shear-difference method had to be employed to solve for three unknowns with two equations. In 1982, Clark and Mignogna [6] derived the same results as Okada [5], but from a classical elastodynamic point of view.

Although these acoustoelastic theories were successfully used in the measurements of plane applied stresses for slightly orthotropic materials, difficulties remained in their application to residual stress measurements because the acoustoelastic constants determined by calibration samples may differ from those for the actual testing medium. Several other methods of separating the effects of texture and stress have been proposed in the literature.

Arora [7] proposed a scheme of using ultrasonic waves with different frequencies to solve the separation problem. He argued that the relative change in the wave speed

results from both texture and stress: Based on many experimental results, the texture effect is frequency dependent while the stress effect is not, thus, with different frequency shear waves, stress measurements can be accomplished.

A method of oblique incidence of the SH wave was presented by King and Fortunko [8]. With the assumption that the principal stress directions coincide with the principal orthotropic texture directions, the relative difference and summation of the two shear velocities, which are polarized perpendicularly to each other and obliquely incident at the same angle relative to the normal of the surface, are derived as a function of the principal stresses, the acoustoelastic constants, and the incident angle. Thus, texture effects can be separated through measurements with different incident angles.

Thompson, et al., [9] proposed a method of measuring the difference in the velocities of two shear waves whose directions of propagation and polarization have been interchanged for a material of orthotropic anisotropy. The velocity difference gives the principal stress difference independent of the texture anisotropy. Here, the principal stress directions are also assumed to be parallel to the principal orthotropic texture directions.

Allen and Sayers [10] used a relationship between the longitudinal wave velocity and the two shear wave velocities, both normalized by the sum of the squares of three velocities which is a texture independent quantity, to solve the separation problem. With this method, a uniaxial stress can be derived if the principal directions are aligned with the principal axes of the orthotropic material.

Another oblique incident technique was studied at the University of Oklahoma. In support of an initial proposal by Egle and Koshti [11], Sinaie [12] developed a first order approximate analytical solution for the separation of the texture-induced effect from the stress induced effect for slightly orthotropic aggregates of cubic crystallites. With the common assumptions of additivity of texture and stress-induced effects on the ultrasonic wave velocities, two different solution forms were proposed. The first solution form employs a combination of the linearized eigenvalues for texture parameters and stresses, and calls for six quasi-shear wave velocity measurements at six different incident angles in the symmetry planes to solve for the three texture parameters and the three principal strains. The second solution form represents a more approximate and commonly used formula and requires six ultrasonic time delay measurements in two symmetry planes at six different incident angles.

Because residual stresses are generally developed in a body as a result of inhomogeneous plastic deformation, the theoretical study of acoustoelasticity has recently been extended to “acoustoplasticity”. Johnson [13] developed an acoustoelastic theory for elastic-plastic materials. He found that the assumption that the wave velocities depend only on stress leads to erroneous results for plastic flow. From the theory of elastic-plastic deformations for finite strains, the velocities of the bulk waves propagating in a principal direction were derived in terms of the elastic strains, the plastic strain, and the work-hardening parameters. Based on Prandtl-Reuss plastic flow theory and the isotropic material assumption, Kobayashi [14] derived an explicit formula for plane harmonic

waves propagating in one of the principal directions. The results turned out to be very complicated, but the difference of two transverse wave speeds can be simply expressed as a function of the second and third order material constants, the difference of the principal plastic strains, and the difference of the principal stresses. Another approach was taken by Pao [15] who reviewed several theories of acoustoelasticity and acoustoplasticity. With proper modifications, he proposed a similar formula for anisotropic materials by including the effects of inherent anisotropy.

1.1.2 *Experimental Techniques*

The experimental study of acoustoelasticity depended on the development of appropriate ultrasonic measurement systems. Such a system usually consists of an excitation source, one or two transducers, a receiver, a display, and a processor. Since the acoustoelastic effect is very small, acoustoelastic techniques did not become routinely feasible until the 1960s when new and accurate ultrasonic velocity measurement techniques were developed. The most extensively used velocity measurement techniques are “sing-around”, pulse-echo overlap, and pulse-superposition techniques. These techniques can provide sufficient accuracy for the measurement of various materials under various loading conditions. In comparison with the other key components in the system, the transducers are the weakest link today. Until recently, almost all measurements were made with piezoelectric or ferroelectric transducers attached via a coupling agent onto a specimen. The irreproducibility of the coupling between transducer and specimen was the major source of difficulties encountered in making acoustoelastic

measurement; thus, this was probably the key factor in severely limiting the utilization of wave amplitude and waveform measurements.

Another drawback associated with the use of contact transducers is their inability to be applied in a scan. To overcome these difficulties, an advance was made using electromagnetic acoustic transducers (EMAT). The non-contacting EMATs yielded dramatic improvements over contact transducer in many experiments, and they can be used for scan purposes. The drawback of this kind of transducers lies in its intrinsically low signal-to-noise ratio. The development of the water-bath coupled transducer was another major advance because it overcame the coupling problem and was suitable for large scale scans. By mode conversion, shear waves could also be generated as desired.

Recently, scanning acoustic microscopy has been used in acoustoelastic measurements. Some advantages are:

1. possibility one to image and scan a large area
2. coupling is well understood
3. wide frequency range
4. various types of waves can be generated by mode conversion
5. high spatial resolution

As far as the experimental study of acoustoelasticity is concerned, the first major advance came from the discovery of acoustic birefringence by Bergman and Shahbender [16] and Benson and Raelson [17] in the late 1950s. Analogous to the changing of the speed of light in a stressed transparent body under the influence of initial stress, the shear

wave speeds along two principal directions of polarization are slightly different from the wave speed in an unstressed medium. This phenomenon has been successfully employed, using shear wave transducers to overcome the difficulty of determining the principal directions in plane stress measurements [18]. In 1967, Crecraft [19] extensively compared photoelasticity and acoustoelasticity in a series of tests with different materials and drew an analogy between acoustoelastic birefringence and photoelastic birefringence. He also defined the problems inherent in making acoustoelasticity measurements in the presence of material texture, plastic deformations, and residual stresses.

Since then, greater efforts have been devoted to the application and study of acoustoelasticity in practical situations. Egle and Bray [20] employed both longitudinal and transverse waves to measure the acoustoelastic constants and third-order elastic constants for rail steel. The sensitivities of the longitudinal and shear waves in different wave propagation directions to applied stress were tested and illustrated. This is helpful when selecting the proper mode and propagation direction to characterize specific stress states. The accuracy of “sing-around” and pulse-echo overlap techniques was also studied and compared. The results showed that the most consistent results were obtained by the latter technique. The test results also proved to be consistent with the prediction of the second-order theory of Hughes and Kelly.

After the development of plane acoustoelastic theory for slight orthotropic materials, many experiments were successfully performed to study the applied stress field in engineering materials and extend the work to residual stress measurements. Clark [20]

measured acoustic shear wave birefringence and acoustic axis rotation at 66 selected points around the crack tip of a standard notched fracture aluminum specimen. With Okada's theory [5], the shear stress contours were derived and showed very good agreement with theoretical results.

Fukuoka and his associates are very active in conducting residual stress measurements. As an example for considering the anisotropy of a material [22], they studied the residual stresses in a wide-flanged hot rolled beam. Assuming the texture anisotropy to be constant along the rolling direction, they measured the texture anisotropy at the stress-free end sections and obtained an average value for each rolling line. Subtracting the texture anisotropy from the total anisotropy, they found the acoustoelastic birefringence due to residual stresses. For comparison, residual stresses were also measured by a destructive strain gage method. A comparison of the residual stresses measured by the two methods showed that the results were in good agreement for the flanges, but not for the web. This is because that the texture was fairly constant along the beam for the flange but fluctuated considerably in the web.

An approach for welded residual stress measurements was conducted by Wu and Jiang [23, 24]. In their study, they employed the general slightly orthotropic plane acoustoelastic theory and adopted the R parameter proposed by Toda [25]. This approach was experimentally shown to be insensitive to slightly inhomogeneous texture. Thus, this approach partially overcame the texture inhomogeneity problem in residual stress measurements. The acoustoelastic measurements of residual stresses in a seam welded

steel plate showed good agreement with the results derived by a destructive strain gage method.

As an example of scan technology, Kino [26] used a water-bath coupling technique to determine the residual stress profiles in an extruded aluminum bar. He employed longitudinal waves at normal incidence in his measurements. Clearly, this approach is limited as shear information can not be obtained and will result in error if the thickness of the specimen is not uniform. In another approach, Blessing, et al., [27] used a non-contacting electromagnetic transducer (EMAT) to scan an aluminum ring-plug assembly. A shrink-fit residual stress with known distribution was calculated using elasticity theory. A comparison of the acoustoelastic stress measurements with the known theoretical stress distribution showed good agreement.

1.2 The Objective of The Present Work

In this background review, most of the approaches to residual stress measurement were based on monitoring the changes in sound velocity produced by a stress state and the assumption of a uniform stress distribution. These techniques were limited in their utility due to the use of the contact shear transducers (effectively precluding scanning large areas), the inability to resolve the dependence of residual stresses on depth (important for surface treatments), the difficulty in making accurate time delay measurements due to coupling problems, and the very small acoustoelastic effects observed for most practical materials.

Drescher-Krasicka [28, 29] demonstrated how scanning acoustic microscopy may be used to obtain qualitative images of the residual stress for a variety of materials and stress states. This was achieved in a novel way through the use of a spherically focused transducer to launch the waves necessary for complete characterization of the stress state in the material. Here, the shear waves were generated by a mode converted obliquely incident longitudinal wave. It should be noted that two distinct refracted shear waves will be observed at the water-specimen interface due to the stress induced anisotropy in the piece. The axisymmetric nature of the source insures that both shear modes will be simultaneously excited. Drescher-Krasicka exploited this superposition to her advantage by monitoring the amplitudes (not the arrival times) of the superimposed signals. Due to the constructive-destructive interference between the shear wave signals, the amplitude of the combined signal turned out to be very sensitive to small changes in acoustic velocity produced by local residual stresses. In this case, the interference yields a signal reflecting the difference of the two principal stresses in the biaxial field. One of the major goals of this research is to conduct theoretical studies and numerical simulations in order to lay a theoretical foundation and enhance the understanding of this new scanning technique. In Chapter II, based on the theory of finite deformations and the equations of motion, Christoffel equations in the presence of stresses are derived. They are then solved with first-order perturbation theory to determine two quasi-shear wave velocities in Chapter III. Modeling the acoustic microscope lens launching a strong axisymmetric longitudinal lobe at oblique incidence and considering the interference of two shear waves polarized in

the directions of the in-plane principal stress axes, a quantitative comparison between the simulation and the experimental results is performed for a diametrically compressed aluminum disk.

Most of the acoustoelastic work mentioned in the previous review involved bulk waves. The use of surface waves in this context has been limited. Rayleigh wave acoustoelasticity was first studied by Hayes and Rivlin [30]. Subsequently, Iwashimizu and Kobori [31] analyzed Rayleigh wave propagation in a finitely deformed isotropic elastic material. Martin [32] investigated the relative effects of stress and preferred grain orientation. Adler [33] measured the residual stress of circumferential welds in pipe. Recently, Lee, et al., [34] utilized line-focused acoustic microscopy to determine local near-surface stresses in an isotropic material. However, since a uniform strain distribution was assumed, these techniques were not able to evaluate the variation of the stress through the thickness of the material. In 1981, Hirao, et al., [35] theoretically and experimentally studied the dispersion of Rayleigh waves for a plate in pure bending. They found that the dispersion of a Rayleigh wave is prominent for relatively low frequencies and diminishes as the frequencies increase.

Another goal in the present study is to employ Rayleigh waves with a line-focused acoustic microscope to characterize through-thickness in-plane stress distributions. Assuming that the principal strain directions are known and strains are polynomially distributed with depth while uniform in the other directions, the formulas for the Rayleigh

wave velocity change versus an initial static stress are derived based on the first order perturbation approach. A detailed study will be presented in Chapter IV.

CHAPTER II

THEORY OF ACOUSTOELASTICITY

To conduct further theoretical studies and numerical simulations, a basic understanding of current acoustoelastic theory and a relevant background are essential. Acoustoelasticity is the interaction of acoustic waves with elastic deformations in a solid. The stress or strain induced change in the propagation wave velocity is generally known as the acoustoelastic effect. The foundation of acoustoelasticity is a small disturbance wave propagating in a predeformed body. In the linear theory of elasticity, the wave speeds are constant and are not affected by stress or strain states. However, in acoustoelasticity, nonlinearity must be employed to relate stress and stress induced wave speed change. The nonlinearity here includes the effects from both the nonlinear constitutive relations and from large deformations. In Chapters III and IV, we will start with the Christoffel equations and the governing equations of an infinitesimal wave propagating in a prestressed body. In order to avoid any ambiguity in understanding these equations, the following sections of this chapter will serve as a theoretical basis to clarify the concepts.

2.1 Wave Motion in a Predeformed Medium

To determine applied or residual stresses in a predeformed body by ultrasonic techniques, one must distinguish three states of the body: the natural state, the initial state, and the final state. In the natural state, a body is free from any stress and strain. Under the action of various loadings, the body is deformed to the initial state, at which an ultrasonic measurement is performed. The superimposed ultrasonic wave deforms the body further to the final state. The kinematics and kinetics of the deformations in these three states are described in the theory by a small motion superimposed on a finitely deformed body. Three vectors ξ , X , and x are used to denote the position of a material point in a body at these three different states, all relative to a common Cartesian frame of reference. In the natural state, the particle is identified by the coordinates $\xi(\xi_1, \xi_2, \xi_3)$. In the initial and final states, the positions of the same particle are described by coordinates $X(X_1, X_2, X_3)$ and $x(x_1, x_2, x_3)$, respectively, as shown in Fig. 2.1.

In the following study, several assumptions were made:

- The predeformation is static and the body is in equilibrium at the initial state
- The superimposed dynamic motion is very small
- In the natural state, the body is anisotropic
- The material is hyperelastic
- The process of deformation is either isentropic or isothermal

In the following equations, all physical variables in the natural state are indicated by the superscript o , those in the initial state by i , and those in the final state by f . All

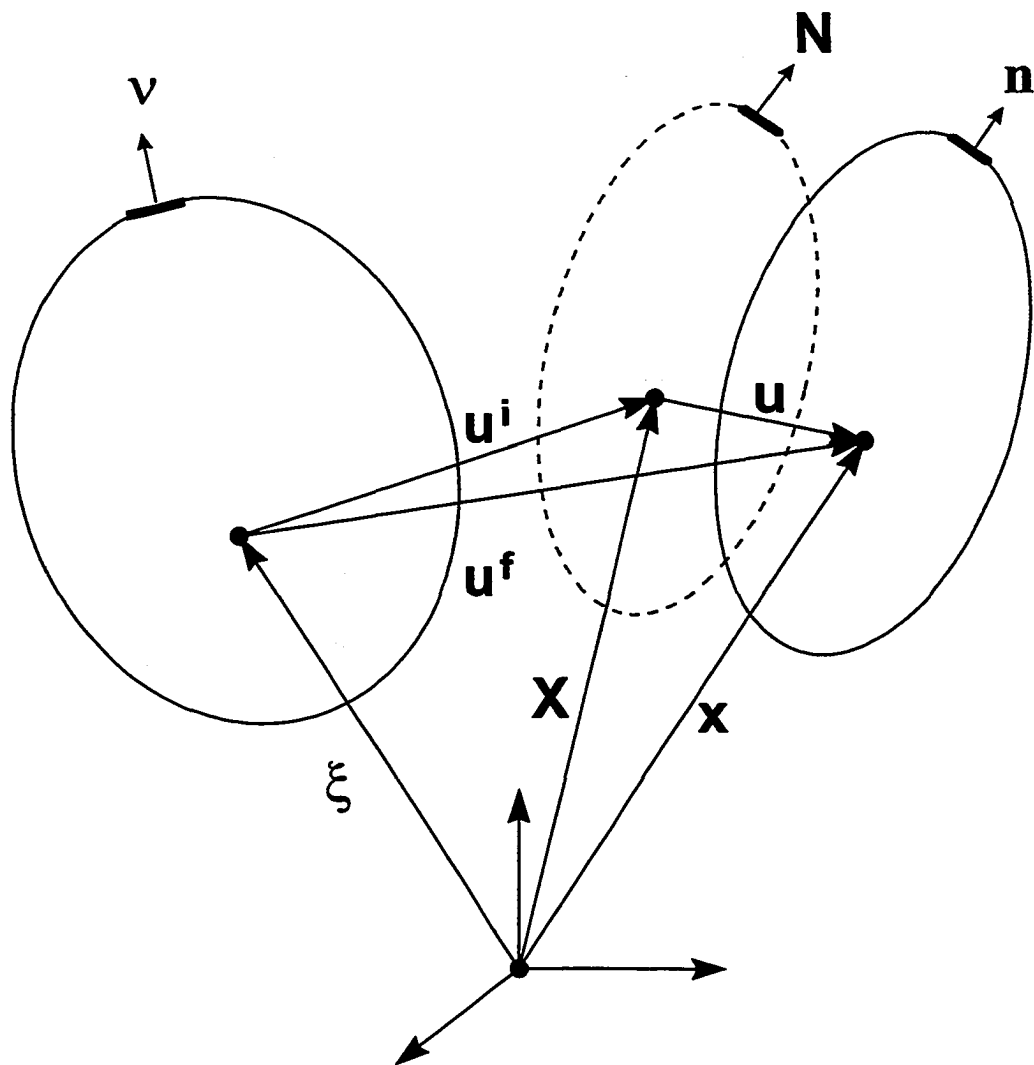


Fig. 2.1 Coordinates for a material point at the natural, initial, and final configurations of a predeformed body.

incremental variables are written without superscripts. The components of a vector or tensor in natural coordinates, ξ , are indicated by Greek subscripts, $\alpha, \beta, \gamma, \dots$, those in the initial coordinates, X , by upper case subscripts, I, J, K, \dots , and those in the final coordinates, x , by lower case subscripts i, j, k, \dots .

2.1.1 Deformation, Strain, and Stress

The deformation is characterized by transformations of coordinates. From the natural state to the initial state, the transformation is static and is defined by

$$\mathbf{X} = \mathbf{X}(\xi_1, \xi_2, \xi_3) \quad (2-1)$$

From the initial state to the final state, since the disturbance is a dynamic wave, the transformation becomes

$$\mathbf{x} = \mathbf{x}(X_1, X_2, X_3, t) \quad (2-2)$$

where \mathbf{X} and \mathbf{x} are two continuous vector functions and the inverse transformations are assumed to exist.

From the natural state, the displacements to the initial and final states are defined, respectively, as

$$\mathbf{u}^i(\xi) = \mathbf{X} - \xi \quad (2-3a)$$

$$\mathbf{u}^f(\xi) = \mathbf{x} - \xi \quad (2-3b)$$

From the initial to the final state, the incremental displacement is given by

$$\mathbf{u}(\xi, t) = \mathbf{x} - \mathbf{X} = \mathbf{u}^f - \mathbf{u}^i \quad (2-4)$$

In continuum mechanics theory, the deformation of a material particle is measured by deformation gradients. Using the polar decomposition theorem, the deformation gradients can be further decomposed into a rotation tensor multiplied by a stretch tensor. The Lagrangian strain of the body is defined by the square of the stretch tensor. In the initial and final states, it can be expressed as

$$E_{\alpha\beta}^i = \frac{1}{2} \left(\frac{\partial X_J}{\partial \xi_\alpha} \frac{\partial X_J}{\partial \xi_\beta} - \delta_{\alpha\beta} \right) \quad (2-5a)$$

$$E_{\alpha\beta}^f = \frac{1}{2} \left(\frac{\partial x_J}{\partial \xi_\alpha} \frac{\partial x_J}{\partial \xi_\beta} - \delta_{\alpha\beta} \right) \quad (2-5b)$$

In the preceding equations, $\delta_{\alpha\beta}$ is the Kronecker delta and the convention of summation over repeated indices is applied.

In terms of the displacement gradients, the Lagrangian strain can be expressed as

$$E_{\alpha\beta}^i = \frac{1}{2} \left(\frac{\partial u_\alpha^i}{\partial \xi_\beta} + \frac{\partial u_\beta^i}{\partial \xi_\alpha} + \frac{\partial u_\gamma^i}{\partial \xi_\beta} \frac{\partial u_\gamma^i}{\partial \xi_\alpha} \right) \quad (2-6a)$$

$$E_{\alpha\beta}^f = \frac{1}{2} \left(\frac{\partial u_\alpha^f}{\partial \xi_\beta} + \frac{\partial u_\beta^f}{\partial \xi_\alpha} + \frac{\partial u_\gamma^f}{\partial \xi_\beta} \frac{\partial u_\gamma^f}{\partial \xi_\alpha} \right) \quad (2-6b)$$

The difference of these two strain is defined as the incremental strain \mathbf{E} ,

$$\mathbf{E} = \mathbf{E}^f - \mathbf{E}^i \quad (2-7)$$

Substituting equation (2-6) into (2-7) and with the aid of equation (2-4), we obtain

$$E_{\alpha\beta} = \frac{1}{2} \left(\frac{\partial u_\alpha}{\partial \xi_\beta} + \frac{\partial u_\beta}{\partial \xi_\alpha} + \frac{\partial u_\lambda^i}{\partial \xi_\beta} \frac{\partial u_\lambda^i}{\partial \xi_\alpha} + \frac{\partial u_\lambda}{\partial \xi_\beta} \frac{\partial u_\lambda^i}{\partial \xi_\alpha} \right) \quad (2-8)$$

Here, the high order term $(\partial u_i / \partial \xi_\alpha)(\partial u_i / \partial \xi_\beta)$ is neglected, as the superimposed disturbance is small.

For the same reason, in the initial coordinates, the incremental Lagrangian strain can be simplified as

$$E_{IJ} = \frac{1}{2} \left(\frac{\partial u_I}{\partial X_J} + \frac{\partial u_J}{\partial X_I} + \frac{\partial u_K}{\partial X_I} \frac{\partial u_K}{\partial X_J} \right) \approx e_{IJ} \quad (2-9)$$

where

$$e_{IJ} = \frac{1}{2} \left(\frac{\partial u_I}{\partial X_J} + \frac{\partial u_J}{\partial X_I} \right) \quad (2-10)$$

is the infinitesimal strain.

The state of stress at a material point can be represented by a Cauchy stress tensor or a Kirchhoff stress tensor. Cauchy stress is the force per unit predeformed area with an outward normal \mathbf{N} as shown in Fig. 2.1. In the initial state, the Cauchy stress tensor is denoted by σ^i . This is the stress to be measured by ultrasonic methods. In finite deformation theory, however, it is more convenient to deal with the second Piola-Kirchhoff stress tensor, \mathbf{T}^i , because in terms of a strain energy function, it is the conjugate stress of the Lagrangian strain tensor. The second Piola-Kirchhoff stress lacks physical meaning. It represents the stress at the same material point but refers to the natural configuration. However, based on tensor theory, the Cauchy stress tensor can be expressed in terms of the second Piola-Kirchhoff stress tensor by

$$\sigma_{JK}^i = \left| \frac{\partial \mathbf{X}}{\partial \xi} \right|^{-1} \frac{\partial X_J}{\partial \xi_\alpha} \frac{\partial X_K}{\partial \xi_\beta} T_{\alpha\beta}^i \quad (2-11)$$

After the superposition of ultrasonic waves, the stress in the body is changed to σ^f in the final state, which can be converted to \mathbf{T}^f , expressed in either initial or natural coordinates,

$$\sigma_{jk}^f = \left| \frac{\partial \mathbf{x}}{\partial \xi} \right|^{-1} \frac{\partial x_j}{\partial \xi_\alpha} \frac{\partial x_k}{\partial \xi_\beta} T_{\alpha\beta}^f = \left| \frac{\partial \mathbf{x}}{\partial \mathbf{X}} \right|^{-1} \frac{\partial x_j}{\partial X_M} \frac{\partial x_k}{\partial X_N} T_{MN}^f \quad (2-12)$$

In analogy to Equation (2-7), the incremental stress tensor is defined by

$$\mathbf{T} = \mathbf{T}^f - \mathbf{T}^i \quad (2-13)$$

or

$$T_{JK} = T_{JK}^f - \sigma_{JK}^i \quad (2-14a)$$

$$T_{\alpha\beta} = T_{\alpha\beta}^f - T_{\alpha\beta}^i \quad (2-14b)$$

2.1.2 Equations of Wave Motion

One of the assumptions, the predeformation is static; therefore, there exists an equation of equilibrium for the initial state. There will also be an equation of motion for the final state. These equations can be expressed in terms of each type of stresses defined in the previous section.

In the literature, most of the equilibrium equations are expressed in terms of the Cauchy stress. The equations of equilibrium for σ_{JK}^i are simply given by

$$\frac{\partial \sigma_{JK}^i}{\partial X_K} = 0 \quad (2-15)$$

From equation (2-3), we have

$$\frac{\partial X_K}{\partial \xi_\beta^E} = \delta_{KY} \left(\delta_{Y\beta} + \frac{\partial u_Y^i}{\partial \xi_\beta^E} \right) \quad (2-16)$$

Substituting equation (2-16) into (2-11), the equilibrium equation in terms of $T_{\alpha\beta}^i$ can be derived:

$$\frac{\partial}{\partial \xi_\beta^E} [T_{\alpha\beta}^i + T_{\beta\gamma}^i \frac{\partial u_\alpha^i}{\partial \xi_\gamma^E}] = 0 \quad (2-17)$$

According to the law of conservation of mass, the densities in the three different states are related by the following equations:

$$\rho^0 = \rho^i \left| \frac{\partial \mathbf{X}}{\partial \xi} \right| = \rho^f \left| \frac{\partial \mathbf{X}}{\partial \xi} \right| \quad (2-18a)$$

$$\rho^i = \rho^f \left| \frac{\partial \mathbf{X}}{\partial \mathbf{X}} \right| \quad (2-18b)$$

Then, the equations of motion for the body in the final state yield one of the three forms:

$$\frac{\partial \sigma_{jk}^f}{\partial x_k} = \rho^f \frac{\partial^2 u_j}{\partial t^2} \quad (2-19a)$$

$$\frac{\partial}{\partial X_K} [T_{JK}^f + T_{KL}^f \frac{\partial u_J}{\partial X_L}] = \rho^i \frac{\partial^2 u_J^f}{\partial t^2} = \rho^i \frac{\partial^2 u_J}{\partial t^2} \quad (2-19b)$$

$$\frac{\partial}{\partial \xi_\beta} [T_{\alpha\beta}^f + T_{\beta\gamma}^f \frac{\partial u_\alpha^f}{\partial \xi_\gamma}] = \rho^0 \frac{\partial^2 u_\alpha^f}{\partial t^2} = \rho^0 \frac{\partial^2 u_\alpha}{\partial t^2} \quad (2-19c)$$

Subtracting Equation (2-15) from (2-19b) and Equation (2-17) from (2-19c), we obtain the equations of motion for the incremental stress in the two coordinates systems:

$$\frac{\partial}{\partial X_K} [T_{JK} + \sigma_{KL}^i \frac{\partial u_J}{\partial X_L}] = \rho^i \frac{\partial^2 u_J}{\partial t^2} \quad (2-20a)$$

$$\frac{\partial}{\partial \xi_\beta} [T_{\alpha\beta} + T_{\beta\gamma}^i \frac{\partial u_\alpha}{\partial \xi_\gamma} + T_{\beta\gamma} \frac{\partial u_\alpha^i}{\partial \xi_\gamma}] = \rho^0 \frac{\partial^2 u_\alpha}{\partial t^2} \quad (2-20b)$$

In this derivation, the products $T_{KL}(\partial \mu_J / \partial X_L)$ and $T_{\beta\gamma}(\partial \mu_\alpha / \partial \xi_\gamma)$ were neglected for small incremental motion.

2.1.3 Constitutive Equations

The third assumption made in this section states that the material is hyperelastic, which means that both initial deformation and final deformation are elastic. Unlike many engineering materials whose stress state is characterized by an elastic-plastic response, the stress-strain behavior of hyperelastic materials is described by a strain energy potential. The strain energy potential relates the stress and strain at a point to a strain energy density function which is used to characterize the material. In an isentropic or adiabatic process, a hyperelastic body is conservative and does not depend on the load path.

In the initial and final states, the internal energy function $\psi(E)$ can be expanded into a Taylor series about the natural state with zero strain,

$$\rho^0 \psi(E^i) = \frac{1}{2} c_{\alpha\beta\gamma\delta} E_{\alpha\beta}^i E_{\gamma\delta}^i + \frac{1}{6} c_{\alpha\beta\gamma\delta\epsilon\eta} E_{\alpha\beta}^i E_{\gamma\delta}^i E_{\epsilon\eta}^i + \dots \quad (2-21a)$$

$$\rho^0 \psi(E^f) = \frac{1}{2} c_{\alpha\beta\gamma\delta} E_{\alpha\beta}^f E_{\gamma\delta}^f + \frac{1}{6} c_{\alpha\beta\gamma\delta\epsilon\eta} E_{\alpha\beta}^f E_{\gamma\delta}^f E_{\epsilon\eta}^f + \dots \quad (2-21b)$$

The second Piola-Kirchhoff stresses in the corresponding two states are given by

$$T_{\alpha\beta}^i = \rho^0 \frac{\partial \psi(E^i)}{\partial E_{\alpha\beta}^i} \quad (2-22a)$$

$$T_{\alpha\beta}^f = \rho^0 \frac{\partial \psi(E^f)}{\partial E_{\alpha\beta}^f} \quad (2-22b)$$

The second and third order moduli are obtained by taking a further derivative with respect to Langrange strain as

$$c_{\alpha\beta\gamma\delta} = \rho^0 \left[\frac{\partial^2 \psi(E^i)}{\partial E_{\alpha\beta}^i \partial E_{\gamma\delta}^i} \right]^0 \dots\dots \quad (2-23a)$$

or

$$c_{\alpha\beta\gamma\delta} = \rho^0 \left[\frac{\partial^2 \psi(E^f)}{\partial E_{\alpha\beta}^f \partial E_{\gamma\delta}^f} \right]^0 \dots\dots \quad (2-23b)$$

$$c_{\alpha\beta\gamma\delta\epsilon\eta} = \rho^0 \left[\frac{\partial^3 \psi(E^i)}{\partial E_{\alpha\beta}^i \partial E_{\gamma\delta}^i \partial E_{\epsilon\eta}^i} \right]^0 \dots\dots \quad (2-24a)$$

or

$$c_{\alpha\beta\gamma\delta\epsilon\eta} = \rho^0 \left[\frac{\partial^3 \psi(E^f)}{\partial E_{\alpha\beta}^f \partial E_{\gamma\delta}^f \partial E_{\epsilon\eta}^f} \right]^0 \dots\dots \quad (2-24b)$$

Because the derivative orders are interchangeable, the symmetric property of the material constants can be derived. For example:

$$c_{\alpha\beta\gamma\delta} = c_{\gamma\delta\alpha\beta} = c_{\beta\alpha\gamma\delta} \dots\dots (2-25)$$

Substituting equations (2-23) and (2-24) into (2-22) and neglecting high order terms, we obtain the constitutive equations for $T_{\alpha\beta}^i$ or $T_{\alpha\beta}^f$ as follows:

$$T_{\alpha\beta}^i = c_{\alpha\beta\gamma\delta} E_{\gamma\delta}^i + c_{\alpha\beta\gamma\delta\epsilon\eta} E_{\gamma\delta}^i E_{\epsilon\eta}^i (2-26a)$$

$$T_{\alpha\beta}^f = c_{\alpha\beta\gamma\delta} E_{\gamma\delta}^f + c_{\alpha\beta\gamma\delta\epsilon\eta} E_{\gamma\delta}^f E_{\epsilon\eta}^f (2-26b)$$

With the aid of equation (2-8), a constitutive equation for the incremental stress, T , is derived by subtracting $T_{\alpha\beta}^i$ from $T_{\alpha\beta}^f$

$$\begin{aligned} T_{\alpha\beta} &= c_{\alpha\beta\gamma\delta} E_{\gamma\delta} + c_{\alpha\beta\gamma\delta\epsilon\eta} E_{\gamma\delta}^i e_{\epsilon\eta} \\ &\cong c_{\alpha\beta\gamma\delta} \left(\delta_{\rho\gamma} + \frac{\partial u_{\rho}^i}{\partial \xi_{\gamma}^f} \right) \frac{\partial u_{\rho}}{\partial \xi_{\delta}^f} + c_{\alpha\beta\gamma\delta\epsilon\eta} \frac{\partial u_{\gamma}^i}{\partial \xi_{\delta}^f} \frac{\partial u_{\epsilon}}{\partial \xi_{\eta}^f} \end{aligned} (2-27)$$

where $e_{\epsilon\eta}$ is the linear part of $E_{\epsilon\eta}$.

The preceding constitutive equation can be rewritten as

$$T_{\alpha\beta} = C_{\alpha\beta\gamma\delta} \frac{\partial u_{\gamma}}{\partial \xi_{\delta}^f} (2-28)$$

where C is the “effective” elastic modulus of the predeformed body,

$$C_{\alpha\beta\gamma\delta} = c_{\alpha\beta\gamma\delta} + c_{\alpha\beta\gamma\delta} \frac{\partial u_{\gamma}^i}{\partial \xi_{\rho}^f} + c_{\alpha\beta\gamma\delta\epsilon\eta} \frac{\partial u_{\epsilon}^i}{\partial \xi_{\eta}^f} (2-29)$$

2.1.4. Governing Equations of Acoustoelasticity

Substituting equation (2-27) into equation (2-20b), we obtain

$$\frac{\partial}{\partial \xi_\beta} [\Gamma_{\alpha\beta\gamma\delta} \frac{\partial u_\gamma}{\partial \xi_\delta} + T_{\gamma\beta}^i \frac{\partial u_\alpha}{\partial \xi_\gamma}] = \rho^0 \frac{\partial^2 u_\alpha}{\partial t^2} \quad (2-30)$$

where

$$\Gamma_{\alpha\beta\gamma\delta} = C_{\alpha\beta\gamma\delta} + c_{\rho\beta\gamma\delta} \frac{\partial u_\alpha^i}{\partial \xi_\rho} \quad (2-31)$$

Equation (2-30) is the governing equation for acoustic waves propagating in an elastically deformed medium in natural coordinates. The initial stress T^i and the initial displacement gradient $\partial u^i / \partial \xi$ are related by the constitutive equation (2-26), and one of them can be eliminated from the equation. The T_α^i should be converted to σ_{JK}^i as the latter is the initial stress to be measured by ultrasonic methods. The difference between T_α^i and σ_{JK}^i is neglected for most applications where the predeformation is assumed small.

Equation (2-30) can also be expressed in the initial coordinates system. According to the transformation of the incremental second Piola-Kirchhoff tensor,

$$T_{IJ} = \left| \frac{\partial \mathbf{X}}{\partial \xi} \right|^{-1} \frac{\partial X_I}{\partial \xi_\alpha} \frac{\partial X_J}{\partial \xi_\beta} T_{\alpha\beta} \quad (2-32)$$

the constitutive equation can be further expressed as

$$T_{IJ} = \delta_{I\alpha} \delta_{J\beta} [T_{\alpha\beta} (1 - \frac{\partial u_\gamma^i}{\partial \xi_\gamma}) + T_{\alpha\gamma} \frac{\partial u_\beta^i}{\partial \xi_\gamma} + T_{\beta\gamma} \frac{\partial u_\alpha^i}{\partial \xi_\gamma}] \quad (2-33)$$

Substituting equation (2-27) into (2-33) and considering the following equations

$$c_{IJKL} = \delta_{I\alpha} \delta_{J\beta} \delta_{K\gamma} \delta_{L\delta} c_{\alpha\beta\gamma\delta} \quad (2-34a)$$

$$c_{IJKLMN} = \delta_{I\alpha} \delta_{J\beta} \delta_{K\gamma} \delta_{L\delta} \delta_{M\epsilon} \delta_{N\eta} c_{\alpha\beta\gamma\delta\epsilon\eta} \quad (2-34b)$$

we have

$$T_{IJ} = C_{IJKL} \frac{\partial u_L}{\partial X_K} \quad (2-35)$$

where

$$\begin{aligned} C_{IJKL} = & c_{IJKL} (1 - e_{NN}^i) + c_{IJKLMN} e_{MN}^i + c_{JMKL} \frac{\partial u_I^i}{\partial X_M} \\ & + c_{IMKL} \frac{\partial u_J^i}{\partial X_M} + c_{IJML} \frac{\partial u_K^i}{\partial X_M} + c_{IJKM} \frac{\partial u_L^i}{\partial X_M} \end{aligned} \quad (2-36)$$

Substituting Equation (2-35) into Equation (2-20a), we obtain the governing equation for acoustoelastic waves in initial coordinates as

$$\frac{\partial}{\partial X_J} [(C_{IJKL} + \sigma_{JL}^i \delta_{IK}) \frac{\partial u_K}{\partial X_L}] = \rho^i \frac{\partial^2 u_I}{\partial t^2} \quad (2-37)$$

All five assumptions have been used in deriving the governing equation as shown above; however, it should be noticed that no assumption of uniform initial strains has ever been invoked. Thus, the governing equation can be applied to solve non-homogeneously predeformed problems.

2.2 Christoffel Equations for Plane Waves in a Stress Induced Anisotropic Medium

In elastic wave propagation theory, when a plane wave is launched into an anisotropic medium, the wave is characterized by Christoffel equations. Solving for the wave modes and speeds yields an eigenvalue problem. In general, there are three distinct eigenvalues for the equations, each corresponding to a particular wave mode. There will be two quasi-transverse wave modes and a quasi-longitudinal wave mode perpendicular to each other. For isotropic materials, these become two pure shear waves and a pure longitudinal wave.

In this section, the Christoffel equations for a plane wave propagating in a stress induced anisotropic medium will be studied. In the following derivation, two more assumptions are made:

- the strain is uniform in the body
- the medium is isotropic in its natural state

With the uniform strain assumption and the equilibrium equation in the initial state, the governing equation (2-37) becomes

$$(C_{IJKL} + \sigma_{JL}^i \delta_{IK}) \frac{\partial^2 u_K}{\partial X_L \partial X_J} = \rho^i \frac{\partial^2 u_I}{\partial t^2} \quad (2-38)$$

A harmonic plane wave in the initial coordinate system can be represented by

$$U_I = U_I \exp[ik(N_J X_J - Vt)] \quad (2-39)$$

where k is wave number, N_J is wave normal and V is phase velocity.

Substituting equation (2-39) into equation (2-38), we have

$$(C_{IJKL} N_J N_L + \sigma_{JL}^i \delta_{IK} N_J N_L) U_K = \rho^i V^2 U_I. \quad (2-40)$$

Based on the law of conservation of mass, for small deformations, ρ^i can be converted to ρ^0 by

$$\rho^i \cong \rho^0(1 - e_{NN}^i) \cong \rho^0(1 + e_{NN}^i)^{-1} \quad (2-41)$$

Substituting the above equation into (2-40) and neglecting the high order term, we have

$$[(C_{IJKL}N_JN_L + \sigma_{JL}^i\delta_{IK}N_JN_L + C_{IJKL}N_JN_L + C_{IJKL}N_JN_L e_{NN}^i)]U_K = \rho^0 V^2 U_I \quad (2-42)$$

Defining the Christoffel tensor in the presence of stress,

$$A_{IK} = C_{IJKL}N_JN_L + \sigma_{JL}^i\delta_{IK}N_JN_L + C_{IJKL}N_JN_L + C_{IJKL}N_JN_L e_{NN}^i \quad (2-43)$$

equation (2-42) can be rewritten as

$$(A_{IK} - \rho^0 V^2 \delta_{IK})U_K = 0 \quad (2-44)$$

and the characteristic equation becomes

$$|A_{IK} - \rho^0 V^2 \delta_{IK}| = 0 \quad (2-45)$$

Solving the eigenvalue problem, two quasi-shear wave speeds and a quasi-longitudinal wave speed can be derived. Now the only problem left is to derive the Christoffel tensor in terms of material constants and strains.

For isotropic materials,

$$\begin{aligned} C_{IJKL} = & \lambda \delta_{IJ} \delta_{KL} + \mu (\delta_{IK} \delta_{JL} + \delta_{IL} \delta_{JK}) \\ & + (-\lambda + \nu_1) \delta_{IJ} \delta_{KL} + (-\mu + \nu_2) (\delta_{IK} \delta_{JL} + \delta_{IL} \delta_{JK}) e_{MM}^i \\ & + 2(\lambda + \nu_2) (e_{IJ}^i \delta_{KL} + e_{KL}^i \delta_{IJ}) \end{aligned} \quad (2-46)$$

$$+ 2(\mu + \nu_3)(e_{IK}^i \delta_{JL} + e_{IL}^i \delta_{JK} + e_{JK}^i \delta_{IL} + e_{JL}^i \delta_{IK})$$

where λ and μ are the Lamé constants, and ν_1, ν_2 , and ν_3 are the third order elastic constants.

For the wave normal, we have

$$\begin{cases} N_I \cdot N_J = 0 & \text{if } I \neq J \\ N_I \cdot N_J = 1 & I = J \end{cases} \quad (2-47)$$

$$\text{Let } \ell_1 = N_1 \quad \ell_2 = N_2 \quad \ell_3 = N_3 \quad (2-48)$$

Then, the components of the Christoffel tensor become

$$\begin{aligned} A_{11} &= (C_{1111}\ell_1^2 + C_{1212}\ell_2^2 + C_{1313}\ell_3^2)(1 + e_{11} + e_{22} + e_{33}) \\ &\quad + \sigma_{11}\ell_1^2 + \sigma_{22}\ell_2^2 + \sigma_{33}\ell_3^2 \\ A_{22} &= (C_{2121}\ell_1^2 + C_{2222}\ell_2^2 + C_{2323}\ell_3^2)(1 + e_{11} + e_{22} + e_{33}) \\ &\quad + \sigma_{11}\ell_1^2 + \sigma_{22}\ell_2^2 + \sigma_{33}\ell_3^2 \\ A_{33} &= (C_{3131}\ell_1^2 + C_{3232}\ell_2^2 + C_{3333}\ell_3^2)(1 + e_{11} + e_{22} + e_{33}) \\ &\quad + \sigma_{11}\ell_1^2 + \sigma_{22}\ell_2^2 + \sigma_{33}\ell_3^2 \\ A_{12} = A_{21} &= (C_{1121}\ell_1^2 + C_{1222}\ell_2^2 + C_{1323}\ell_3^2)(1 + e_{NN}) + \sigma_{11}\ell_1^2 + \sigma_{22}\ell_2^2 + \sigma_{33}\ell_3^2 \\ A_{13} = A_{31} &= (C_{1131}\ell_1^2 + C_{1232}\ell_2^2 + C_{1333}\ell_3^2)(1 + e_{NN}) + \sigma_{11}\ell_1^2 + \sigma_{22}\ell_2^2 + \sigma_{33}\ell_3^2 \\ A_{23} = A_{32} &= (C_{2131}\ell_1^2 + C_{2232}\ell_2^2 + C_{2333}\ell_3^2)(1 + e_{NN}) + \sigma_{11}\ell_1^2 + \sigma_{22}\ell_2^2 + \sigma_{33}\ell_3^2 \end{aligned} \quad (2-49)$$

From equation (2-46), it is easy to obtain

$$C_{1111} = \lambda + 2\mu + [(-\lambda + \nu_1) + (-\mu + \nu_2)]e_{NN} + 4(\lambda + \nu_2)e_{11}$$

$$\begin{aligned}
& +8(\mu + \nu_3)e_{11} \\
C_{2222} &= \lambda + 3\mu + [(-\lambda + \nu_1) + (-\mu + \nu_2)]e_{NN} + 4(\lambda + \nu_2)e_{22} \\
& +8(\mu + \nu_3)e_{22} \\
C_{3333} &= \lambda + 2\mu + [(-\lambda + \nu_1) + (-\mu + \nu_2)]e_{NN} + 4(\lambda + \nu_2)e_{33} \quad (2-50) \\
& +8(\mu + \nu_3)e_{33} \\
C_{1212} &= \mu + (-\mu + \nu_2)e_{NN} + 2(\mu + \nu_3)(e_{11} + e_{22}) \\
C_{1313} &= \mu + (-\mu + \nu_2)e_{NN} + 2(\mu + \nu_3)(e_{11} + e_{33}) \\
C_{2121} &= C_{1212} \\
C_{2323} &= \mu + (-\mu + \nu_2)e_{NN} + 2(\mu + \nu_3)(e_{22} + e_{33}) \\
C_{3131} &= C_{1313} \\
C_{3232} &= C_{2323} \\
C_{1121} &= C_{1222} = C_{1323} = C_{1131} = 0 \\
C_{1232} &= C_{1333} = C_{2131} = C_{2232} = C_{2333} = 0
\end{aligned}$$

For the first order approach, the constitutive equations for an isotropic material are simply

$$\begin{aligned}
\sigma_{11} &= \lambda e_{NN} + 2\mu e_{11} \\
\sigma_{22} &= \lambda e_{NN} + 2\mu e_{22} \\
\sigma_{33} &= \lambda e_{NN} + 2\mu e_{33}
\end{aligned} \quad (2-51)$$

In acoustoelastic theory, the third order elastic constants are usually expressed in terms of Murnaghan constants (l, m, n):

$$v_1 = 2l - 2m + n$$

$$v_2 = m - \frac{1}{2}n \quad (2-52)$$

$$v_3 = \frac{1}{4}n$$

After algebraic manipulation, we derive,

$$\begin{aligned}
A_{11} &= \ell_1^2 [\lambda + 2\mu + (4\lambda + 10\mu + 4m)e_{11} + (\lambda + 2l)e_{NN}] \\
&\quad + \ell_2^2 [\mu + 2\mu e_{22} - (2\mu + \frac{1}{2}n)e_{33} + (\lambda + 2\mu + m)e_{NN}] \\
&\quad + \ell_3^2 [\mu - (2\mu + \frac{1}{2}n)e_{22} + 2\mu e_{33} + (\lambda + 2\mu + m)e_{NN}] \\
A_{12} &= A_{21} = \ell_1 \ell_2 [\lambda + \mu + 2(\lambda + \mu)(e_{11} + e_{22}) \\
&\quad + (\frac{1}{2}\mu - 2m)e_{33} + (2l + m)e_{NN}] \\
A_{13} &= A_{31} = \ell_1 \ell_3 [\lambda + \mu + 2(\lambda + \mu)(e_{11} + e_{33}) \\
&\quad + (\frac{1}{2}\mu - 2m)e_{22} + (2l + m)e_{NN}] \\
A_{22} &= \ell_1^2 [\mu + 2\mu e_{11} - (2\mu + \frac{1}{2}n)e_{33} + (\lambda + 2\mu + m)e_{NN}] \\
&\quad + \ell_2^2 [\lambda + 2\mu + (4\lambda + 10\mu + 4m)e_{22} + (\lambda + 2l)e_{NN}] \\
&\quad + \ell_3^2 [\mu - (2\mu + \frac{1}{2}n)e_{11} + 2\mu e_{33} + (\lambda + 2\mu + m)e_{NN}] \quad (2-53) \\
A_{23} &= A_{32} = \ell_2 \ell_3 [\lambda + \mu + (\frac{1}{2}n - 2m)e_{11}
\end{aligned}$$

$$\begin{aligned}
& + 2(\lambda + \mu)(e_{22} + e_{33}) + (2l + m)e_{NN}] \\
A_{33} = & \ell_1^2 [\mu + 2\mu e_{11} - (2\mu + \frac{1}{2}n)e_{22} + (\lambda + 2\mu + m)e_{NN}] \\
& + \ell_2^2 [\mu - (2\mu + \frac{1}{2}n)e_{11} + 2\mu e_{22} + (\lambda + 2\mu + m)e_{NN}] \\
& + \ell_3^2 [\lambda + 2\mu + (4\lambda + 10\mu + 4m)e_{33} + (\lambda + 2l)e_{NN}]
\end{aligned}$$

This is the Christoffel tensor in the presence of stress or strain. In Chapter III, the eigenvalue problem will be solved with a first order perturbation approach to obtain two quasi-shear wave speeds.

CHAPTER III

A NEW SCANNING ACOUSTIC MICROSCOPY APPROACH TO IN-PLANE STRESS ANALYSIS

Acoustic microscopy has been designed and utilized as a tool to study the microstructure of materials. Since acoustic waves interact directly with the properties of the material in which they propagate, acoustic microscopy provides a unique capability for investigating aspects of a material that are not revealed by either light or electron microscopes. By using acoustic waves at frequencies in the GHz range, it is possible to obtain images with submicron resolution.

Recently, scanning acoustic microscopy has been applied to the field of acoustoelasticity. Meek, et al., [36] used a phase measuring acoustic microscope to measure residual stresses in electronic materials. Narita, et al., [37] studied residual stresses in ceramics with line focused microscopy. Lee, et al., [34] applied line focus acoustic microscopy to surface stress measurements in aluminum alloys and polymethylmethacrylate. These studies, however, were based on the stress induced wave speed theory. The reason why other ultrasonic wave information such as amplitude and

wave form is rarely of interest in acoustoelasticity is the fact that these parameters are less affected by stress and easily influenced by many other factors, thus, are difficult to be determined experimentally with sufficient precision. As a new approach, Drescher-Krasicka [28, 29] conducted a series of experiments to characterize in-plane stresses by monitoring the peak amplitudes of scanning acoustic microscopy signals resulting from polarized quasi-shear waves. Instead of simply relating the wave amplitude and the stress, this method took advantage of the interference of the shear wave signals due to stress induced anisotropy. The experiment turned out to not only overcome the shortcomings of the amplitude approach mentioned above, but also to convert it into an advantage. The experimental results showed much higher sensitivity than the conventional wave speed technique, or more precisely, the time of flight measurement technique. In this chapter, a theoretical base is provided and the information from the previous experimental study [29] is quantified. A mathematical model is also presented to provide a qualitative and quantitative comparison between the numerical simulation and the experimental results for a diametrically compressed aluminum disk.

3.1 First Order Perturbation Approach to Determine Wave Velocities

In Chapter II, the Christoffel equations in the presence of strain or stress were developed. In explicit format, they are:

$$\begin{aligned}
(A_{11} - \rho^0 V^2)m_1 + A_{12}m_2 + A_{13}m_3 &= 0 \\
A_{21}m_1 + (A_{22} - \rho^0 V^2)m_2 + A_{23}m_3 &= 0 \\
A_{31}m_1 + A_{32}m_2 + (A_{33} - \rho^0 V^2)m_3 &= 0
\end{aligned} \tag{3-1}$$

which yields an eigenvalue problem for the phase velocities.

Sinaie [12] proposed an exact solution approach to solve these equations, however, numerical problems were encountered in its implementation. Thus, a new approximation method is employed here. The approach is based on first order perturbation theory for the wave propagation in anisotropic media as developed originally by Jech and Psencik [38] for geological media. Since the acoustoelastic effect is relatively small, the mathematical solutions for the stressed sample can be treated as a first order perturbation of the isotropic solution. Rewriting the Christoffel equations in tensor format, we have

$$(A_{ik} - \rho^0 V^2 \delta_{ik})\alpha_k^{(m)} = 0 \tag{3-2}$$

where $m = 1, 2, 3$, and $\alpha^{(m)}$ corresponds to each of the eigenvectors.

In the perturbed medium, we may write

$$(A_{ik}^0 + \Delta A_{ik} - \rho^0 (V_0^{(m)} + \Delta V^{(m)})^2 \delta_{ik})(\alpha_k^{0(m)} + \Delta \alpha_k^{(m)}) = 0 \tag{3-3}$$

which yields

$$\begin{aligned}
& (A_{ik}^0 - \rho^0 V_0^{(m)2} \delta_{ik})\alpha_k^{0(m)} + (A_{ik}^0 - \rho^0 V_0^{(m)2} \delta_{ik})\Delta \alpha_k^{(m)} \\
& + (\Delta A_{ik} - 2\rho^0 V_0^{(m)} \Delta V^{(m)} \delta_{ik})\alpha_k^{0(m)} \\
& + (\Delta A_{ik} - 2\rho^0 V_0^{(m)} \Delta V^{(m)} \delta_{ik})\Delta \alpha_k^{(m)} = 0
\end{aligned} \tag{3-4}$$

However, the first term in this expansion must be identically zero due to equation (3-2).

Also, the final term can be neglected as it is of higher order than the remaining two expressions. Thus,

$$(A_{ik}^0 - \rho^0 V_0^{(m)2} \delta_{ik}) \Delta \alpha_k^{(m)} + (\Delta A_{ik} - 2\rho^0 V_0^{(m)} \Delta V^{(m)} \delta_{ik}) \alpha_k^{0(m)} = 0 \quad (3-5)$$

Multiplying this expression by $\alpha_i^{0(n)}$, the first term vanishes due to the symmetry of the Christoffel tensor and equation (3-5) reduces to

$$\Delta A_{ik} \alpha_k^{0(m)} \alpha_i^{0(n)} - 2\rho^0 V_0^{(m)} \Delta V^{(m)} = 0 \quad (3-6)$$

since the eigenvectors are orthonormal. Then,

$$\Delta V^{(m)} = \frac{1}{2\rho^0 V_0^{(m)}} B_{mn} \quad (3-7)$$

where

$$B_{mn} = \Delta A_{ik} \alpha_k^{0(m)} \alpha_i^{0(n)} \quad (3-8)$$

The only difficulty in applying this formula arises from the degeneracy of the shear modes in the unstressed, isotropic medium as the polarization (eigen) vectors are arbitrary. It is only known that they are perpendicular to the wave normal and to each other.

For an incident longitudinal wave in water (let the z direction correspond to the surface normal), the wave normal for the incident wave in the x-z plane will be given by

$$\tilde{l}_{in} = \begin{pmatrix} \sin \theta_{in} \\ 0 \\ \cos \theta_{in} \end{pmatrix} \quad (3-9)$$

and, upon refraction, for the shear mode

$$\tilde{l}_r = \begin{pmatrix} \sin \theta_{rs} \\ 0 \\ \cos \theta_{rs} \end{pmatrix} \quad (3-10)$$

when, via Snell's law,

$$\frac{\sin \theta_{in}}{V_l} = \frac{\sin \theta_{rs}}{V_s} \quad (3-11)$$

Let $\tilde{e}^3 = \tilde{l}_r$, which is a good approximation for the case of near isotropy (i.e., small residual stresses). We can then form an orthonormal triad, for example:

$$\tilde{e}^1 = \begin{pmatrix} 0 \\ 1 \\ 0 \end{pmatrix} \quad (3-12)$$

and

$$\tilde{e}^2 = \tilde{e}^3 \times \tilde{e}^1 = \begin{pmatrix} -\cos \theta_{rs} \\ 0 \\ \sin \theta_{rs} \end{pmatrix} \quad (3-13)$$

Then, the associated shear eigenvectors can be represented by

$$\tilde{\alpha}^{(1)} = a_{11}\tilde{e}^1 + a_{12}\tilde{e}^2 = \begin{pmatrix} -a_{12}\cos \theta_{rs} \\ a_{11} \\ a_{12}\sin \theta_{rs} \end{pmatrix} \quad (3-14)$$

$$\tilde{\alpha}^{(2)} = a_{21}\tilde{e}^1 + a_{22}\tilde{e}^2 = \begin{pmatrix} -a_{22}\cos \theta_{rs} \\ a_{21} \\ a_{22}\sin \theta_{rs} \end{pmatrix} \quad (3-15)$$

but, since $\tilde{\alpha}^{(1)}$ and $\tilde{\alpha}^{(2)}$ must be orthogonal,

$$a_{11} = a_{22} \quad \text{and} \quad a_{12} = -a_{21} \quad (3-16)$$

Returning to equation (3-5) for $m = 1$ and multiplying through by e_i^1 , we have

$$(A_{ik}^0 - \rho^0 V_0^{(1)2} \delta_{ik}) \Delta \alpha_k e_i^1 + (\Delta A_{ik} - 2\rho^0 V_0^{(1)} \Delta V^{(1)} \delta_{ik}) (a_{11} e_k^1 + a_{12} e_k^2) e_i^1 = 0 \quad (3-17)$$

The first term must be zero as any vector in the $\tilde{e}^1 \times \tilde{e}^2$ plane is an acceptable shear wave eigenvector as the shear eigenvalues degenerate. Since $\tilde{e}^1 \perp \tilde{e}^2$, we may write the resulting equation as

$$\bar{B}_{11} a_{11} + \bar{B}_{12} a_{12} - 2V_0^{(1)} \Delta V^{(1)} \rho^0 a_{11} = 0 \quad (3-18)$$

where

$$\bar{B}_{mn} = \Delta A_{ik} e_i^m e_k^n \quad (3-19)$$

Similarly, by multiplying equation (3-5) by e_i^2 for $m = 1$ and repeating the process, we obtain

$$\bar{B}_{12} a_{11} + \bar{B}_{22} a_{12} - 2V_0^{(1)} \Delta V^{(1)} \rho^0 a_{12} = 0 \quad (3-20)$$

Equation (3-18) and (3-20) have a nontrivial solution for a_{11} and a_{12} if

$$\begin{vmatrix} \bar{B}_{11} - 2V_0^{(1)} \Delta V^{(1)} \rho^0 & \bar{B}_{12} \\ \bar{B}_{12} & \bar{B}_{22} - 2V_0^{(1)} \Delta V^{(1)} \rho^0 \end{vmatrix} = 0 \quad (3-21)$$

Solving for $\Delta V^{(1)}$ yields

$$\Delta V^{(1)} = \frac{1}{4V_0^{(1)} \rho^0} \{ \bar{B}_{11} + \bar{B}_{22} \pm \sqrt{(\bar{B}_{11} - \bar{B}_{22})^2 - 4\bar{B}_{12}^2} \} \quad (3-22)$$

A similar result holds for $\Delta V^{(2)}$. Hence, there are two possible shear waves in the stressed medium, a fast wave V_{s1} corresponding to the positive root and a slow wave V_{s2} corresponding to the negative root. Thus, assuming axial symmetry from the spherically focused source with the bulk of the incident energy concentrated in a hollow cone of equally distributed rays about a single input incident angle, the longitudinal wave source will excite two shear waves of equal amplitude in the stressed medium whose velocities are given by

$$V_{s1} = V_{s0} + \frac{1}{4V_{s0}\rho^0} \{ \bar{B}_{11} + \bar{B}_{22} + \sqrt{(\bar{B}_{11} - \bar{B}_{22})^2 - 4\bar{B}_{12}^2} \} \quad (3-23a)$$

$$V_{s2} = V_{s0} + \frac{1}{4V_{s0}\rho^0} \{ \bar{B}_{11} + \bar{B}_{22} - \sqrt{(\bar{B}_{11} - \bar{B}_{22})^2 - 4\bar{B}_{12}^2} \} \quad (3-23b)$$

Equations (3-23a) and (3-23b) will serve as the fundamental equations to study the interference between two shear waves differing in phase.

The eigenvectors associated with the shear waves can also be derived from equations (3-14) to (3-16), (3-18), and (3-20):

If $\bar{B}_{12} = 0$,

$$a_{11} = a_{22} = 1 \quad \text{and} \quad a_{12} = -a_{21} = 0 \quad (3-24)$$

thus

$$\tilde{\alpha}^{(1)} = \tilde{e}^1 \quad \text{and} \quad \tilde{\alpha}^{(2)} = \tilde{e}^2 \quad (3-25)$$

For $\bar{B}_{12} \neq 0$,

$$a_{11} = \frac{\bar{B}_{12}}{|\bar{B}_{12}|} \left[\frac{1}{2} \left(1 + \frac{\bar{B}_{11} - \bar{B}_{22}}{[(\bar{B}_{11} - \bar{B}_{22})^2 + 4\bar{B}_{12}^2]^{1/2}} \right) \right]^{1/2} \quad (3-26a)$$

$$a_{12} = \frac{\bar{B}_{12}}{|\bar{B}_{12}|} \left[\frac{1}{2} \left(1 - \frac{\bar{B}_{11} - \bar{B}_{22}}{[(\bar{B}_{11} - \bar{B}_{22})^2 + 4\bar{B}_{12}^2]^{1/2}} \right) \right]^{1/2} \quad (3-26b)$$

Substituting equations (3-26a) and (3-26b) into equations (3-14) and (3-15), we obtain the exact specification of the eigenvectors in the plane perpendicular to the wave normal \tilde{l}_r . It should be noted that even though the unperturbed medium degenerated, the eigenvectors derived by the perturbation method are unique and they are controlled by the Christoffel tensor. Generally, different ΔA_{ik} will result in different eigenvectors.

3.2 Experiment

Scanning acoustic microscopy provides a convenient means to obtain an image of the residual stress distribution within a material. This can be obtained from monitoring the interference of shear waves traveling back and forth across the specimen which is generated by using acoustic microscope in an out-of-focus mode. The schematic diagram of the acoustic microscope's operation is shown in Fig. 3.1. An efficient transducer is excited with a tone burst in order to interrogate the sample of interest. It is also used as the receiving transducer in order to detect the echo from the surface. The transducer receives the reflected signal which is rectified and filtered to give a signal proportional to the amplitude of the returned signal. The transducer is mechanically scanned in raster style in order to create a two-dimensional acoustic image. This image is then displayed on

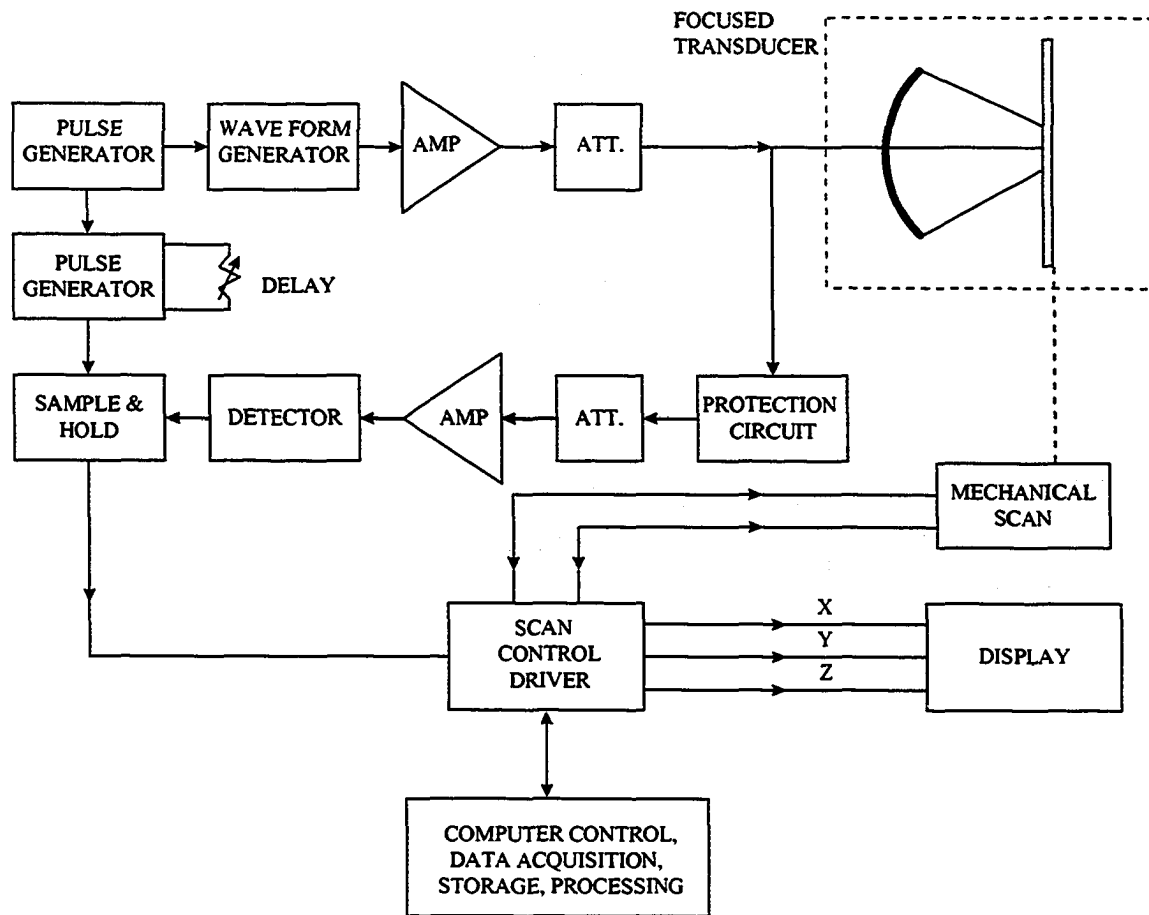


Fig. 3.1 Schematic diagram of acoustic microscopy.

a high-resolution color monitor using various pseudo-color and gray-level color schemes.

The scanning acoustic microscope used in the experiment is a broad frequency imaging system, with the frequency range adjustable from 1 to 150 MHz. The software of the system provides a single data gate, which has three adjustable parameters. The first is a gate start which specifies a starting time to monitor the ultrasonic waveform. The second is the gate length which specifies the amount of time after the gate starts during which the software will look for the peaks in the waveform. The software searches for the highest value the wave form attains. The third adjustable parameter of the gate is a threshold which specifies a percentage of the full screen height of the oscilloscope waveform. The peak below the threshold will be filtered and the peak values between the threshold and the 100% full screen height are displayed as a linearly distributed color value. When scanning the specimen, the software will monitor the change of the amplitude of the incoming signal and display certain corresponding colors in the pixels.

The specimen was an aluminum alloy (6061-T6) disk which was cut from an aluminum bar with both sides polished. The material properties are listed in Table 3.1. The disk thickness was 3 mm and the diameter was 40 mm. The specimen was diametrically compressed to several different load levels. The loading apparatus is shown in Fig. 3.2, along with the electronics used for load monitoring.

The geometry for the experiment is illustrated in Fig. 3.3. The sample was placed in a water tank and the acoustic scanning system was adjusted parallel to the surface of the specimen. The transducer launched longitudinal waves with 15 MHz of resonant

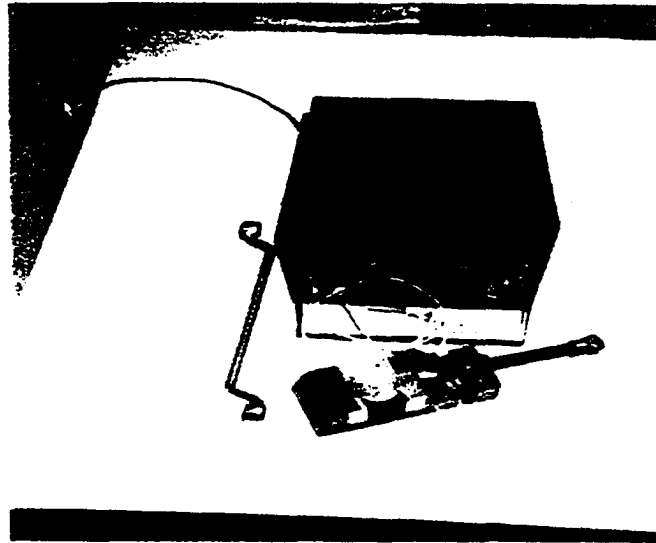


Fig. 3.2 Experimental loading facilities.

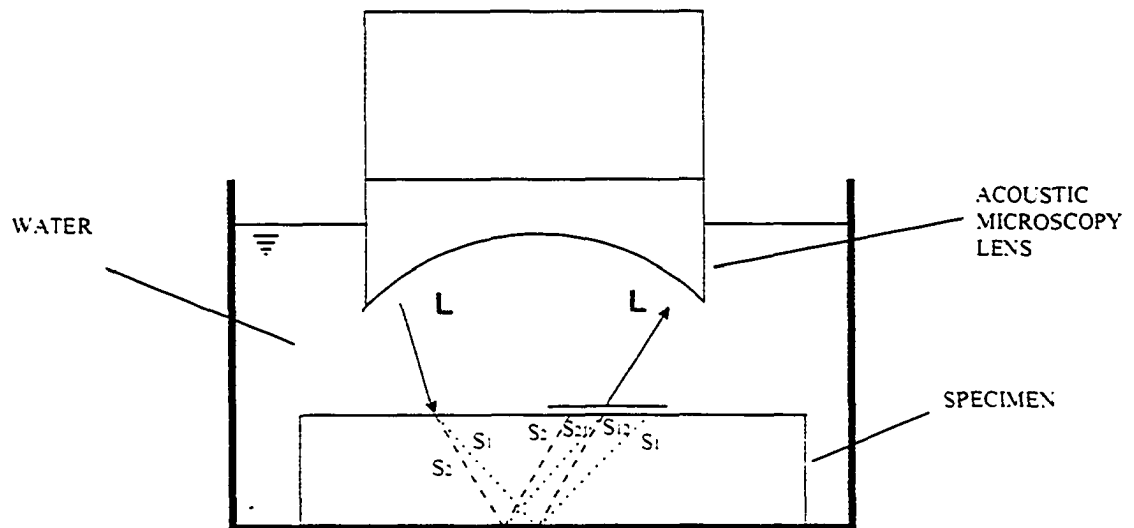


Fig. 3.3 Wave propagation diagram.

frequency. Monitoring the peak amplitudes of the superimposed shear waves, scanning acoustic microscopy images can be derived.

Table. 3.1 The material properties of aluminum alloy 6061-T6.

Density (kg/m ³)	Lamé Constants (× 10 ¹⁰ Pa)		Third-Order Elastic Constants (× 10 ¹⁰ Pa)			Shear Wave Speed (m / sec)
ρ	λ	μ	l	m	n	V_0
2710	4.32	2.65	-32.1	-41.1	-40.8	3127

3.3 Numerical Simulation

In order to quantify the information from the acoustic images of the distribution of stress in a diametrically compressed disk, the understanding of such a stress or strain distribution is essential. For the disk under a concentrated point load, the plane stress components at any location can be derived from the analytical solution of elasticity [39] and further used to obtain the principal strains. In practice, however, the load is distributed over a small area rather than being applied at a point, thus, the assumption of a point load will result in certain discrepancies which were discussed in a previous study [49]. Thence, a FEA simulation was performed to provide more accurate results reflecting the precise load distribution in the experiment.

3.3.1 Finite Element Analysis of a Diametrically Compressed Disk

Here, an aluminum disk under a diametrically applied compression load was modeled and analyzed with the general FEA software ANSYS 5.3. Since there were stress concentrations near the loading areas involving plastic deformations, both material and geometry nonlinearities were considered. A SHELL42 element was selected with keyoption(3)=3 to simulate a plane stress problem. The element is defined by four nodes having two degrees of freedom at each node: translations in the nodal x and y directions. SHELL 42 is commonly used for the 2-D modeling of solid structures with plasticity, creep, swelling, stress stiffening, large deflection, and large strain capabilities.

The element mesh is shown in Fig. 3.4. Based on the symmetric properties of the sample and load, only a quarter of the disk was modeled. Symmetric boundary conditions were applied at $X=0$ and $Y=0$. The stress-strain curve was assumed to be bilinear, with a Young's modulus of 69.6 GPa, a second tangent slope of 457 MPa, and a yield stress of 240 MPa. The main difficulty in the analysis was the simulation of the loading in the experiment. Because the loading frame was much stiffer than the specimen, the top and bottom surfaces of the disk where the loads were applied would be flattened. With this consideration, a displacement controlled loading strategy was selected with the displacement load applied in several load steps. In the first load step, the node with the maximum y coordinate was selected and a displacement down to the y-level of its adjacent node was applied. In the second load step, these two top most nodes were taken down to the y-level of the next highest adjacent node. This procedure was continued until

the load exceeded the maximum load of 1700 N in the test (as determined by checking the total nodal reaction forces). In this procedure, sufficient loading increments between the load steps have to be taken so that reaction forces close to the load levels in the experiment can be found. The loads in the experimental study were 716, 910, 1110, 1310, 1510, and 1700 N, respectively, and the closest load levels in the FEA simulation were found to be 714, 908, 1114, 1322, 1532, and 1728 N, respectively. Some important stress results of the analysis are given in Appendix B.

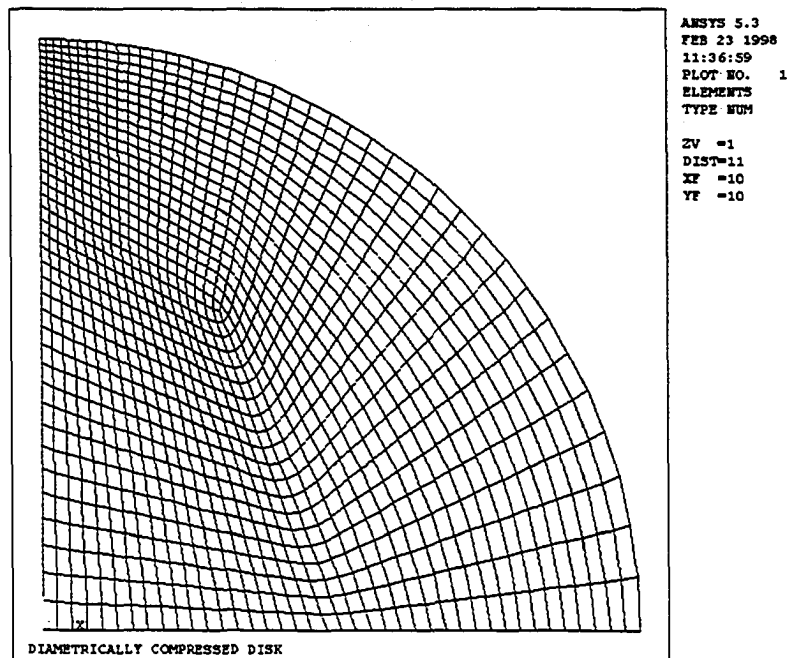


Fig. 3.4 FEA model for diametrically compressed disk.

3.3.2 Mathematical Model for Numerical Simulation

As shown in Fig. 3.3, the output of the scanning acoustic microscopy transducer can be modeled as having two main wave components: (1) a normal incidence pulse and (2) a strong axisymmetric longitudinal lobe at oblique incidence. The shear pulses indicated by S in the sample are of principal concern. Due to the presence of stresses in the medium, at the top of water-specimen interface, two shear waves are generated by the mode-converted, obliquely incident longitudinal waves. Their velocities will be slightly different, therefore, resulting in different refracted angles. At the bottom surface of the specimen, the two shear waves will produce two extra shear waves by mode conversion. The superimposed amplitudes of the four shear waves will be exploited for stress analysis. Assuming that the incident longitudinal wave and the two refracted quasi-shear waves generated at the top water-solid interface have velocities V_L , V_{s1} , and V_{s2} , respectively, and the corresponding directions of propagation are α_L , α_1 , and α_2 , according to Snell's law, we have

$$\frac{\sin \alpha_L}{V_L} = \frac{\sin \alpha_1}{V_{s1}} = \frac{\sin \alpha_2}{V_{s2}} \quad (3-27)$$

After the waves travel through the specimen, the phase shifts for $S_1 - S_4$ will be

$$\Phi_1 = \frac{4\pi fd}{V_{s1} \cos \alpha_1} \quad (3-28a)$$

$$\Phi_2 = \frac{4\pi fd}{V_{s2} \cos \alpha_2} \quad (3-28b)$$

$$\Phi_3 = \Phi_4 = \frac{4\pi fd}{V_{s1} \cos \alpha_1} + \frac{4\pi fd}{V_{s2} \cos \alpha_2} \quad (3-28c)$$

The interference of the shear waves at the top of the sample is then given by

$$y = A_1 \exp[i(2\pi ft + \Phi_1)] + A_2 \exp[i(2\pi ft + \Phi_2)] \\ + A_3 \exp[i(2\pi ft + \Phi_3)] + A_4 \exp[i(2\pi ft + \Phi_4)] \quad (3-29)$$

Assuming

$$A_1 = A_2 = A_3 = A_4 = A \quad (3-30)$$

the amplitude of the interfered wave yields

$$y = 4A \cos^2\left(\frac{\Phi_1 - \Phi_2}{4}\right) = 4A \cos^2\left(\frac{\pi fd}{V_{s1} \cos \alpha_1} - \frac{\pi fd}{V_{s2} \cos \alpha_2}\right) \quad (3-31)$$

Thus, the interfered shear wave amplitude calculation can be summarized in the following four steps:

- 1) Extract the principal strains at the nodes of interest from the FEA results
- 2) Determine the Christoffel tensor in the presence of stress or strain
- 3) Solve for two quasi-shear wave velocities with equations (3-19) and (3-23)
- 4) Calculate the amplitude of the interfered shear wave from equation (3-31)

The only remaining problem is how to compare the simulation results with the experimental results quantitatively. There are several obstacles: the incident longitudinal wave amplitude is unknown, the amplitude change due to mode conversion is unknown, as are the attenuation in the water and the final signal amplification in the acoustic microscopy. These factors make it almost impossible to realize a quantitative comparison

between simulation and experiment. To overcome these difficulties, a linear calibration scheme is employed in this study based on the following consideration: (1) the amplification used in the electronic circuits is usually linear and (2) the attenuations in water and sample are small because of short wave paths. Specifically, the procedure is as follows: determine the two unknowns in the linear equation by using the simulation and experimental results at any two locations of the disk, then use the same linear equation to amplify the amplitudes for the rest of the simulation results.

3.4 Experimental and Simulation Results

The experimental images of the scanning acoustic microscopy measurements at six different load levels are shown in Fig. 3.5 through Fig. 3.10. They were provided by Drescher-Krasicka of NIST. In order to realize a quantitative comparison with the numerical simulations, the peak amplitude curve along the diametrical loading line is also shown for each of the loading conditions. The quantitative comparisons between simulation and experimental results are shown in Fig. 3.11 to Fig. 3.16.

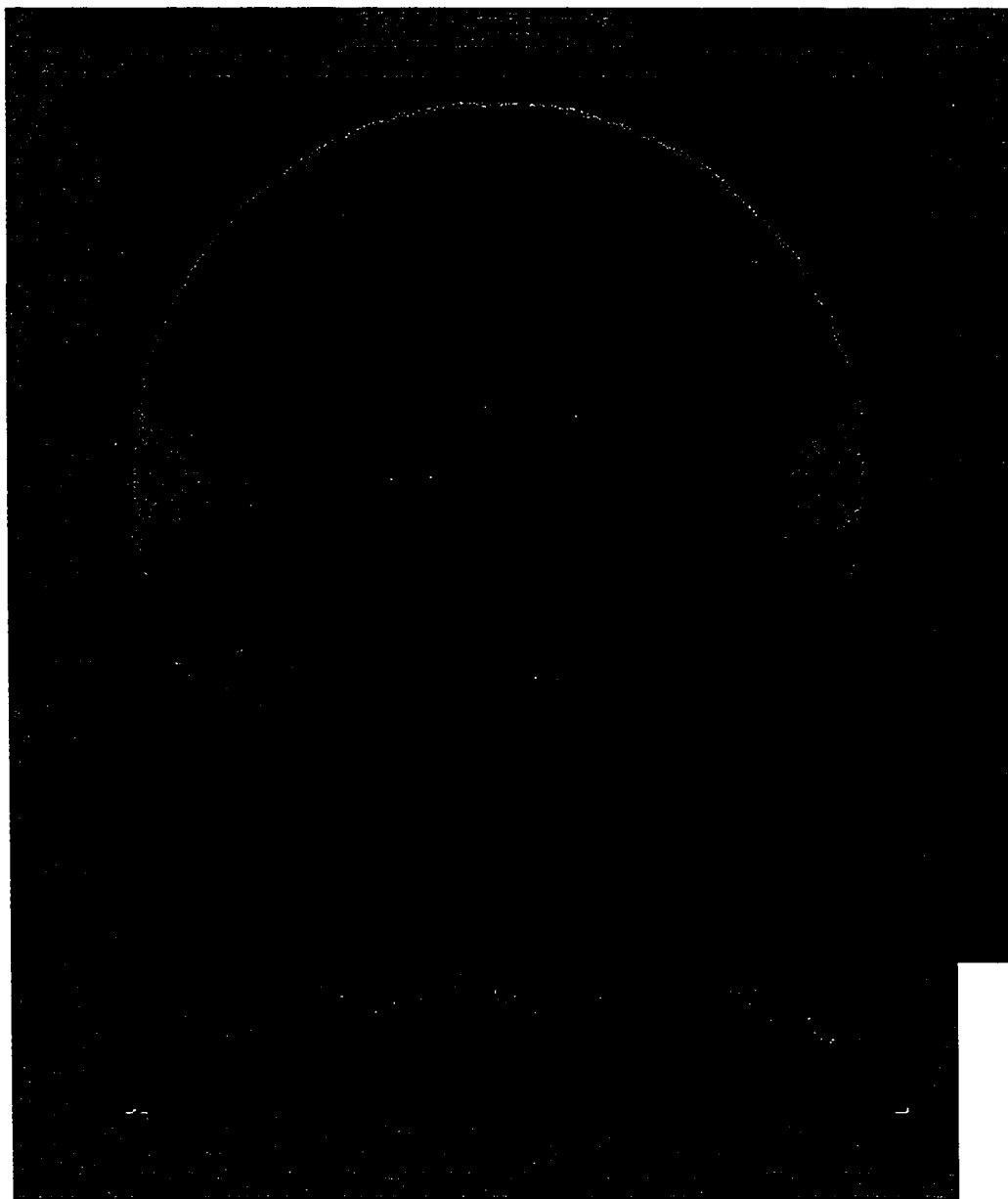


Fig. 3.5 Scanning acoustic microscopy image of a diametrically compressed disk ($P = 716 \text{ N}$) (Drescher-Krasicka, NIST).

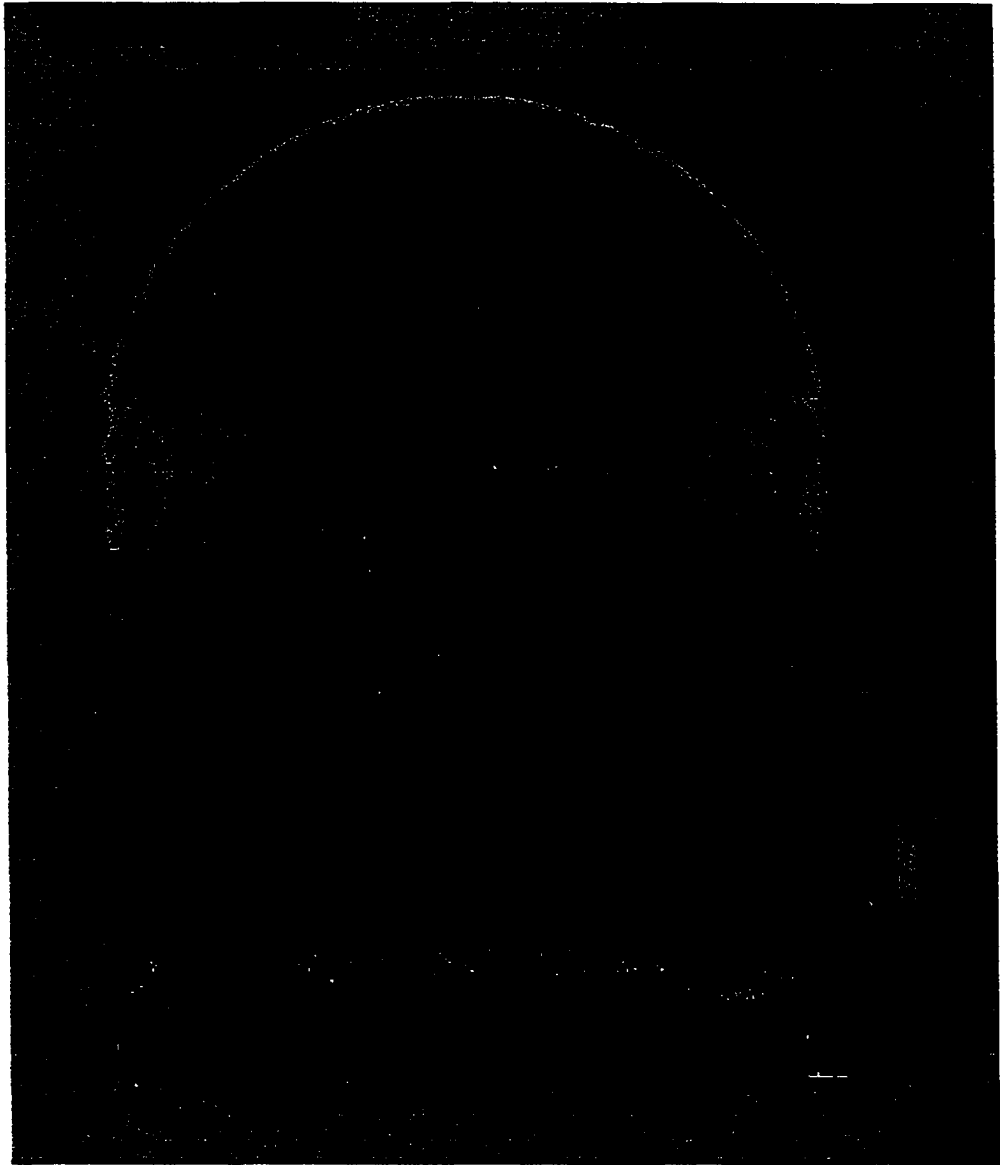


Fig. 3.6 Scanning acoustic microscopy image of a diametrically compressed disk ($P = 910 \text{ N}$) (Drescher-Krasicka, NIST).

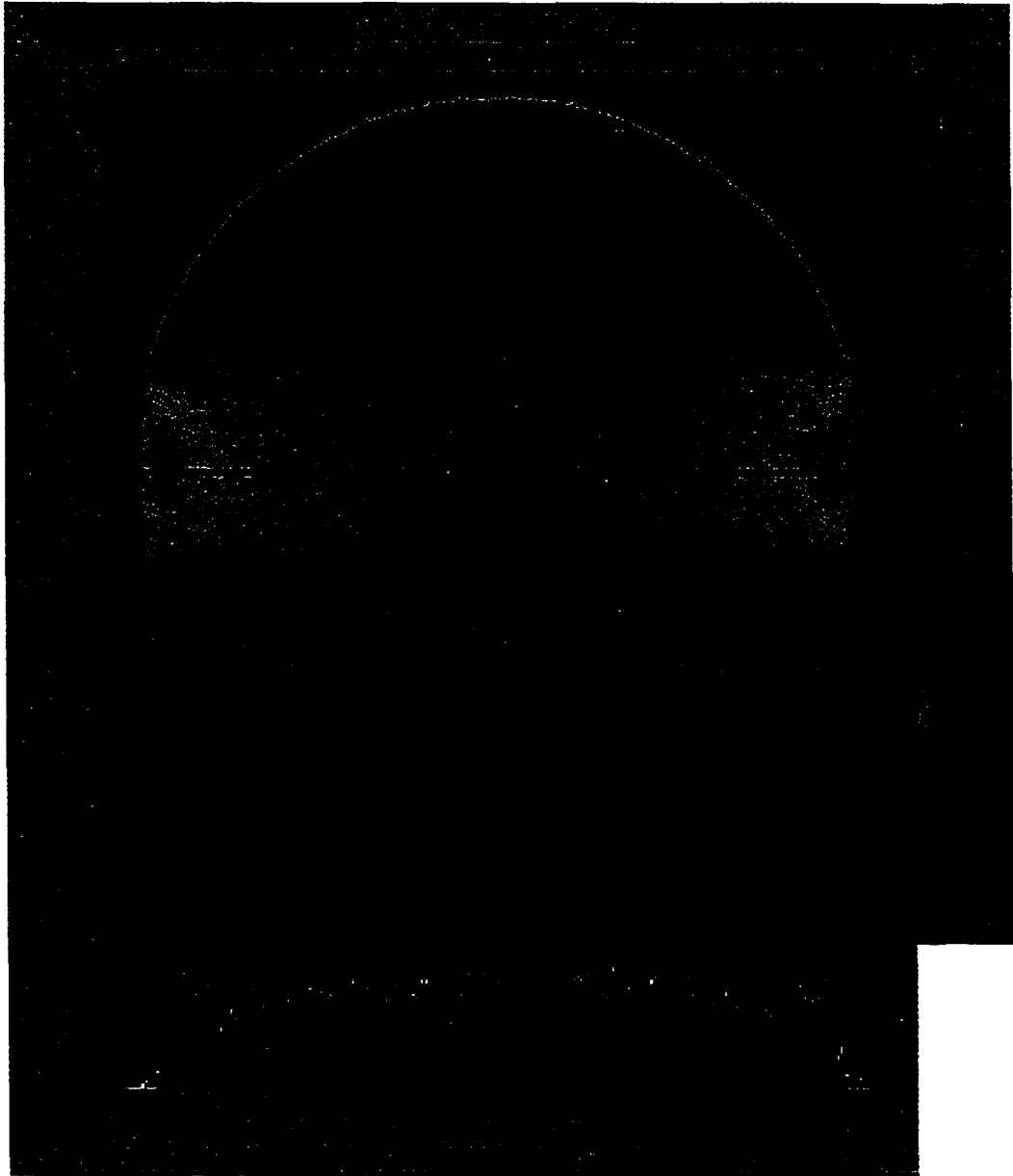


Fig. 3.7 Scanning acoustic microscopy image of a diametrically compressed disk ($P = 1110 \text{ N}$) (Drescher-Krasicka, NIST).

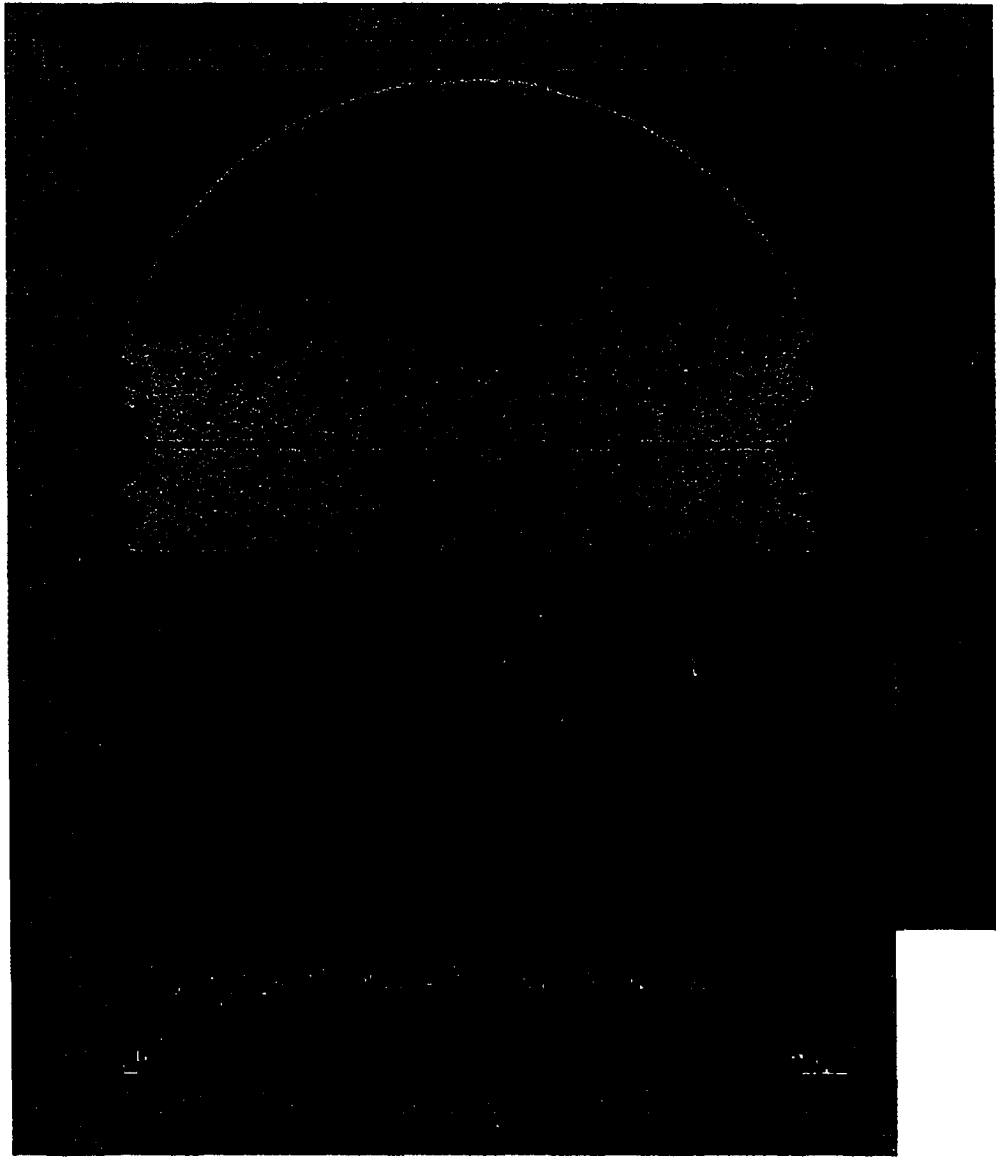


Fig. 3.8 Scanning acoustic microscopy image of a diametrically compressed disk ($P = 1310$ N) (Drescher-Krasicka, NIST).

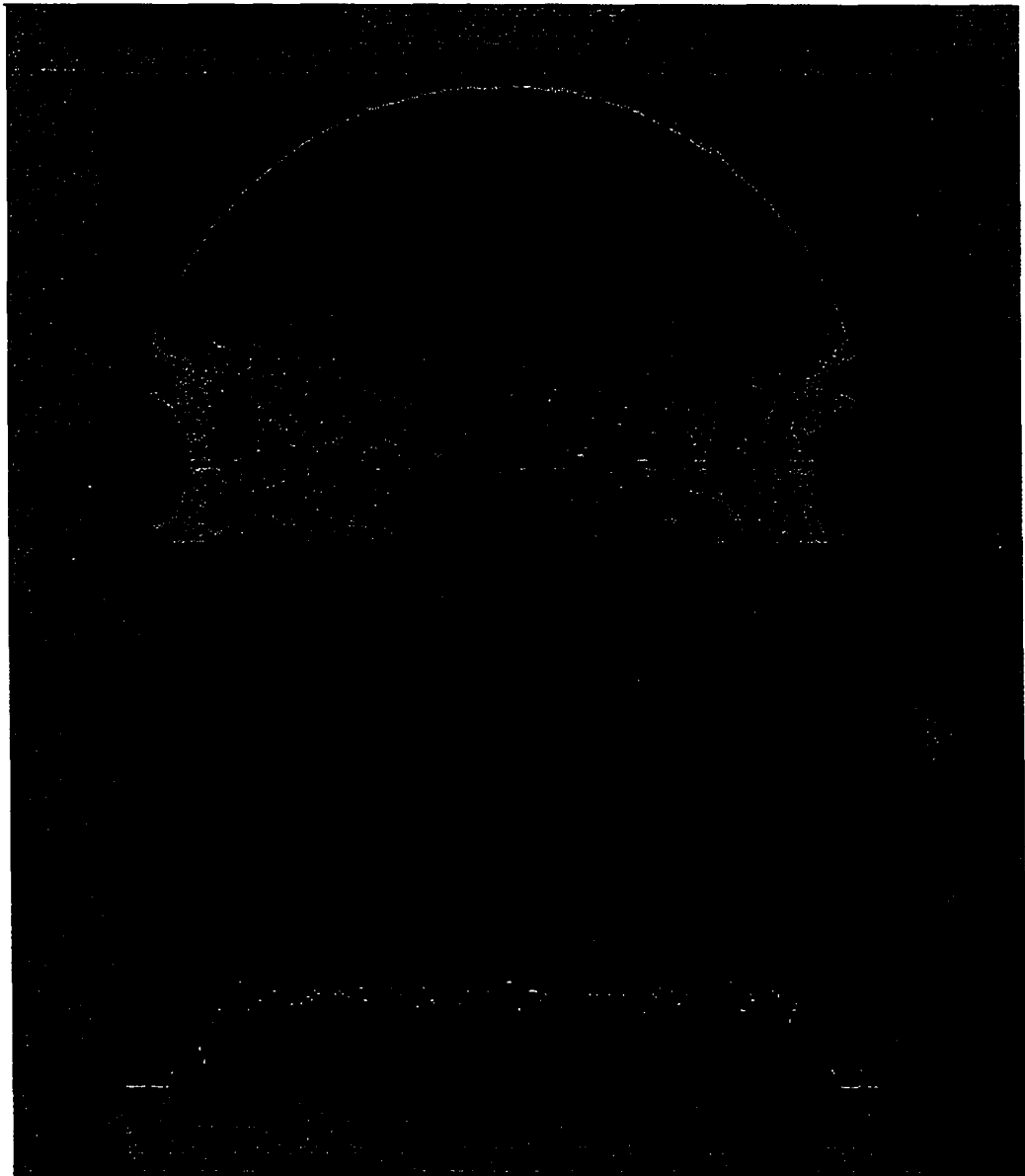


Fig. 3.9 Scanning acoustic microscopy image of a diametrically compressed disk ($P = 1510$ N) (Drescher-Krasicka, NIST).

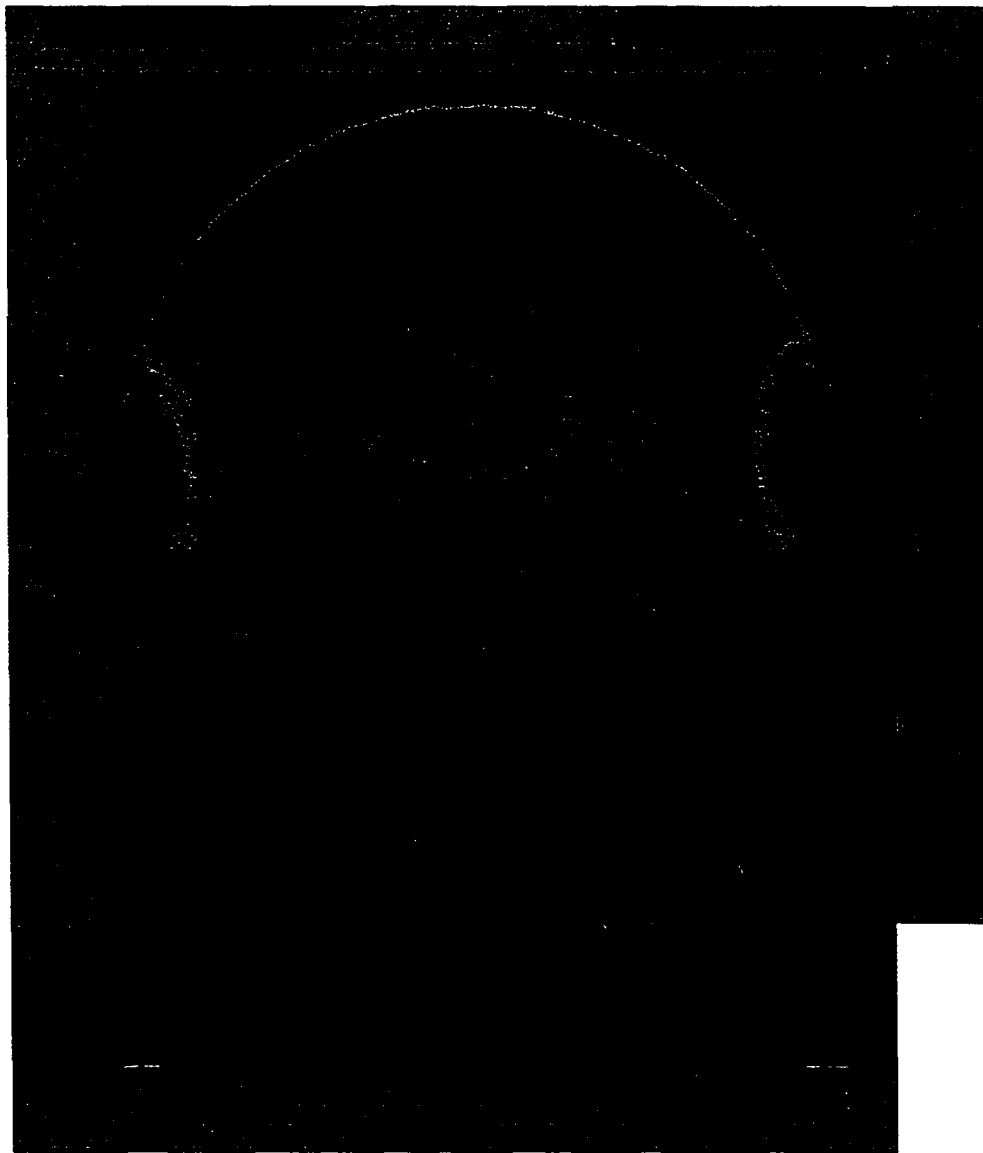


Fig. 3.10 Scanning acoustic microscopy image of a diametrically compressed disk ($P = 1700$ N) (Drescher-Krasicka, NIST).

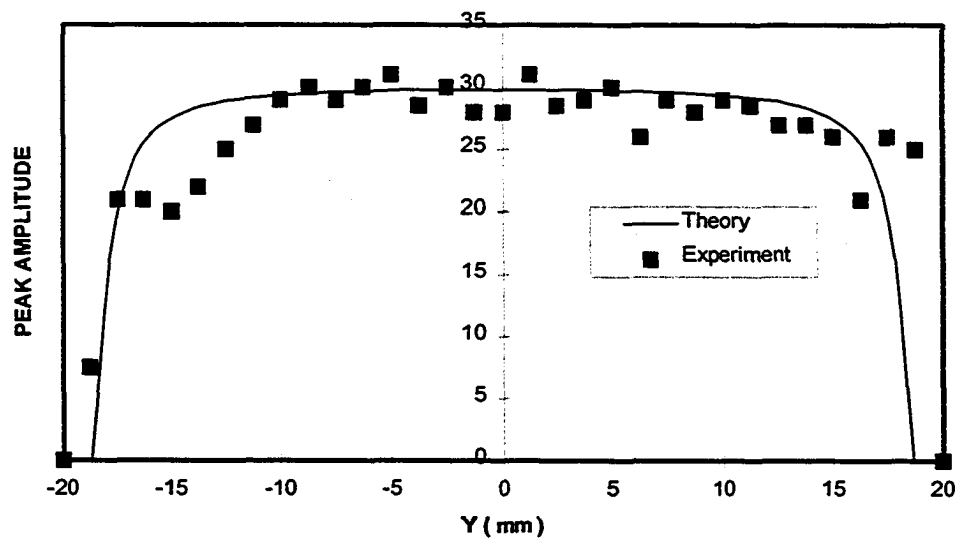


Fig. 3.11 Quantitative comparison between theoretical and experimental results ($P = 716$ N).

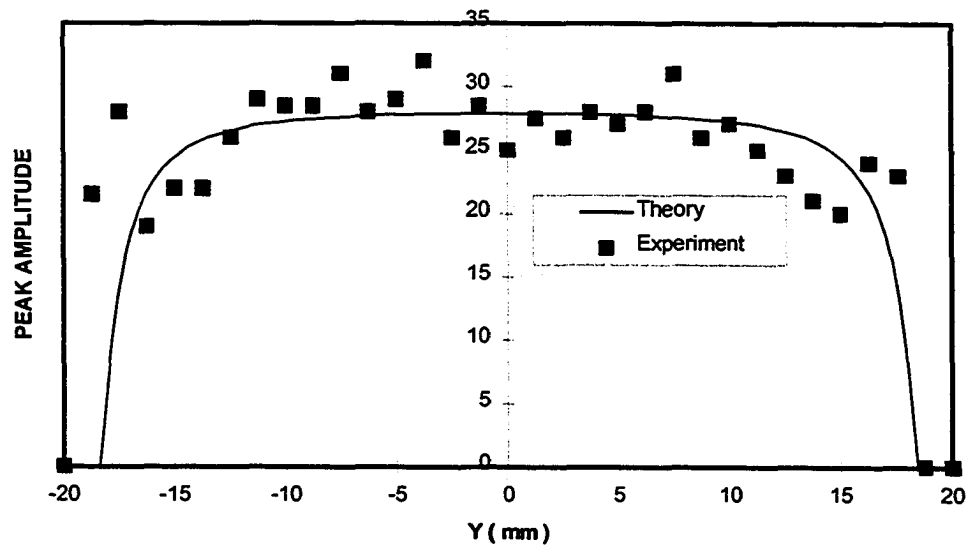


Fig. 3.12 Quantitative comparison between theoretical and experimental results ($P = 910$ N).

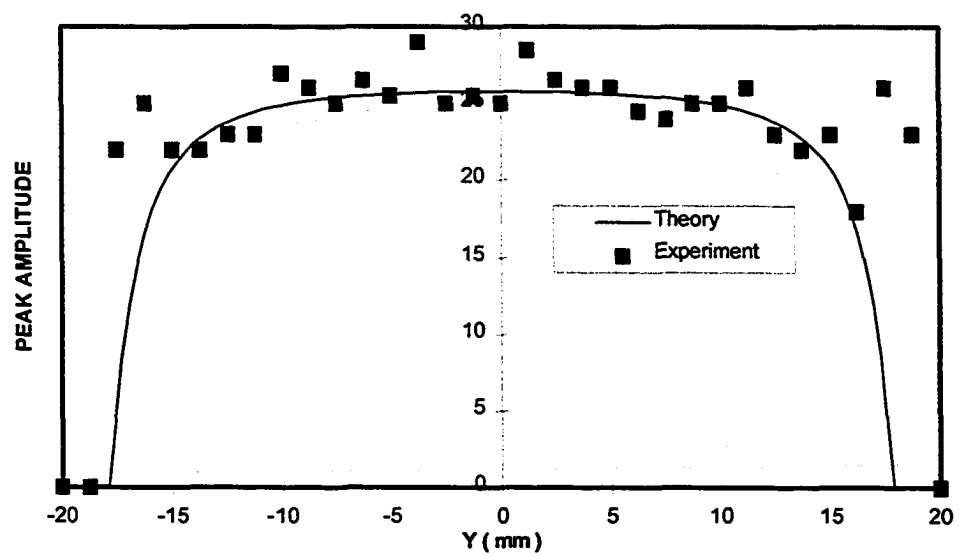


Fig. 3.13 Quantitative comparison between theoretical and experimental results ($P = 1110 \text{ N}$).

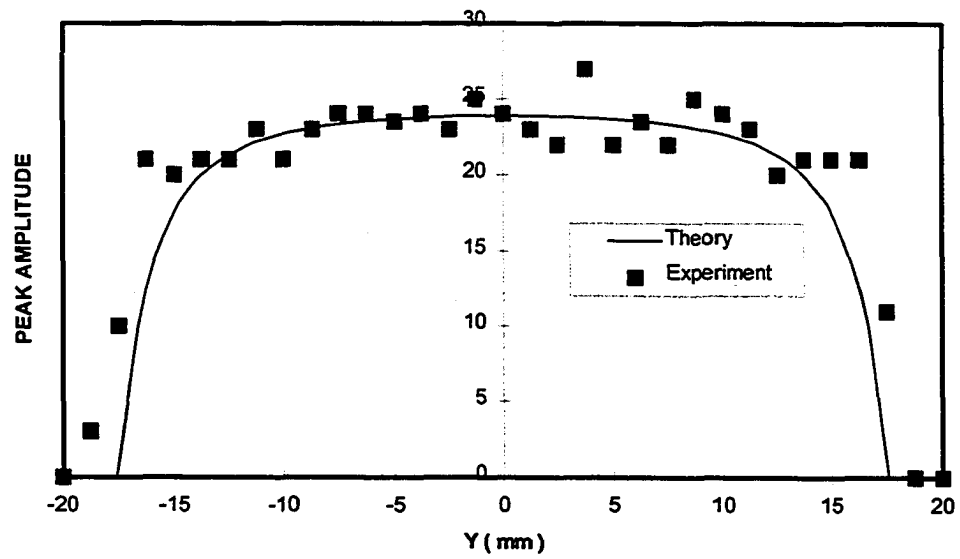


Fig. 3.14 Quantitative comparison between theoretical and experimental results ($P = 1310$ N).

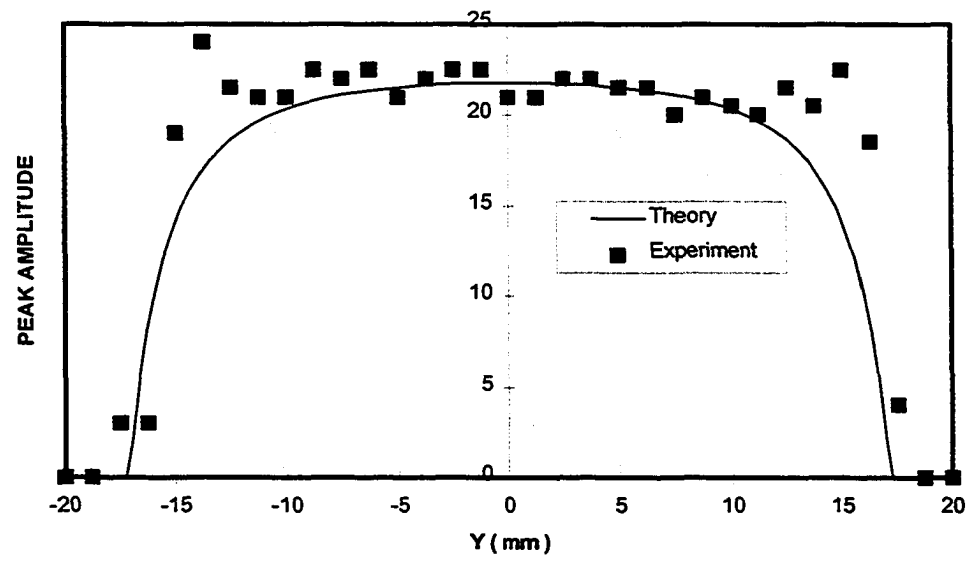


Fig. 3.15 Quantitative comparison between theoretical and experimental results ($P = 1510$ N).

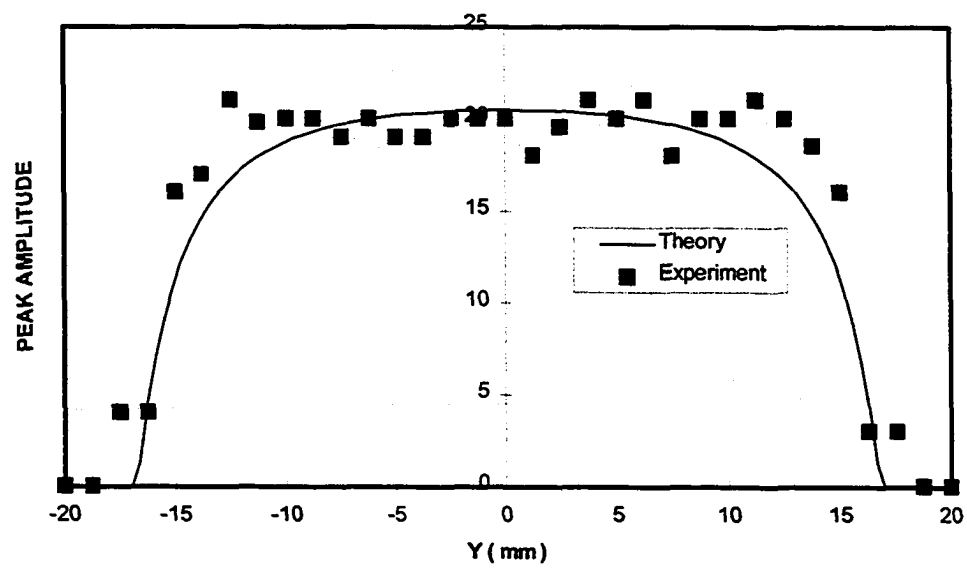


Fig. 3.16 Quantitative comparison between theoretical and experimental results ($P = 1700 \text{ N}$).

3.5 Discussion

The first question to be addressed in this discussion is the utility of the perturbation method to solve the problem. As reported in the paper of Jech and Psencik [38], for extremely anisotropic materials, the perturbation approach is less accurate in a degenerated unperturbed medium. In this study, the refracted quasi-shear wave angles required to form the Christoffel tensor were set equal by considering only small differences between the two quasi-shear wave velocities. In order to analyze the errors introduced by using the first-order perturbation approach, a comparison between the first-order perturbation solution and a full field solution was conducted. To simplify the calculation, the analytical elastic solution for a diametrically compressed disk was used:

$$\sigma_{xx} = -\frac{2P}{\pi t} \left(\frac{(R-y)x^2}{r_1^4} + \frac{(R+y)x^2}{r_2^4} - \frac{1}{d} \right) \quad (3-32a)$$

$$\sigma_{yy} = -\frac{2P}{\pi t} \left(\frac{(R-y)^3}{r_1^4} + \frac{(R+y)^3}{r_2^4} - \frac{1}{d} \right) \quad (3-32b)$$

$$\sigma_{xy} = \frac{2P}{\pi t} \left(\frac{(R-y)^2 x}{r_1^4} - \frac{(R+y)^2 y}{r_2^4} \right) \quad (3-32c)$$

where

$$r_1^2 = x^2 + (R-y)^2 \text{ and } r_2^2 = x^2 + (R+y)^2 \quad (3-33)$$

Here, R was the radius of the disk, t was its thickness, x and y were the coordinates along the X and Y axes with their origin located at the center of the disk, and P was the concentrated load. The principal stresses were obtained according to:

$$\begin{Bmatrix} \sigma_{11} \\ \sigma_{22} \end{Bmatrix} = \left(\frac{\sigma_{xx} + \sigma_{yy}}{2} \right)^2 \pm \sqrt{\left(\frac{\sigma_{xx} - \sigma_{yy}}{2} \right)^2 + \sigma_{xy}^2} \quad (3-34)$$

and the corresponding principal strains were calculated by Hooke's Law.

The principal difficulty encountered in solving the eigenvalue problem for a full field solution stems from the fact that the direction cosines of the refracted wave cannot be directly determined from Snell's law because of the directional dependence of the wave velocities. To overcome this difficulty, a scheme proposed by Kline [18] was adopted here. From equation (3-11), one may represent

$$\sin \theta_{re} = \frac{V_{re}}{V_{in}} \sin \theta_{in} = KV_{re} \quad (3-35)$$

For each of the refracted waves

$$\cos \theta_{re} = (1 - \sin^2 \theta_{re})^{1/2} = [1 - (KV_{re})^2]^{1/2} \quad (3-36)$$

Then, the eigenvalue problem becomes

$$\begin{vmatrix} A_{11} - \rho^0 V_{re}^2 & 0 & A_{13} \\ 0 & A_{22} - \rho^0 V_{re}^2 & 0 \\ A_{31} & 0 & A_{22} - \rho^0 V_{re}^2 \end{vmatrix} = 0 \quad (3-37)$$

where

$$\begin{aligned} A_{11} = & [1 - (KV_{re})^2][\lambda + 2\mu + (4\lambda + 10\mu + 4m)e_{11} + (\lambda + 2l)e_{NN}] \\ & + (KV_{re})^2[\mu - (2\mu + \frac{1}{2}n)e_{22} + 2\mu e_{33} + (\lambda + 2\mu + m)e_{NN}] \end{aligned} \quad (3-38a)$$

$$A_{22} = [1 - (KV_{re})^2][\mu + 2\mu e_{11} - (2\mu + \frac{1}{2}n)e_{33} + (\lambda + 2\mu + m)e_{NN}]$$

$$+ (KV_{re})^2 [\mu - (2\mu + \frac{1}{2}n)e_{11} + 2\mu e_{33} + (\lambda + 2\mu + m)e_{NN}] \quad (3-38b)$$

$$A_{33} = [1 - (KV_{re})^2] [\mu + 2\mu e_{11} - (2\mu + \frac{1}{2}n)e_{22} + (\lambda + 2\mu + m)e_{NN}] \\ + (KV_{re})^2 [\lambda + 2\mu + (4\lambda + 10\mu + 4m)e_{33} + (\lambda + 2l)e_{NN}] \quad (3-38c)$$

$$A_{13} = A_{31} = [1 - (KV_{re})^2] (KV_{re})^2 [\lambda + \mu + 2(\lambda + \mu)(e_{11} + e_{33}) \\ + (\frac{1}{2}\mu - 2m)e_{22} + (2l + m)e_{NN}] \quad (3-38d)$$

With a 1700 N compressive load and a 10 degree longitudinal incident angle with respect to the Z axis, two shear velocities were derived by solving the eigenvalue problem, utilizing the symbolic software Maple V. These velocities were subsequently substituted into equation (3-31) to determine the superimposed wave amplitude. The differences between the perturbation approach and the full field solution are presented in Fig. 3.17. Obviously, viewing the medium as being slightly perturbed from the isotropic state, results in errors in the vicinities of the two loading sites. However, if one considers the fact that these regions are actually in a plastic state while the elastic solutions give unrealistically high stresses, it is easy to conclude that the perturbation approach still provides satisfactory accuracy in comparison with the full field solution.

As a part of the verification of the FEA results, a stress comparison between the FEA solution and an elastic analytical solution along the transverse center line of the disk was conducted. Along this line, σ_y was a variant while σ_x stayed constant according to elastic theory. They were virtually the principal stresses. Six σ_y plots at different load

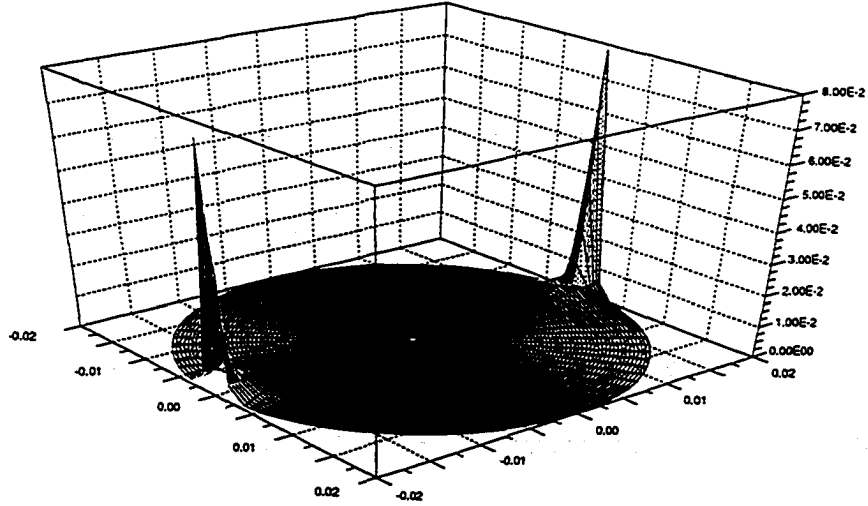


Figure 3.17 Errors introduced using perturbation theory compared with full field theory.

levels and one σ_x plot are presented in Fig. 3.18 to Fig. 3.24. The results show very good agreement between the FEA and analytical solutions in the center region of the disk. However, it should be noted that larger stress differences are expected at locations other than the transverse center line of the disk because of the loading condition.

One of the most important issues to be clarified in this study was the physical meaning of the peak amplitude of the interfered shear wave signals or, more specifically, how these signals relate to the residual stress to be measured.

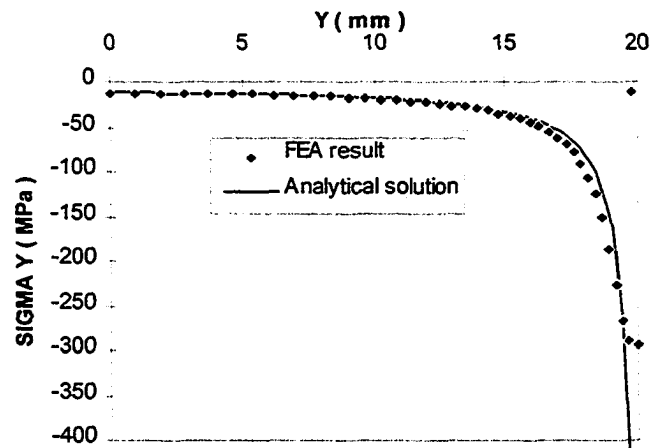


Fig. 3.18 Stress σ_y comparison between FEA and analytical solution for 716 N compressing load.

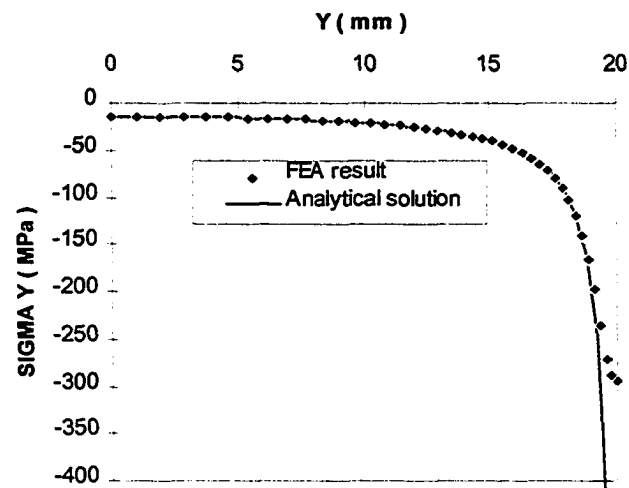


Fig. 3.19 Stress σ_y comparison between FEA and analytical solution for 910 N compressing load.

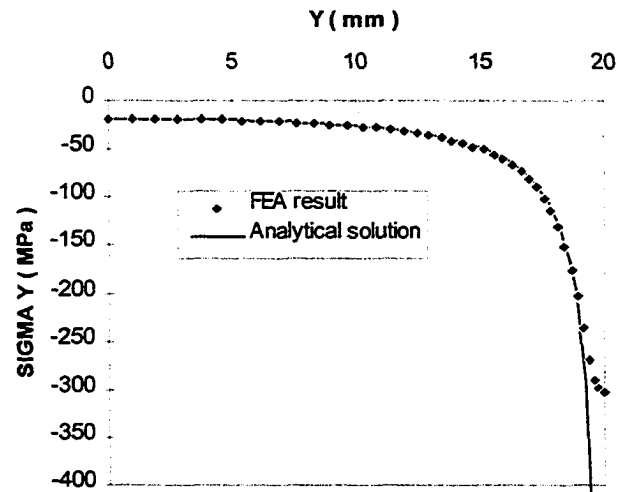


Fig. 3.20 Stress σ_y comparison between FEA and analytical solution for 1110 N compressing load.

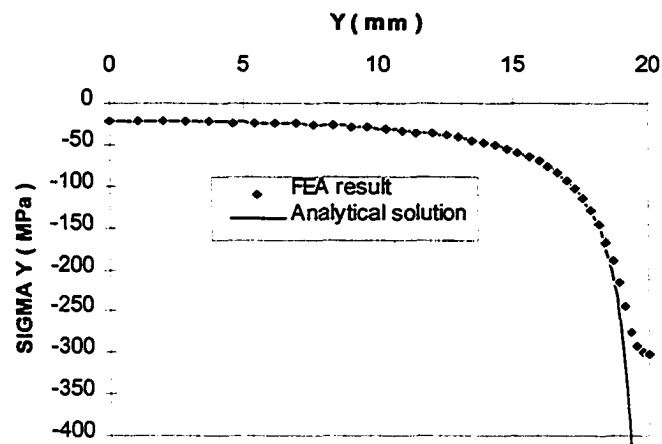


Fig. 3.21 Stress σ_y comparison between FEA and analytical solution for 1310 N compressing load.

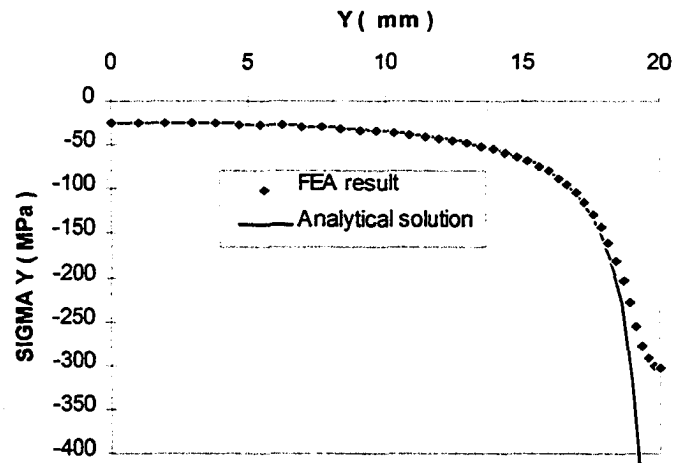


Fig. 3.22 Stress σ_y comparison between FEA and analytical solution for 1510 N compressing load.

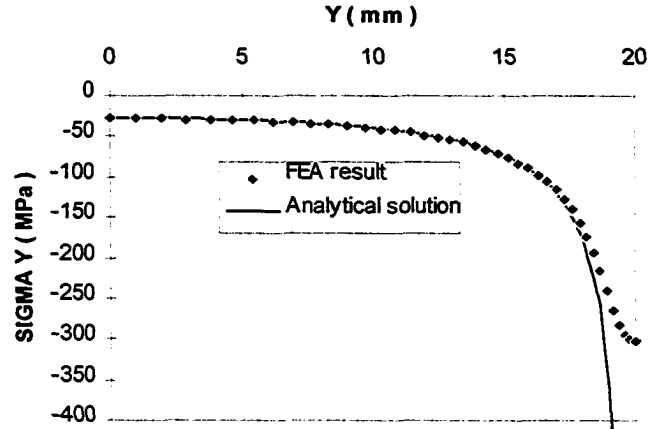


Fig. 3.23 Stress σ_y comparison between FEA and analytical solution for 1700 N compressing load.

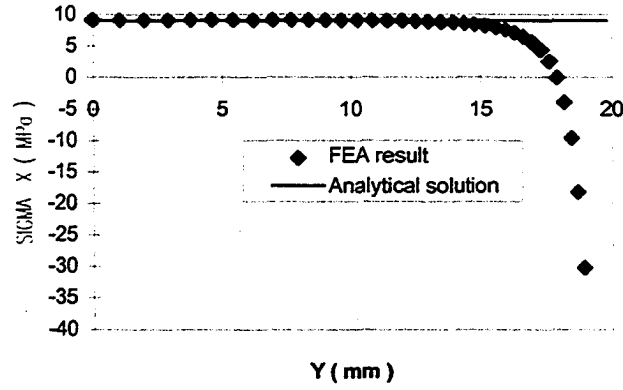


Fig. 3.24 Stress σ_x comparison between FEA and analytical solution for 1700 N compressing load.

Since the acoustoelastic effect is small, for small incident angles, one may neglect the refracted angle difference between the two shear waves. Then, we have $A_3 = A_4 = 0$ in equation (3-30), hence, the wave amplitude in equation (3-31) becomes

$$y = 2A \cos\left(\frac{\Phi_1 - \Phi_2}{2}\right) = 2A \cos\left(\frac{2\pi f d}{V_{s1} \cos \alpha_1} - \frac{2\pi f d}{V_{s2} \cos \alpha_1}\right) \quad (3-35)$$

This can be further simplified to yield

$$y = 2A \cos\left[\frac{2\pi f d}{\cos \alpha_1} \left(\frac{V_{s1} - V_{s2}}{V_{s1} V_{s2}}\right)\right] \cong 2A \cos\left[\frac{2\pi f d}{\cos \alpha_1} \left(\frac{V_{s1} - V_{s2}}{V_0^2}\right)\right] \quad (3-36)$$

where V_0 is the shear wave velocity in the stress-free isotropic material.

For an incident angle close to the normal direction of the disk plane, one may assume

$$\epsilon_1 = \epsilon_2 \cong 0 \text{ and } \epsilon_3 \cong 1 \quad (3-37)$$

in equation (2-53). Solving the eigenvalue problem, one obtains [1]

$$V_{s1} = \left(\frac{\mu}{\rho_0} \right)^{1/2} \left[1 + \frac{(\lambda + m)e_{kk} + 4\mu e_{33} + 2\mu e_{11} - \frac{1}{2}ne_{22}}{2\mu} \right] \quad (3-38a)$$

$$V_{s2} = \left(\frac{\mu}{\rho_0} \right)^{1/2} \left[1 + \frac{(\lambda + m)e_{kk} + 4\mu e_{33} + 2\mu e_{22} - \frac{1}{2}ne_{11}}{2\mu} \right] \quad (3-38b)$$

where V_{s1} and V_{s2} are the shear wave velocities polarized in the x_1 and x_2 principal directions.

From equation (2-51), one has

$$e_{11} - e_{22} = \frac{1}{2\mu} (\sigma_{11} - \sigma_{22}) \quad (3-39)$$

With the aid of equations (3-37) to (3-39), (3-36) yields

$$\begin{aligned} y &= 2A \cos \left[\frac{2\pi f d}{V_0^2} \frac{V_0}{2\mu} \left(2\mu + \frac{1}{2}n \right) (e_{11} - e_{22}) \right] \\ &= 2A \cos \left[\pi f d \left(\frac{4\mu + n}{4\mu^2 V_0} \right) (\sigma_{11} - \sigma_{22}) \right] \end{aligned} \quad (3-40)$$

Define

$$D = \pi f d \left(\frac{4\mu + n}{4\mu^2 V_0} \right) \quad (3-41)$$

Here, $D(\sigma_{11} - \sigma_{22})$ is on the order of 10^{-3} to 10^{-2} based on an approximate calculation, thus, it is small. Then equation (3-40) can be expanded into a Taylor series about zero

$$y = A[2 - D^2(\sigma_{11} - \sigma_{22})^2 + HOT] \quad (3-42)$$

and equation (3-42) may be further simplified as

$$y = C_1 - C_2(\sigma_{11} - \sigma_{22})^2 \quad (3-43)$$

where C_1 and C_2 are constants.

Hence, it can be concluded that, when the incident angle is small, the information about the amplitude of the interfered shear wave yields the square of the principal stress difference. It should be noted that this is a nonlinear relationship instead of a linear relationship as predicted by Drescher-Krasicka [28].

From Fig. 3.11 to Fig. 3.16, it is seen that, at the stressed area, the wave shows a decrease in amplitude; in other words, the higher the difference of the principal stresses, the lower the wave amplitude. This phenomenon can be well understood from equation (3-43). One point needs to be addressed here: Since the stress induced phase shift is small, one will not see a harmonic wave format change of the amplitude even with very large differences in the principal stresses. This will secure the single valued relationship between the amplitude and the difference in the principal stresses or the maximum in-plane shear stress. As far as a quantitative comparison is concerned, considering the experimental error, the correspondence of simulation and experimental results is quite satisfactory. It is noticed that the experimental results show certain levels of noise in the images. This may be due to the inhomogeneity of the sample material, unsatisfactory specimen surface conditions, and other possible sources of error.

CHAPTER IV

USING RAYLEIGH WAVE DISPERSION TO CHARACTERIZE IN-PLANE STRESSES

In the past forty years, bulk wave acoustoelasticity has been the subject of a great deal of research. One of the shortcomings, however, associated with the use of bulk waves is the resulting inability to detect surface stresses and the variation in stress through the thickness. In many applications, knowledge of the surface stress and the in-plane stress distribution in the depth direction are highly desired; thus, Rayleigh wave acoustoelasticity is suggested. Rayleigh waves travel at the free surface of a solid half space and the amplitudes decrease rapidly with depth. The depth of penetration into the solid is approximately one wavelength. In a stress-free isotropic material, the phase velocity of Rayleigh wave propagation is a constant and independent of wave frequency; thus, it is not dispersive. When stresses or strains are applied to the material, they cause (via the acoustoelastic effect) a slight change in the elastic properties. This, in turn, is responsible for changes in the elastic wave propagation. If an isotropic half space is subjected to a static, pure homogeneous deformation, it has been shown that the wave

motion does not differ substantially from that formulated in linear wave theory and there is no dispersion. However, when the initial deformation has a distribution in the direction of the depth, the degree of change in the elastic properties also varies with depth. In this sense, the material subjected to such a deformation is qualitatively similar to that of a layered or stratified material. In this case, Rayleigh waves are known to be dispersive. This effect has been studied both theoretically and experimentally by Hirao, et al., [35] where the dispersion of Rayleigh waves for a plate in pure bending was investigated. They found dispersion to be pronounced for relatively low frequencies and to diminish as the frequency increased. In this Chapter, their study will be extended to the case in which the stress distribution in the depth direction can be expressed as a polynomial series so as to investigate surface residual stress in a more general sense. As scanning acoustic microscopy is feasible for a broad range of frequencies and can effectively excite Rayleigh waves in the defocused mode, this technique will be a powerful tool to study surface residual stress fields.

4.1 Theory

First, let us consider Rayleigh wave propagation on the free surface of a semi-infinite homogeneous isotropic material which is initially under static deformation. The coordinate system for the half space is shown in Fig. 4.1. From the governing equation (2-37) in Chapter II and with the aid of equilibrium equation (2-15), we have:

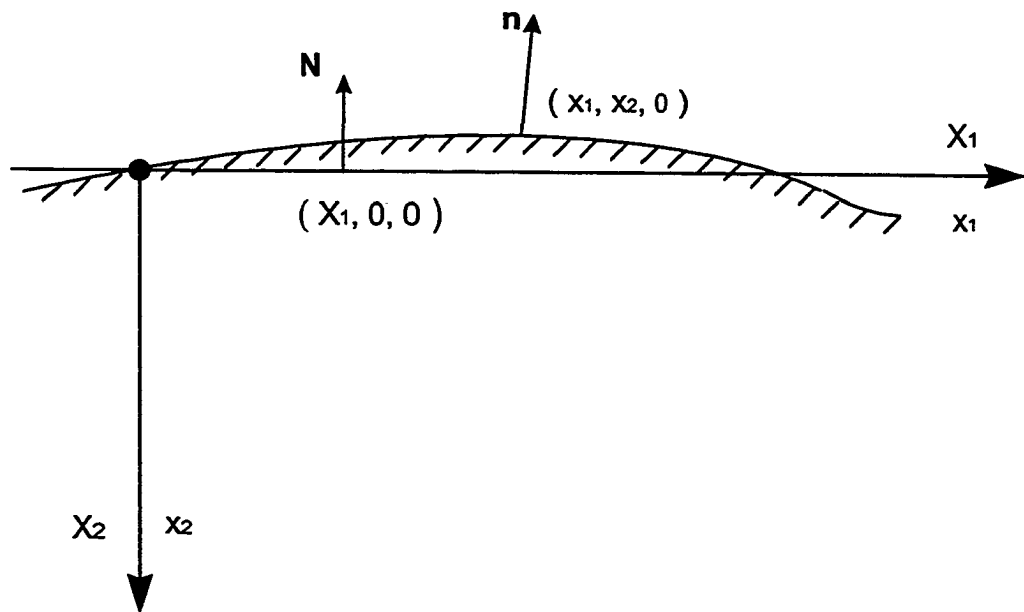


Fig. 4.1 Surface wave over a deformed half space.

$$\frac{\partial}{\partial X_J} (C_{IJKL} \frac{\partial u_K}{\partial X_L}) + \sigma_{JL} \frac{\partial^2 u_I}{\partial X_L \partial X_J} = \rho \frac{\partial^2 u_I}{\partial t^2} \quad (4-1)$$

In the study of this Chapter, several assumptions were made as follows:

- the principal directions are known and aligned with the coordinate axes
- the strain is uniform in the half space other than in the direction X_2
- $\sigma_{22} = 0$, as the region of interest is close to the free surface
- Rayleigh waves propagate in a straight line in the X_1 direction.

With the above assumptions, the Rayleigh wave displacement components have the form

$$u_1 = f_1(X_2) \exp[ik(X_1 - Vt)] \quad (4-2a)$$

$$u_2 = f_2(X_2) \exp[ik(X_1 - Vt)] \quad (4-2b)$$

$$u_3 = 0 \quad (4-2c)$$

Equation (4-2c) represents a conventional treatment since this mode corresponds to the shear wave in the half space which is not related to the Rayleigh wave. In the preceding equations, k denotes the wave number, V the phase velocity, f_1 and f_2 the amplitudes which decay with depth.

Substituting equation (4-2) into equation (4-1) leads to

$$[\mu V^2 / V_T^2 - (\sigma_{11} + C_{1111}) + D(C_{1212}D)]f_1 + i[(C_{1212} + C_{1122})D + DC_{1212}]f_2 = 0 \quad (4-3a)$$

$$[\mu V^2 / V_T^2 - (\sigma_{11} + C_{1212}) + D(C_{2222}D)]f_2 + i[(C_{1212} + C_{1122})D + DC_{1212}]f_1 = 0 \quad (4-3b)$$

where

$$V_T = \sqrt{\mu / \rho} \quad (4-4)$$

$$D = d / d(kX_2) \quad (4-5)$$

We define

$$f_1 = -i[(C_{1212} + C_{1122})D + DC_{1212}]F \quad (4-6a)$$

$$f_2 = [\mu V^2 / V_T^2 - (\sigma_{11} + C_{1111}) + D(C_{1212}D)]F \quad (4-6b)$$

Substituting equations (4-6) into equations (4-3), equation (4-3a) is automatically satisfied and equation (4-3b) leads to a fourth order governing differential equation given by

$$\begin{aligned} & [\mu V^2 / V_T^2 - (\sigma_{11} + C_{1111}) + D(C_{1212}D)][\mu V^2 / V_T^2 - (\sigma_{11} + C_{1212}) + D(C_{2222}D)]F \\ & + [(C_{1212} + C_{1122})D + DC_{1212}][(C_{1212} + C_{1122})D + DC_{1122}]F = 0 \end{aligned} \quad (4-7)$$

As far as boundary conditions are concerned, in the initial state, the surface tractions T_i are given by

$$T_i = \sigma_{ij}l_j = 0 \quad \text{at } X_2 = 0 \quad (4-8)$$

where l_j are the direction cosines of the normal to the surface.

In the final state, the surface tractions become

$$T_i + T'_i = (\sigma_{ij} + \sigma'_{ij})(l_j + l'_j) = 0 \quad \text{at } X_2 = 0 \quad (4-9)$$

where $\sigma_{ij} + \sigma'_{ij}$ and $l_j + l'_j$ are the stress components and direction cosines of the normal to the surface, respectively. Since the superimposed disturbance wave is very small, σ'_{ij} and l'_j are small terms. Neglecting the multipliers of the high order terms, we obtain

$$T'_i = \sigma'_{ij}l_j + \sigma_{ij}l'_j = 0 \quad \text{at } X_2 = 0 \quad (4-10)$$

It has been shown that [30]

$$\sigma'_{IJ} = -\sigma_{IJ} \frac{\partial u_K}{\partial X_K} + \sigma_{IK} \frac{\partial u_J}{\partial X_K} + \sigma_{JK} \frac{\partial u_I}{\partial X_K} + C_{IJKL} \frac{\partial u_K}{\partial X_L} \quad (4-11)$$

and

$$l'_J = \frac{1}{2} l_J l_M l_N \left(\frac{\partial u_M}{\partial X_N} + \frac{\partial u_N}{\partial X_M} \right) - l_M \frac{\partial u_M}{\partial X_J} \quad (4-12)$$

Taking note of the fact that u_1 and u_2 are not functions of X_3 and, in the initial state,

$$l_J = \begin{pmatrix} 0 \\ -1 \\ 0 \end{pmatrix} \quad (4-13)$$

we have

$$l'_1 = \frac{\partial u_2}{\partial X_1} \quad (4-14)$$

and

$$l'_2 = l'_3 = 0 \quad (4-15)$$

Thus, the boundary conditions yield

$$\sigma_{22} = 0 \quad (4-16a)$$

$$\sigma_{11} \frac{\partial u_2}{\partial X_1} - \sigma'_{12} = 0 \quad (4-16b)$$

$$\sigma'_{22} = 0 \quad (4-16c)$$

$$\sigma'_{32} = 0 \quad (4-16d)$$

on the surface $X_2 = 0$. As $\sigma_{IJ} = 0$ if $I \neq J$, the last equation (4-16d) is automatically satisfied. Equations (4-16b) and (4-16c) are relevant to Rayleigh waves. This leads to [30]

$$\frac{\partial u_1}{\partial X_2} + \frac{\partial u_2}{\partial X_1} = 0 \quad (4-17a)$$

and

$$C_{1122} \frac{\partial u_1}{\partial X_1} + C_{2222} \frac{\partial u_2}{\partial X_2} = 0 \quad (4-17b)$$

With the aid of equations (4-2), the boundary conditions (in term of f_1 and f_2) can be rewritten as

$$Df_1 + if_2 = 0 \quad (4-18a)$$

$$iC_{1122}f_1 + C_{2222}Df_2 = 0 \quad (4-18b)$$

Since a general solution which satisfies both the governing equation (4-7) and boundary condition (4-18) is not readily available, we seek a first order perturbation solution for F .

Let

$$F = F^0 + F^1 \quad (4-19)$$

where F^0 is the zeroth order solution when the initial stress is absent and F^1 is the first order solution corresponding to a small perturbation from F^0 because of stress. With the same scheme, the differential operator in equation (4-7) can be written as

$$L = L_0 + L_1 \quad (4-20)$$

From equation (2-46), with $\theta = e_{MM}$, we have

$$\begin{aligned}
C_{1111} &= \lambda + 2\mu + (-\lambda - 2\mu + \nu_1 + 2\nu_2)\theta + 4(\lambda + 2\mu + \nu_2 + 2\nu_3)e_{11} \\
C_{2222} &= \lambda + 2\mu + (-\lambda - 2\mu + \nu_1 + 2\nu_2)\theta + 4(\lambda + 2\mu + \nu_2 + 2\nu_3)e_{22} \\
C_{1212} &= \mu + (-\mu + \nu_2)\theta + 2(\mu + \nu_3)(e_{11} + e_{22}) \\
C_{1122} &= \lambda + (-\lambda + \nu_1)\theta + 2(\lambda + \nu_2)(e_{11} + e_{22})
\end{aligned} \tag{4-21}$$

Define

$$\begin{aligned}
C_{1111}^0 &= \lambda + \mu \\
C_{1111}^1 &= (-\lambda - 2\mu + \nu_1 + 2\nu_2)\theta + 4(\lambda + 2\mu + \nu_2 + 2\nu_3)e_{11} \\
C_{2222}^0 &= \lambda + 2\mu \\
C_{2222}^1 &= (-\lambda - 2\mu + \nu_1 + 2\nu_2)\theta + 4(\lambda + 2\mu + \nu_2 + 2\nu_3)e_{22} \\
C_{1212}^0 &= \mu \\
C_{1212}^1 &= (-\mu + \nu_2)\theta + 2(\mu + \nu_3)(e_{11} + e_{22}) \\
C_{1122}^0 &= \lambda \\
C_{1122}^1 &= (-\lambda + \nu_1)\theta + 2(\lambda + \nu_2)(e_{11} + e_{22})
\end{aligned} \tag{4-22}$$

Then

$$\begin{aligned}
C_{1111} &= C_{1111}^0 + C_{1111}^1 \\
C_{2222} &= C_{2222}^0 + C_{2222}^1 \\
C_{1212} &= C_{1212}^0 + C_{1212}^1 \\
C_{1122} &= C_{1122}^0 + C_{1122}^1
\end{aligned} \tag{4-23}$$

Thus, equation (4-7) yields

$$(L_0 + L_1)(F^0 + F^1) = 0 \quad (4-24)$$

In explicit form, this is

$$\begin{aligned} & \{\mu V_0^2 / V_{T0}^2 + \mu E - (\sigma_{11} + C_{1111}^0 + C_{1111}^1) + D[(C_{1212}^0 + C_{1212}^1)D]\} \\ & \times \{\mu V_0^2 / V_{T0}^2 + \mu E - (\sigma_{11} + C_{1212}^0 + C_{1212}^1) + D[(C_{2222}^0 + C_{2222}^1)D]\}(F^0 + F^1) \\ & + [(C_{1212}^0 + C_{1212}^1 + C_{1122}^0 + C_{1122}^1)D + D(C_{1212}^0 + C_{1212}^1)] \\ & \times [(C_{1212}^0 + C_{1212}^1 + C_{1122}^0 + C_{1122}^1)D + D(C_{1212}^0 + C_{1212}^1)](F^0 + F^1) = 0 \end{aligned} \quad (4-25)$$

where

$$z = 2 \frac{\Delta V V_0}{V_{T0}^2} \quad (4-26)$$

Collecting the zeroth order terms in the above differential equation, we have

$$L_0 F^0 = 0 \quad (4-27)$$

or

$$\begin{aligned} & [\mu \frac{V_0^2}{V_{T0}^2} - C_{1111}^0 + C_{1212}^0 D^2][\mu \frac{V_0^2}{V_{T0}^2} - C_{1212}^0 + C_{2222}^0 D^2]F^0 \\ & + (C_{1212}^0 + C_{1122}^0)^2 D^2 F^0 = 0 \end{aligned} \quad (4-28)$$

Applying equation (4-22) and letting

$$n_1 = (1 - \frac{V_0^2}{V_{T0}^2})^{1/2} \quad (4-29)$$

$$n_2 = (1 - \frac{V_0^2}{KV_{T0}^2})^{1/2} \quad (4-30)$$

where

$$K = \frac{\lambda + 2\mu}{\mu} \quad (4-31)$$

equation (4-28) can be simplified to

$$D^4 F^0 - (n_1^2 + n_2^2) D^2 F^0 + n_1^2 n_2^2 F^0 = 0 \quad (4-32)$$

The general solution to this fourth order differential equation is

$$F^0 = \sum_{i=1}^2 A_i \exp(-n_i k X_2) + \sum_{i=1}^2 B_i \exp(n_i k X_2) \quad (4-33)$$

However, since F should tend to zero as X_2 tends to infinity, B_i must be zero. We then obtain the zeroth order solution

$$F^0 = \sum_{i=1}^2 A_i \exp(-n_i k X_2) \quad (4-34)$$

Collecting the first order terms in equation (4-25), we obtain

$$L_0 F^1 + L_1 F^0 = 0 \quad (4-35)$$

or

$$\begin{aligned} & \mu^2 \{ K D^4 + D^2 \{ (K+1) \frac{V_0^2}{V_{T0}^2} - 2K \} + (\frac{V_0^2}{V_{T0}^2} - K) (\frac{V_0^2}{V_{T0}^2} - 1) \} F^1 \\ & + (\mu \frac{V_0^2}{V_{T0}^2} - C_{1111}^0 + C_{1212}^0 D^2) (\mu z - \sigma_{11} + C_{1212}^1 + C_{2222}^1 D^2 + D C_{2222}^1 D) F^0 \\ & + (C_{1212}^0 + C_{1122}^0) D [(C_{1212}^1 + C_{1122}^1) D + D C_{1212}^1] F^0 \\ & + [(C_{1212}^1 + C_{1122}^1) D + D C_{1122}^1] [(C_{1212}^0 + C_{1122}^0) D] F^0 \\ & + [\mu z - (\sigma_{11} + C_{1111}^1) + C_{1212}^1 D^2 + D C_{1212}^1 D] [\mu \frac{V_0^2}{V_{T0}^2} - C_{1212}^0 + C_{2222}^0 D^2] F^0 = 0 \end{aligned} \quad (4-36)$$

We define

$$\begin{aligned}
 r_0 &= \frac{2\mu}{\lambda} \\
 r_1 &= \frac{-\lambda + v_1}{\mu} \\
 r_2 &= -1 + \frac{v_2}{\mu} \\
 r_3 &= \frac{\lambda + v_2}{\mu} \\
 r_4 &= 1 + \frac{v_3}{\mu}
 \end{aligned} \tag{4-37}$$

Substituting equations (4-22) and (4-37) into equation (4-36) and taking into account the following equation

$$\sigma_{22} = \lambda\theta + 2\mu e_{22} = 0 \tag{4-38}$$

or

$$\theta = \frac{-2\mu}{\lambda} e_{22} = r_0 e_{22} \tag{4-39}$$

after complicated algebraic manipulation, we have

$$\begin{aligned}
 &K[D^4 + (n_1^2 + n_2^2)D^2 + n_1^2 n_2^2]F^1 + \{z[n_i^2 - n_1^2 + K(n_i^2 - n_2^2)] \\
 &+ L_i^{(1)}e_{11} + L_i^{(2)}e_{22} + M_i^{(1)}De_{11} + M_i^{(2)}De_{22}\}F^0 = 0
 \end{aligned} \tag{4-40}$$

where

$$L_i^{(1)} = 2Kr_4 n_i^4 + 2n_i^2 \left[\left(\frac{V_0^2}{V_{70}^2} - 4 \right) r_4 - K(1 + 2r_4) - 1 - 2r_3 \right]$$

$$\begin{aligned}
& + 2n_1^2(1 + 2r_3 + 4r_4) + 2K(1 + r_4)n_2^2 \\
L_i^{(2)} &= n_i^4[r_0(r_1 + 2r_2) + 4(r_3 + 2r_4) + K(r_0r_2 + 2r_4)] \\
& + n_i^2 \left\{ \frac{V_0^2}{V_{T0}^2} [r_0(r_1 + 3r_2) + 4r_3 + 10r_4] + 2K[1 - r_0r_2 - 2r_4] \right. \\
& \quad \left. + 2[2 - r_0r_1 - 2r_0r_2 - 2r_4] \right\} - Kn_2^2(2 - r_0r_2 - 2r_4) - n_1^2(2 - r_0r_2 - r_0r_1) \\
M_i^{(1)} &= 2n_i[(n_1^2 - Kn_i^2)r_4 - (K - 1)(r_3 + r_4)] \\
M_i^{(2)} &= -n_i \{ [r_0(r_1 + 2r_2) + 4(r_3 + 2r_4)]n_i^2 + (r_0r_2 + 2r_4)(Kn_i^2 - n_1^2) \\
& \quad - K[r_0(r_1 + 2r_2) + 4(r_3 + 2r_4)]n_2^2 + (K - 1)[(r_1 + r_2)r_0 + 2(r_3 + r_4)] \}
\end{aligned} \tag{4-41}$$

Let

$$R_i(X_2) = [n_i^2 - n_1^2 + K(n_i^2 - n_2^2)]z + \sum_{l=1}^2 (L_i^{(l)}e_{ll} + M_i^{(l)}De_{ll}) \tag{4-42}$$

Then, equation (4-40) becomes

$$K[D^4 + (n_1^2 + n_2^2)D^2 + n_1^2n_2^2]F^1 = -R_i(X_2)F^0 \tag{4-43}$$

Since

$$\begin{aligned}
& [D^4 + (n_1^2 + n_2^2)D^2 + n_1^2n_2^2]F^1 \\
& = (D - n_1)(D + n_1)(D - n_2)(D + n_2) = G(D)F^1
\end{aligned} \tag{4-44}$$

and

$$\frac{1}{G(D)} = \frac{1}{2n_1n_2(n_1^2 - n_2^2)} \left[\frac{n_2}{D - n_1} - \frac{n_2}{D + n_1} - \frac{n_1}{D - n_2} + \frac{n_1}{D + n_2} \right] \tag{4-45}$$

the first order solution is obtained as

$$F^1 = h \sum_{i=1}^2 A_i [n_2 e^{n_1 k X_2} \int_{\infty}^{k X_2} R_i e^{-(n_1+n_2)t} dt - n_1 e^{n_2 k X_2} \int_{\infty}^{k X_2} R_i e^{-(n_1+n_2)t} dt \\ - n_2 e^{n_1 k X_2} \int_0^{k X_2} R_i e^{-(n_1-n_2)t} dt + n_1 e^{n_2 k X_2} \int_0^{k X_2} R_i e^{-(n_1-n_2)t} dt] \quad (4-46)$$

where

$$h = [2Kn_1n_2(n_1^2 - n_2^2)]^{-1} \quad (4-47)$$

Thus, we have the solution

$$F = F^0 + F^1 = \sum_{i=1}^2 A_i \exp(n_i k X_2) \\ + h \sum_{i=1}^2 A_i [n_2 e^{n_1 k X_2} \int_{\infty}^{k X_2} R_i e^{-(n_1+n_2)t} dt - n_1 e^{n_2 k X_2} \int_{\infty}^{k X_2} R_i e^{-(n_1+n_2)t} dt \\ - n_2 e^{n_1 k X_2} \int_0^{k X_2} R_i e^{-(n_1-n_2)t} dt + n_1 e^{n_2 k X_2} \int_0^{k X_2} R_i e^{-(n_1-n_2)t} dt] \quad (4-48)$$

Applying solution F to boundary condition (4-18a), it turns out to be

$$-Di[(C_{1212} + C_{1122})D + DC_{1212}]F \\ + i[\mu V^2 / V_{T0}^2 - (\sigma_{11} + C_{1111}) + D(C_{1212}D)]F = 0 \quad \text{at } X_2 = 0 \quad (4-49)$$

With the aid of equation (4-23), the above equation becomes

$$-[(C_{1212}^0 + C_{1122}^0)D^2 + DC_{1122}^1 D + (C_{1212}^1 + C_{1122}^1)D^2](F_0 + F_1) \\ + [\mu V_0^2 / V_{T0}^2 + \mu E - C_{1111}^0 - (\sigma_{11} + C_{1111}^1) + DC_{1212}^1 D + C_{1212}^0 D^2 + C_{1212}^1 D^2](F_0 + F_1) \\ - [DC_{1212}^1 D + DC_{1122}^1 D + D^2 C_{1212}^1](F_0 + F_1) = 0 \quad \text{at } X_2 = 0 \quad (4-50)$$

Neglecting the second order terms, we have

$$[-Kn_2^2 - (K-2)n_i^2 + z - U_{li}^{(1)} \overline{e_{11}} - U_{li}^{(2)} \overline{e_{22}}]F^0$$

$$-(K-2)D^2 F^1 - Kn_2^2 F^1 + V_{li}^{(1)} \overline{De_{11}} + V_{li}^{(2)} \overline{De_{22}} - W_{li}^{(1)} \overline{D^2 e_{11}} - W_{li}^{(2)} \overline{D^2 e_{22}} = 0 \quad (4-51)$$

where

$$\begin{aligned} U_{li}^{(1)} &= 2 + 4r_3 + 8r_4 + 2n_i^2 r_3 \\ U_{li}^{(2)} &= -2 + (r_1 + 2r_2)r_0 + (r_1 r_0 + 2r_3)n_i^2 \\ V_{li}^{(1)} &= 2(r_3 + r_4)n_i \\ V_{li}^{(2)} &= r_0(r_1 + r_2) + 2(r_3 + r_4)n_i \\ W_{li}^{(1)} &= 2r_4 \\ W_{li}^{(2)} &= r_0 r_2 + 2r_4 \end{aligned} \quad (4-52)$$

and the bars over the strains and their derivatives indicate values at the free surface

$$x_2 = 0.$$

Substituting F into the boundary condition (4-18b), we obtain

$$\begin{aligned} &C_{1122}[(C_{1212} + C_{1122})D + DC_{1212}]F \\ &+ C_{2222}D[\mu V^2 / V_{T0}^2 - (\sigma_{11} + C_{1111}) + D(C_{1212}D)]F = 0 \end{aligned} \quad (4-53)$$

Similar to the first boundary condition, the above equation can be expressed as

$$\begin{aligned} &(C_{1122}^0 + C_{1122}^1)[(C_{1212}^0 + C_{1122}^1)D + (C_{1212}^1 + C_{1212}^1)D + DC_{1212}^1](F^0 + F^1) \\ &+ (C_{2222}^0 + C_{2222}^1)[\mu V^2 / V_{T0}^2 + \mu \varepsilon - C_{1111}^0 - (\sigma_1 + C_{1111}^1) \\ &+ 2DC_{1212}^1 D + C_{1212}^0 D^2 + C_{1212}^1 D^2]D(F_0 + F_1) \\ &+ (C_{2222}^0 + C_{2222}^1)[-D(\sigma_{11} + C_{1111}^1) + D^2 C_{1212}^1 D](F_0 + F_1) = 0 \end{aligned} \quad (4-54)$$

For the first order approach, equation (4-54) yields

$$\begin{aligned}
& -n_i[(k-1)(k-2) - K^2 n_2^2 + Kz + Kn_i^2]F^0 + [U_{2i}^{(1)} \overline{e_{11}} + U_{2i}^{(2)} \overline{e_{22}} \\
& + V_{2i}^{(1)} \overline{De_{11}} + V_{2i}^{(2)} \overline{De_{22}} + W_{2i}^{(1)} \overline{De_{11}} + W_{2i}^{(2)} \overline{De_{22}}]F^0 \\
& + [(K-1)(K-2) - K^2 n_2^2]DF^1 + KD^3 F^1 = 0
\end{aligned} \tag{4-55}$$

where

$$\begin{aligned}
U_{2i}^{(1)} &= 2n_i[K(1+3r_4) + (3r_3 + 2r_4)] - 2Kr_4 n_i^3 \\
U_{2i}^{(2)} &= -n_i \{(-Kn_2^2 + n_i^2)[r_0(r_1 + 2r_2) + 4(r_3 + 2r_4)] \\
& \quad + K[r_0(r_1 - r_2) + 2(2r_3 + r_4) + 2]\} \\
V_{2i}^{(1)} &= 2[-K(1+2r_3) + r_4(2Kn_i^2 - 3K - 2)] \\
V_{2i}^{(2)} &= (r_0 r_2 + 2r_4)(2Kn_i^2 + K - 2) + K[2 - r_0(r_1 + 2r_2)] \\
W_{2i}^{(1)} &= -2Kr_4 n_i \\
W_{2i}^{(2)} &= -K(r_0 r_2 + 2r_4)n_i
\end{aligned} \tag{4-56}$$

From equation (4-46), the derivative to the first order solution F^1 yields

$$\begin{aligned}
DF^1 &= h \sum_{i=1}^2 A_i [n_1 n_2 e^{\eta_1 k X_2} \int_{\infty}^{kX_2} R_i e^{-(n_1+n_2)t} dt - n_1 n_2 e^{\eta_2 k X_2} \int_{\infty}^{kX_2} R_i e^{-(n_1+n_2)t} dt \\
& \quad + n_1 n_2 e^{\eta_1 k X_2} \int_0^{kX_2} R_i e^{-(n_1-n_1)t} dt - n_1 n_2 e^{\eta_2 k X_2} \int_0^{kX_2} R_i e^{-(n_1-n_2)t} dt] \\
& \quad + n_2 R_i e^{-\eta_1 k X_2} - n_1 R_i e^{-\eta_1 k X_2} - n_2 R_i e^{-\eta_1 k X_2} + n_1 R_i e^{-\eta_1 k X_2} \\
&= h \sum_{i=1}^2 A_i [n_1 n_2 e^{\eta_1 k X_2} \int_{\infty}^{kX_2} R_i e^{-(n_1+n_2)t} dt - n_1 n_2 e^{\eta_2 k X_2} \int_{\infty}^{kX_2} R_i e^{-(n_1+n_2)t} dt \\
& \quad + n_1 n_2 e^{\eta_1 k X_2} \int_0^{kX_2} R_i e^{-(n_1-n_1)t} dt - n_1 n_2 e^{\eta_2 k X_2} \int_0^{kX_2} R_i e^{-(n_1-n_2)t} dt]
\end{aligned} \tag{4-57}$$

For the second order derivative, we have

$$\begin{aligned}
D^2 F^1 &= h \sum_{i=1}^2 A_i [n_1^2 n_2 e^{n_1 k X_2} \int_{\infty}^{k X_2} R_i e^{-(n_1+n_2)t} dt - n_1 n_2^2 e^{n_2 k X_2} \int_{\infty}^{k X_2} R_i e^{-(n_1+n_2)t} dt \\
&\quad - n_1^2 n_2 e^{n_1 k X_2} \int_0^{k X_2} R_i e^{-(n_1-n_1)t} dt + n_1 n_2^2 e^{n_2 k X_2} \int_0^{k X_2} R_i e^{-(n_1-n_2)t} dt] \\
&\quad + n_1 n_2 R_i e^{-n_1 k X_2} - n_1 n_2 R_i e^{-n_1 k X_2} - n_1 n_2 R_i e^{-n_1 k X_2} + n_1 n_2 R_i e^{-n_1 k X_2} \quad (4-58) \\
&= h \sum_{i=1}^2 A_i [n_1^2 n_2 e^{n_1 k X_2} \int_{\infty}^{k X_2} R_i e^{-(n_1+n_2)t} dt - n_1 n_2^2 e^{n_2 k X_2} \int_{\infty}^{k X_2} R_i e^{-(n_1+n_2)t} dt \\
&\quad - n_1^2 n_2 e^{n_1 k X_2} \int_0^{k X_2} R_i e^{-(n_1-n_1)t} dt + n_1 n_2^2 e^{n_2 k X_2} \int_0^{k X_2} R_i e^{-(n_1-n_2)t} dt]
\end{aligned}$$

Continuing, the third order derivative becomes

$$\begin{aligned}
D^3 F^1 &= h \sum_{i=1}^2 A_i [n_1^3 n_2 e^{n_1 k X_2} \int_{\infty}^{k X_2} R_i e^{-(n_1+n_2)t} dt - n_1 n_2^3 e^{n_2 k X_2} \int_{\infty}^{k X_2} R_i e^{-(n_1+n_2)t} dt \\
&\quad + n_1^3 n_2 e^{n_1 k X_2} \int_0^{k X_2} R_i e^{-(n_1-n_1)t} dt - n_1 n_2^3 e^{n_2 k X_2} \int_0^{k X_2} R_i e^{-(n_1-n_2)t} dt] \\
&\quad + n_1^2 n_2 R_i e^{-n_1 k X_2} - n_1 n_2^2 R_i e^{-n_1 k X_2} - n_1^2 n_2 R_i e^{-n_1 k X_2} + n_1 n_2^2 R_i e^{-n_1 k X_2} \quad (4-59) \\
&= h \sum_{i=1}^2 A_i [n_1^3 n_2 e^{n_1 k X_2} \int_{\infty}^{k X_2} R_i e^{-(n_1+n_2)t} dt - n_1 n_2^3 e^{n_2 k X_2} \int_{\infty}^{k X_2} R_i e^{-(n_1+n_2)t} dt \\
&\quad - n_1^3 n_2 e^{n_1 k X_2} \int_0^{k X_2} R_i e^{-(n_1-n_1)t} dt + n_1 n_2^3 e^{n_2 k X_2} \int_0^{k X_2} R_i e^{-(n_1-n_2)t} dt]
\end{aligned}$$

From the above equations, we obtain

$$-(K-2)D^2 F^1 - K n_2^2 F^1 = \sum_{i=1}^2 n_2 h (K-1) A_i [(n_1^2 + 1) I_{i1} - 2 n_1 n_2 I_{i2}] \quad (4-60)$$

$$(K-1)(K-2)DF^1 - K^2 n_2^2 DF^1 + KD^3 F^1$$

$$= h \sum_{i=1}^2 A_i n_i n_2 (K-1) [2I_{i1} - (1+n_1^2)I_{i2}] \quad (4-61)$$

where

$$I_{ij} = \int_0^\infty k R_i e^{-(n_i+n_j)kX_2} dX_2 = [n_i^2 - n_1^2 + K(n_i^2 - n_2^2)][n_i + n_j]^{-1} \\ + \sum_{l=1}^2 \{-M_i^{(l)} \overline{e_{il}} + [L_i^{(l)} + (n_i + n_j)M_i^{(l)}]E_{ij}^{(l)}\} \quad (4-62)$$

and

$$E_{ij}^{(l)} = \int_0^\infty k e_{il} e^{-(n_i+n_j)kX_2} dX_2 \quad (4-63)$$

Then, the boundary conditions become

$$\sum_{i=1}^2 [-Kn_2^2 - (K-2)n_i^2 + z + U_{li}^{(1)} \overline{e_{11}} + U_{li}^{(2)} \overline{e_{22}} + V_{li}^{(1)} \overline{De_{11}} + V_{li}^{(2)} \overline{De_{22}} \\ + W_{li}^{(1)} \overline{D^2 e_{11}} + W_{li}^{(2)} \overline{D^2 e_{22}} + h(K-1)n_2 \{(1+n_1^2)I_{i1} - 2n_1 n_2 I_{i2}\}] A_i = 0 \quad (4-64)$$

and

$$\sum_{i=1}^2 \{-(K-1)(K-2) - Kn_2^2 + Kn_i^2 + Kz\} n_i + U_{2i}^{(1)} \overline{e_{11}} + U_{2i}^{(2)} \overline{e_{22}} \\ + V_{2i}^{(1)} \overline{De_{11}} + V_{2i}^{(2)} \overline{De_{22}} + W_{2i}^{(1)} \overline{D^2 e_{11}} + W_{2i}^{(2)} \overline{D^2 e_{22}} \\ + h(K-1)n_1 n_2 [2I_{i1} - (1+n_1^2)I_{i2}] A_i = 0 \quad (4-65)$$

The preceding equations can be further expressed in matrix form as

$$(G_{ij} + a_{ij}z + b_{ij}) A_j = 0 \quad (4-66)$$

where

$$G_{11} = -Kn_2^2 - (K-2)n_1^2 = -(K-1)(n_1^2 + 1)$$

$$G_{12} = -Kn_2^2 - (K-2)n_2^2 = -2(K-1)n_2^2$$

$$G_{21} = -[(K-1)(K-2) - K^2n_2^2 - Kn_1^2]n_1 = 2(K-1)n_1$$

$$G_{22} = -[(K-1)(K-2) - K^2n_2^2 - Kn_2^2]n_1 = (K-1)(1+n_1^2)n_2$$

$$a_{11} = 1 + (K-1)\left[\frac{1+n_1^2}{4n_1^2} - \frac{n_2}{n_1+n_2}\right]$$

$$a_{12} = 1 + \frac{K-1}{2K}\left[1 - \frac{1+n_1^2}{n_1(n_1+n_2)}\right]$$

$$a_{21} = -Kn_1 + \frac{K-1}{2n_1}\left[1 - \frac{n_1(1+n_1^2)}{n_1+n_2}\right] \quad (4-67)$$

$$a_{22} = -Kn_2 - \frac{K-1}{K}\left[\frac{1}{n_1+n_2} - \frac{1+n_1^2}{4n_2}\right]$$

$$b_{11} = U_{11}^{(1)}\overline{e_{11}} + U_{11}^{(2)}\overline{e_{22}} + V_{11}^{(1)}\overline{De_{11}} + V_{11}^{(2)}\overline{De_{22}} + W_{11}^{(1)}\overline{D^2e_{11}} + W_{11}^{(2)}\overline{D^2e_{22}}$$

$$+ h(K-1)n_2[(1+n_1^2)I_{11}^{(2)} - 2n_1n_2I_{12}^{(2)}]$$

$$b_{12} = U_{12}^{(1)}\overline{e_{11}} + U_{12}^{(2)}\overline{e_{22}} + V_{12}^{(1)}\overline{De_{11}} + V_{12}^{(2)}\overline{De_{22}} + W_{12}^{(1)}\overline{D^2e_{11}} + W_{12}^{(2)}\overline{D^2e_{22}}$$

$$+ h(K-1)n_2[(1+n_1^2)I_{21}^{(2)} - 2n_1n_2I_{22}^{(2)}]$$

$$b_{21} = U_{21}^{(1)}\overline{e_{11}} + U_{21}^{(2)}\overline{e_{22}} + V_{21}^{(1)}\overline{De_{11}} + V_{21}^{(2)}\overline{De_{22}} + W_{21}^{(1)}\overline{D^2e_{11}} + W_{21}^{(2)}\overline{D^2e_{22}}$$

$$+ h(K-1)n_1n_2[2I_{11}^{(2)} - (1+n_1^2)I_{12}^{(2)}]$$

$$b_{22} = U_{22}^{(1)}\overline{e_{11}} + U_{22}^{(2)}\overline{e_{22}} + V_{22}^{(1)}\overline{De_{11}} + V_{22}^{(2)}\overline{De_{22}} + W_{22}^{(1)}\overline{D^2e_{11}} + W_{22}^{(2)}\overline{D^2e_{22}}$$

$$+ h(K-1)n_1n_2[2I_{21}^{(2)} - (1+n_1^2)I_{22}^{(2)}]$$

$$I_{ij}^{(2)} = \sum_{l=1}^2 \{ -M_i^{(l)} \overline{e_{ll}} + [L_i^{(l)} + (n_i + n_j) M_i^{(l)}] E_{ij}^{(l)} \}$$

The nontrivial solution for A_j requires

$$\left| G_{ij} + a_{ij}z + b_{ij} \right| = 0 \quad (4-68)$$

Here, z and b_{ij} are of the order of the initial strains and are small in comparison with G_{ij} ;

thus, z can be determined with the first order perturbation approach.

The zeroth order solution, which represents the stress-free case, requires

$$\begin{vmatrix} G_{11} & G_{12} \\ G_{21} & G_{22} \end{vmatrix} = 0 \quad (4-69)$$

Solving this equation, the Rayleigh wave velocity for an isotropic medium can be derived. In explicit format, equation (4-68) becomes

$$\begin{vmatrix} G_{11} + a_{11}z + b_{11} & G_{12} + a_{12}z + b_{12} \\ G_{21} + a_{21}z + b_{21} & G_{22} + a_{22}z + b_{22} \end{vmatrix} = 0 \quad (4-70)$$

Neglecting second order terms and with the aid of the zeroth order equation, we obtain

$$z = - \frac{G_{11}b_{22} + G_{22}b_{11} - G_{12}b_{21} - G_{21}b_{12}}{G_{11}a_{22} + G_{22}a_{11} - G_{12}a_{21} - G_{21}a_{12}} \quad (4-71)$$

Then

$$\frac{\Delta V}{V_0} = \frac{zV_{r0}^2}{2V_0^2} \quad (4-72)$$

Obviously, a_{ij} and G_{ij} are functions of the second and third order elastic moduli, and, thus, are constants. It is b_{ij} that reflects the acoustoelastic effect.

If one models the strain distributions through the thickness as an nth order polynomial, then

$$e_{11} = a_0 + a_1 X_2 + a_2 X_2^2 + a_3 X_2^3 + \dots + a_n X_2^n \quad (4-73a)$$

$$e_{22} = b_0 + b_1 X_2 + b_2 X_2^2 + b_3 X_2^3 + \dots + b_n X_2^n \quad (4-73b)$$

and

$$\begin{aligned} \overline{e_{11}} &= a_0 & \overline{e_{22}} &= b_0 \\ \overline{De_{11}} &= a_1 / k & \overline{De_{22}} &= b_1 / k \\ \overline{D^2 e_{11}} &= a_2 / k^2 & \overline{D^2 e_{22}} &= b_2 / k^2 \end{aligned} \quad (4-74)$$

From equation (4-63), we have

$$E_{ij}^{(1)} = \int_0^\infty k e_{11} e^{-(n_i + n_j)kX_2} dX_2 = \int_0^\infty k \left(\sum_{m=0}^n a_m X_2^m \right) e^{-(n_i + n_j)kX_2} dX_2 \quad (4-75)$$

$$E_{ij}^{(2)} = \int_0^\infty k e_{22} e^{-(n_i + n_j)kX_2} dX_2 = \int_0^\infty k \left(\sum_{m=0}^n b_m X_2^m \right) e^{-(n_i + n_j)kX_2} dX_2 \quad (4-76)$$

Since

$$\int_0^\infty t^m e^{kt} dt = \frac{m!}{k^{m+1}} \quad (4-77)$$

we obtain from equations (4-75) and (4-76)

$$E_{11}^{(1)} = \sum_{m=0}^n \frac{a_m m!}{(2n_1)^{m+1} k^m}$$

$$E_{11}^{(2)} = \sum_{m=0}^n \frac{b_m m!}{(2n_1)^{m+1} k^m}$$

$$\begin{aligned}
E_{12}^{(1)} &= E_{21}^{(1)} = \sum_{m=0}^n \frac{a_m m!}{(n_1 + n_2)^{m+1} k^m} \\
E_{12}^{(2)} &= E_{21}^{(2)} = \sum_{m=0}^n \frac{b_m m!}{(n_1 + n_2)^{m+1} k^m} \\
E_{22}^{(1)} &= \sum_{m=0}^n \frac{a_m m!}{(2n_2)^{m+1} k^m} \\
E_{22}^{(2)} &= \sum_{m=0}^n \frac{b_m m!}{(2n_2)^{m+1} k^m}
\end{aligned} \tag{4-78}$$

Thus, the velocity change from the unstressed state may be expressed as

$$\begin{aligned}
\Delta V / V_0 &= \beta_0 a_0 + \beta_1 a_1 / k + \beta_2 a_2 / k^2 + \beta_3 a_3 / k^3 + \dots + \beta_n a_n / k^n \\
&+ \gamma_0 b_0 + \gamma_1 b_1 / k + \gamma_2 b_2 / k^2 + \gamma_3 b_3 / k^3 + \dots + \gamma_n b_n / k^n
\end{aligned} \tag{4-79}$$

where β_i and γ_i are functions of the second and third order elastic constants listed in Appendix A.

It is noted that the relative change of the velocity of the Rayleigh wave is a function of the wave number k . By definition, the Rayleigh wave is dispersive. Thus, by measuring the relative change of the phase velocity of different frequency Rayleigh waves, it will be possible to reconstruct a stress field by measuring these relative velocity changes.

4.2 Numerical Simulation

To further explore the application of Rayleigh wave dispersion to strain reconstruction, consider a special case:

$$\sigma_{11} = \sigma_{22} = 0 \quad (4-80)$$

$$e_{11} = e_{22} = a + bX_2 + cX_2^2 \quad (4-81)$$

For a mild steel with the material constants listed in Table 4.1, we have

$$\Delta V / V_0 = \lambda_0 a + \lambda_1 b / k + \lambda_2 c / k^2 \quad (4-82)$$

$$\lambda_0 = -0.274 \quad \lambda_1 = -0.214 \quad \lambda_2 = -2.55 \quad (4-83)$$

Rayleigh wave dispersions corresponding to different strain fields are shown in Fig. 4.2 through Fig. 4.4. Since there are three constants a , b , and c to be determined, three different frequency Rayleigh waves should be employed. In this simulation, two sets of Rayleigh waves for the reconstruction are utilized: a first set of 1, 5, 10 MHz and a second one of 2, 3, 5 MHz. Reconstruction results are shown in Fig. 4.5 through Fig. 4.10.

Table. 4.1 Material properties of a mild steel.

Density (kg/m ³)	Lamé Constants (× 10 ¹⁰ Pa)		Third-Order Elastic Constants (× 10 ¹⁰ Pa)			Rayleigh Wave Speed (m / sec)
ρ	λ	μ	ν_1	ν_2	ν_3	V_0
7837	10.74	8.19	-1.3	-20.0	-20.0	3109

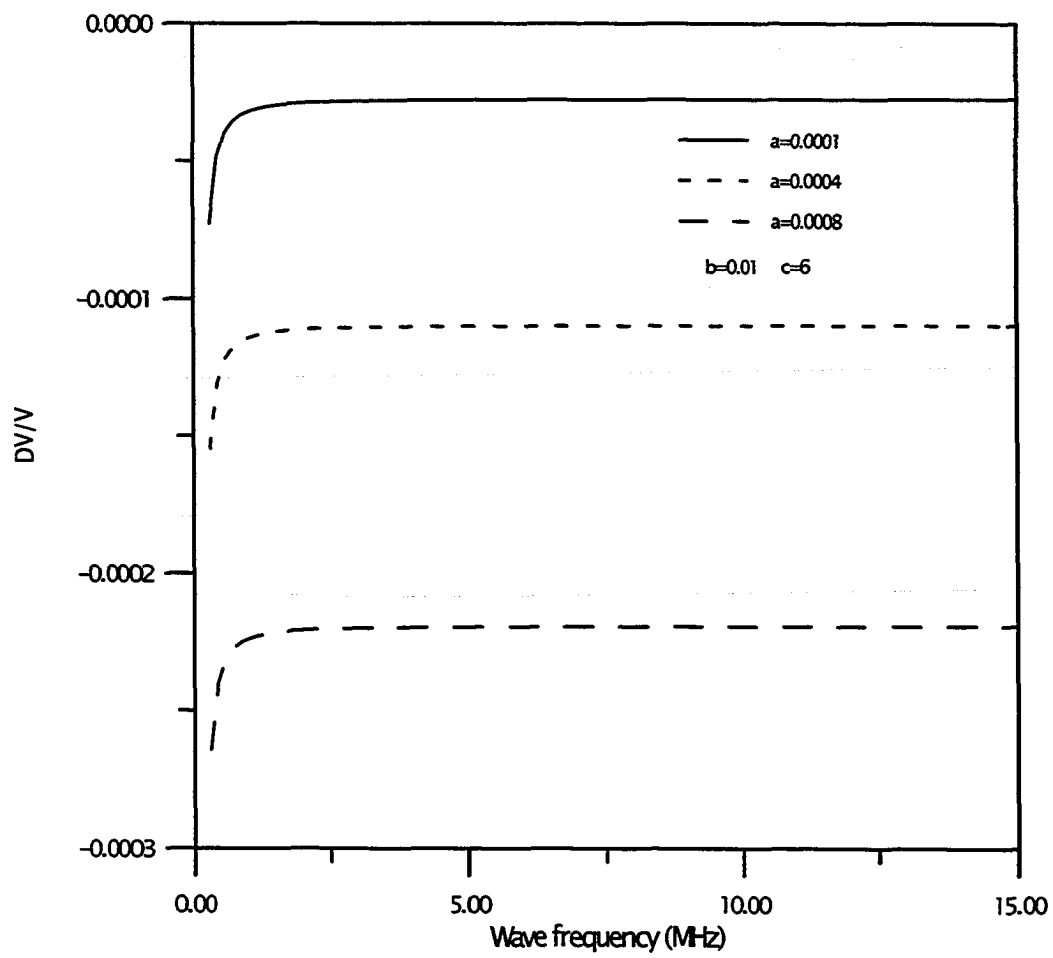


Fig. 4.2 Dispersion of Rayleigh waves for different surface strains.

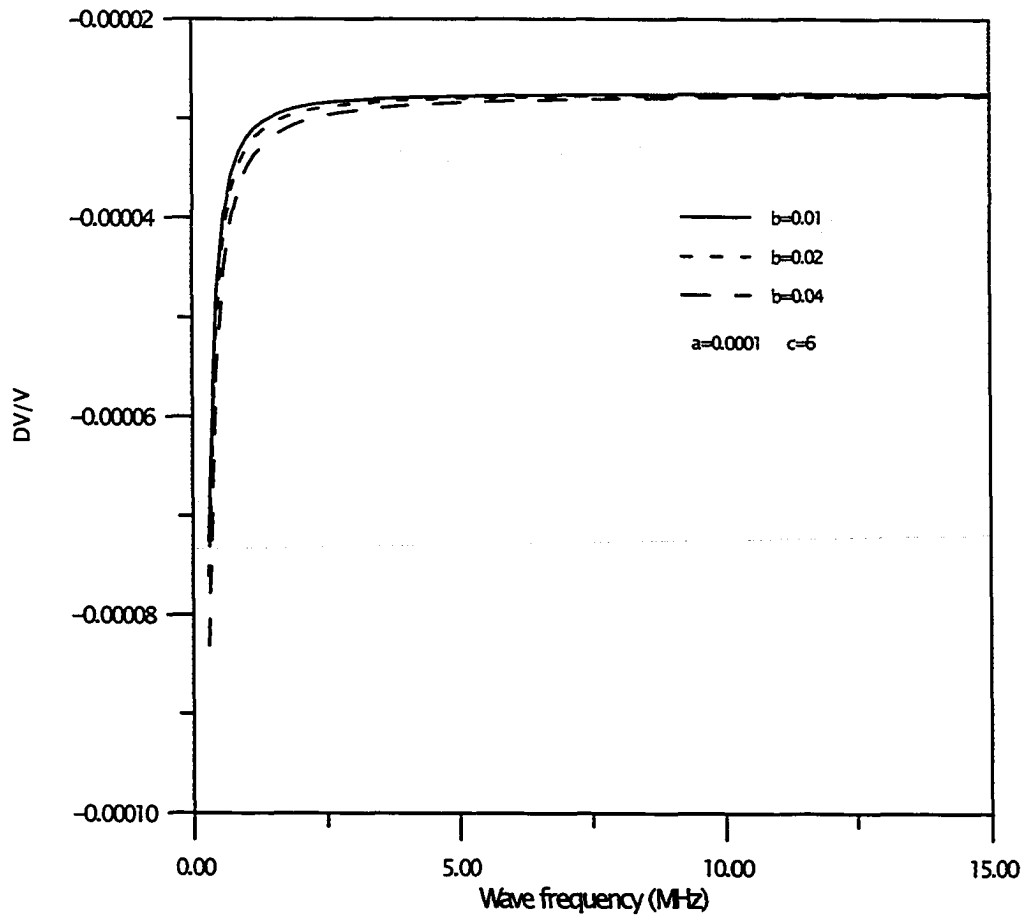


Fig. 4.3 Dispersion of Rayleigh waves for different linear coefficients of strain distribution.

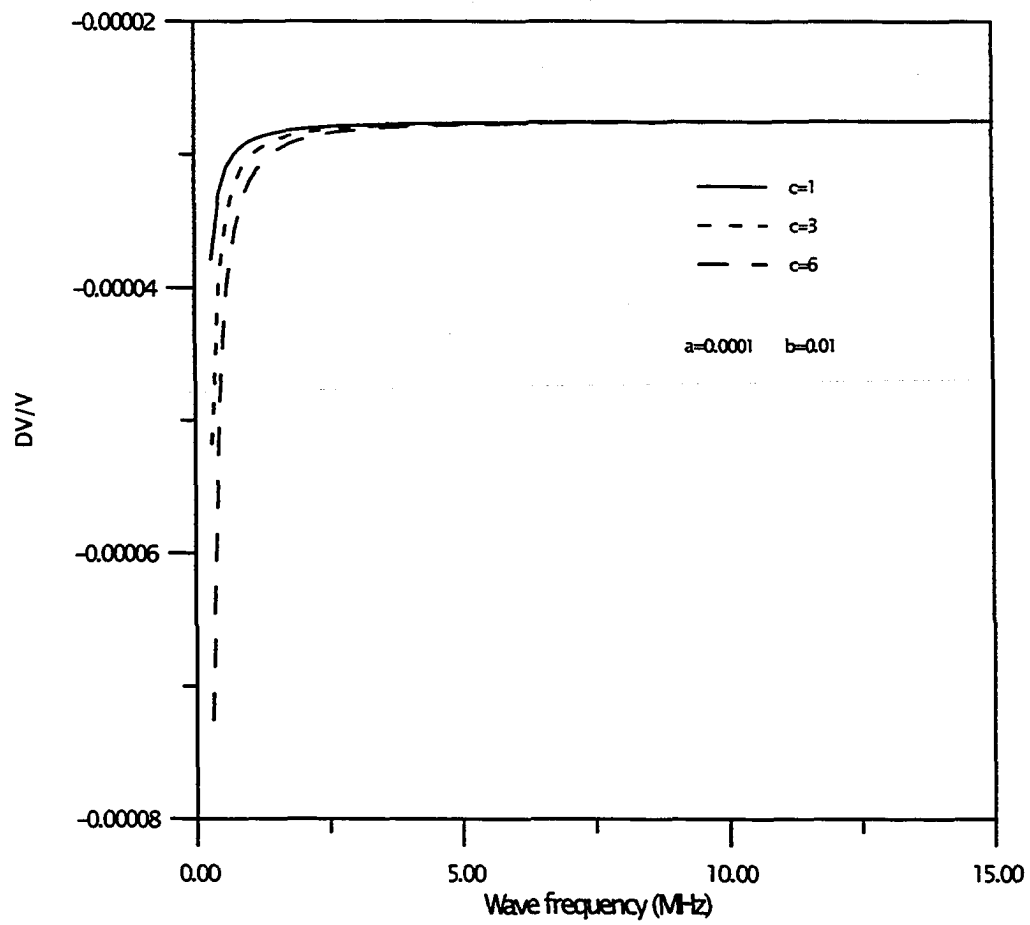


Fig. 4.4 Dispersion of Rayleigh waves for different quadratic coefficients of strain distribution.

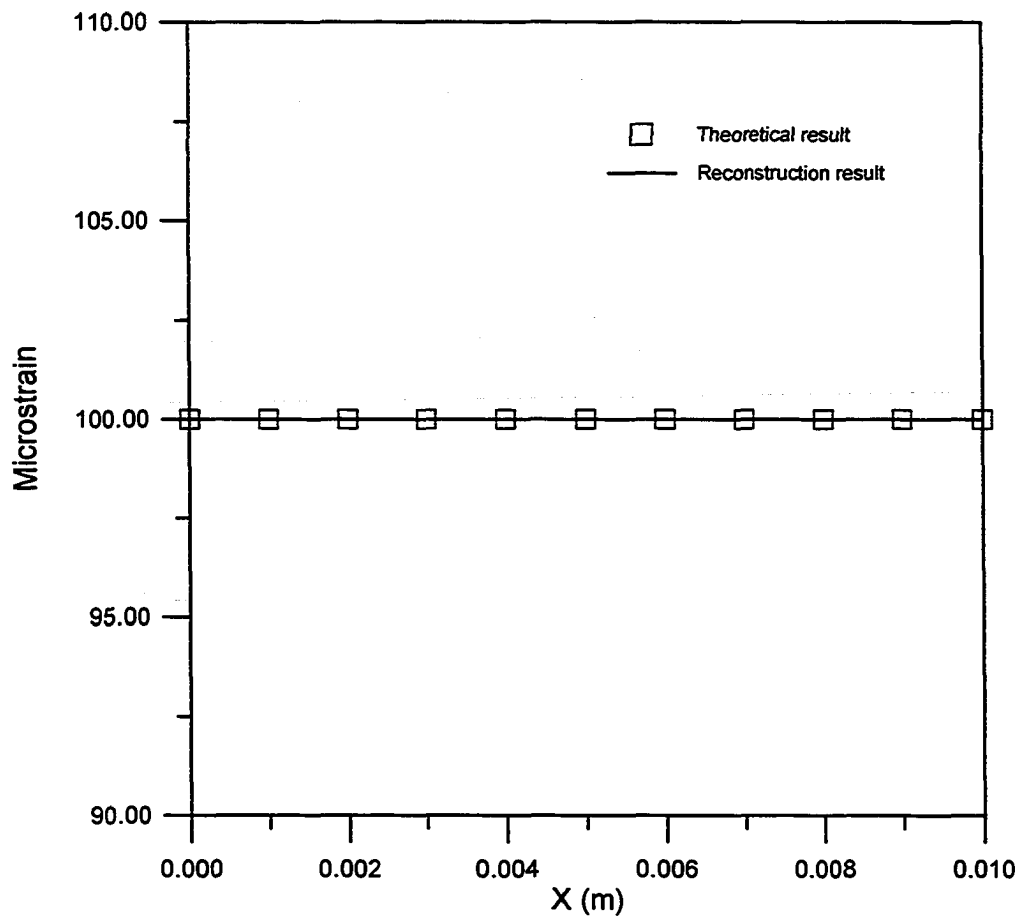


Fig. 4.5 Surface strain field reconstruction using Rayleigh waves of 1, 5, and 10 MHz.

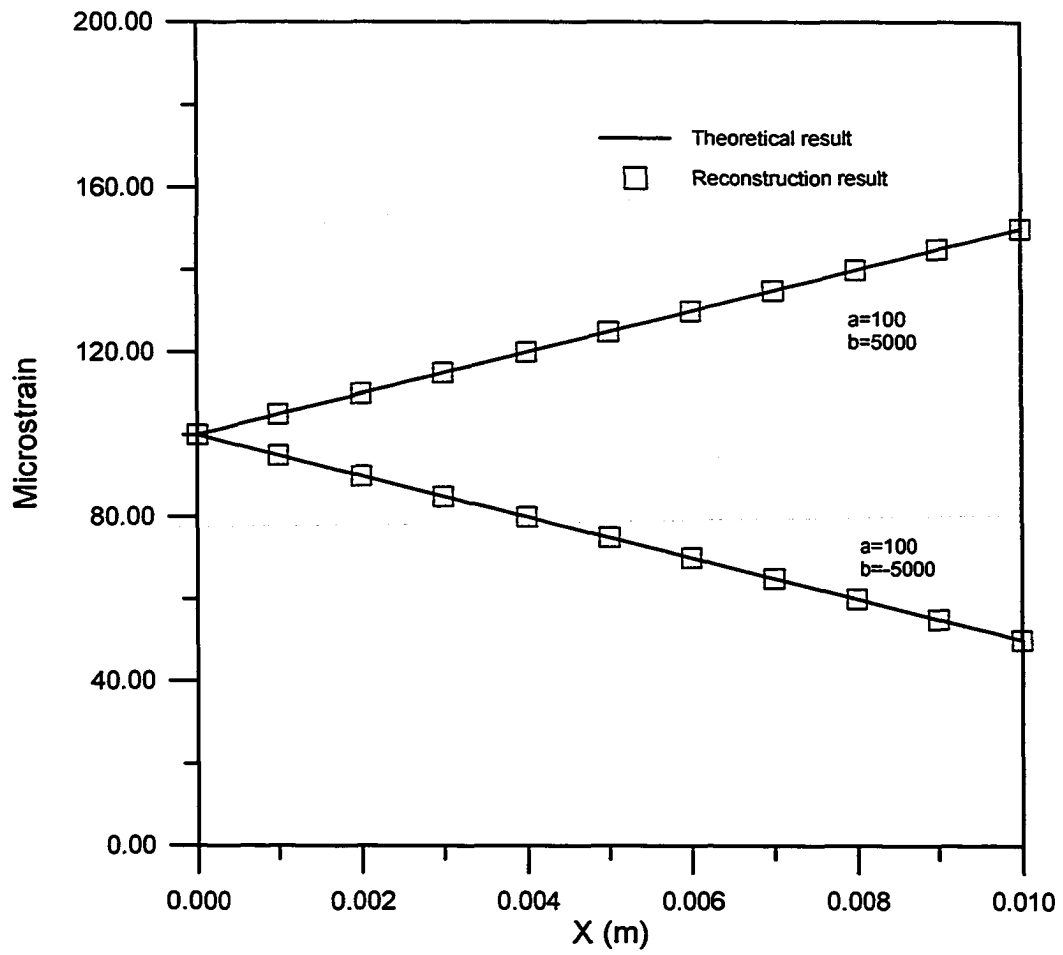


Fig. 4.6 Linear strain field reconstruction using Rayleigh waves of 1, 5, and 10 MHz.

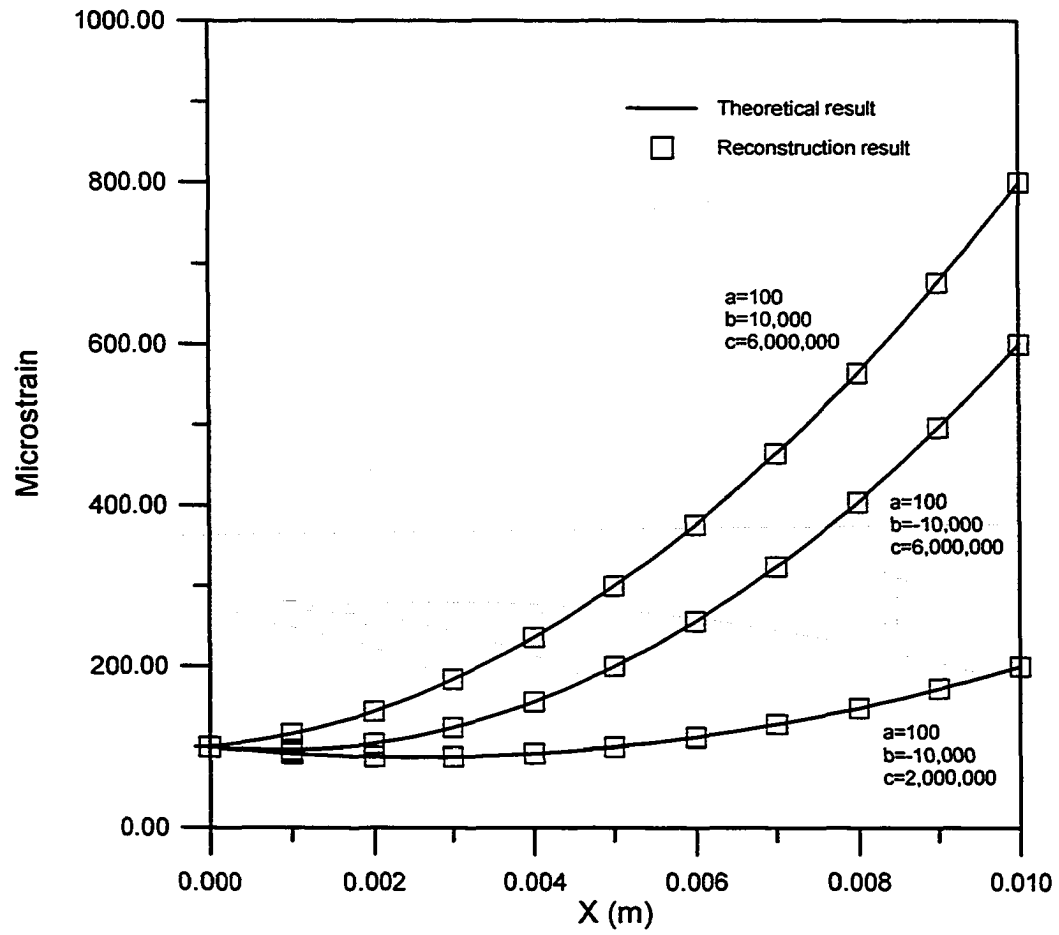


Fig. 4.7 Quadratic strain field reconstruction using Rayleigh waves of 1, 5, and 10 MHz.

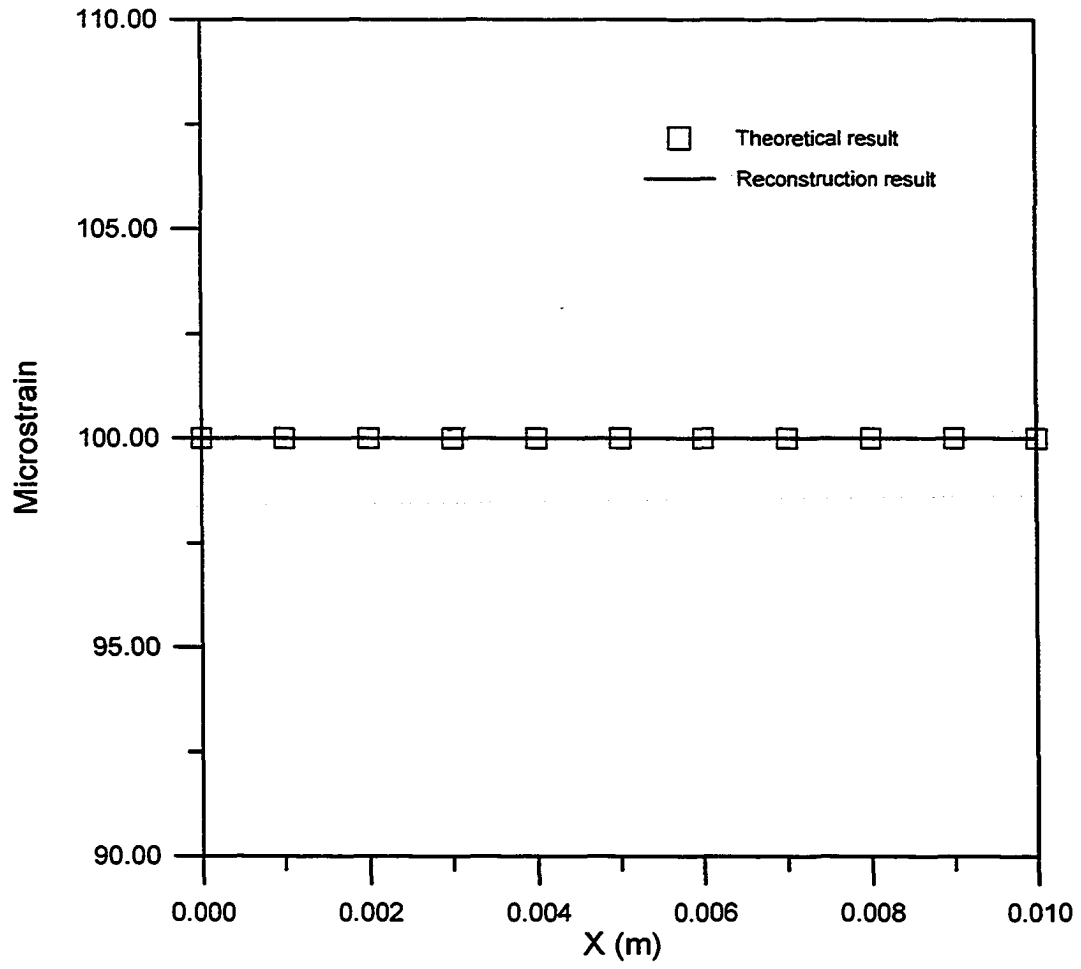


Fig. 4.8 Surface strain field reconstruction using Rayleigh waves of 2, 3, and 5 MHz.

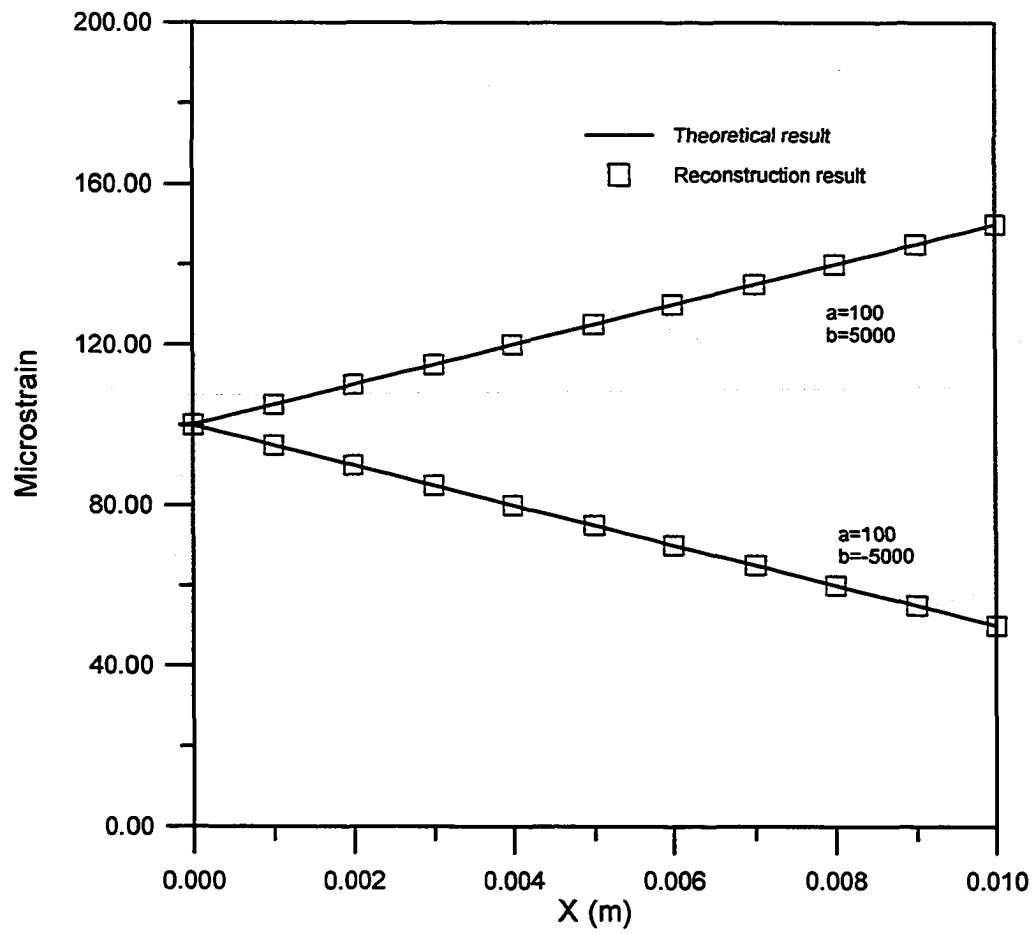


Fig. 4.9 Linear strain field reconstruction using Rayleigh waves of 2, 3, and 5 MHz.

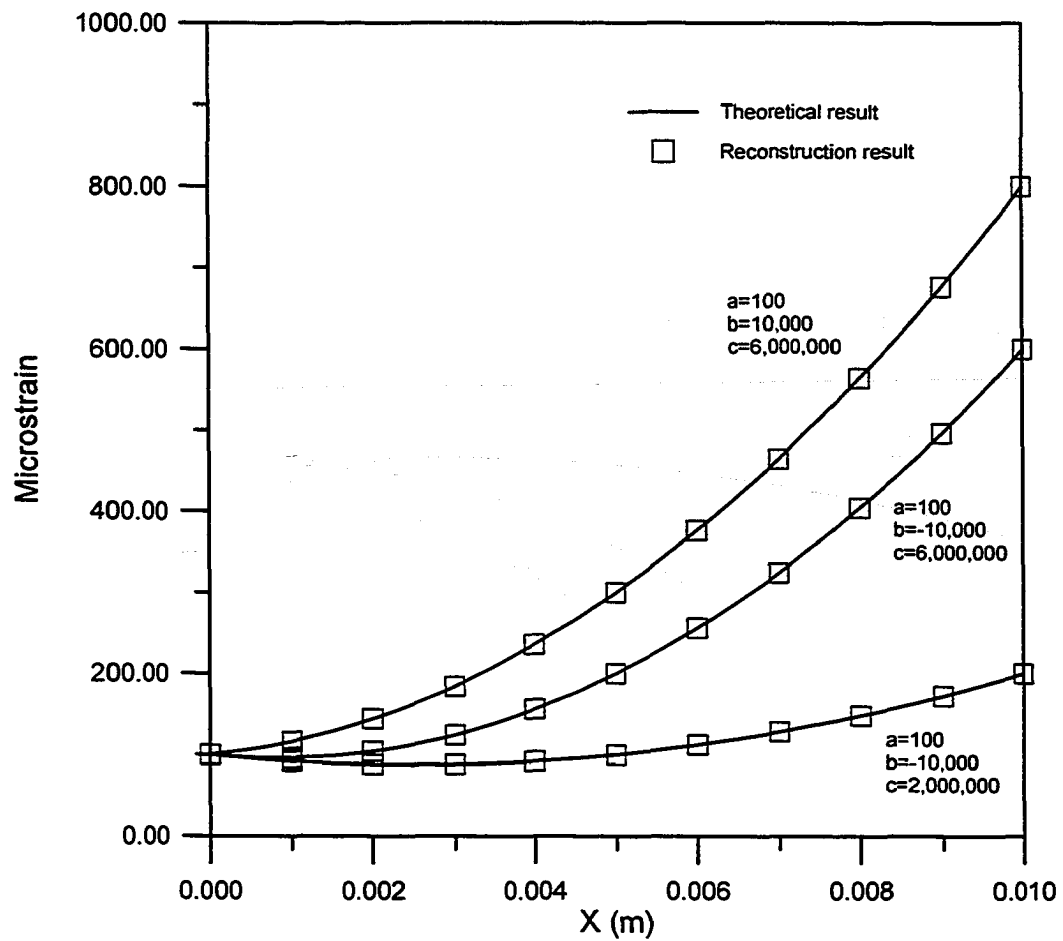


Fig. 4.10 Quadratic strain field reconstruction using Rayleigh waves of 2, 3, and 5 MHz.

4.3 Discussion

From equation (4-79), it is found that the extent of the Rayleigh wave dispersion is determined by the nature of the strain field and the Rayleigh wave frequency. This means that the details of the changes in the strain field with depth and the proper selection of the Rayleigh wave frequency will be crucial for this technique. For a uniform strain case, as $a_i = b_i = 0$, when $i > 0$, all the k terms will vanish in equation (4-79); thus, there will be no dispersion. This conclusion has been verified in Rayleigh wave acoustoelasticity. It should be noted that the lower the frequency of the Rayleigh waves, the higher the dispersion. Thus, low frequency Rayleigh waves are preferred for reconstruction purposes. In many problems, however, the sample thickness limits the frequencies which can be used. Since the penetration depth for Rayleigh waves is about equal to their wave length, care must be taken to ensure that the basic assumptions for surface wave propagation are still met. Generally speaking, there is no absolute half space in practice. Only if the sample thickness is much larger than the penetration depth can Rayleigh waves be well defined. The wave length of several different frequency Rayleigh waves propagating in the mild steel used for the simulation are listed in Table 4.2.

Fig. 4.2 shows the relative change of the Rayleigh wave speeds when the surface strains are different. The polynomial strain distribution pattern remains the same. The surface strains were assumed to be 100, 400, and 800 micro strain, respectively. It is seen that these three curves are almost parallel to each other and follow the same trend. Dispersion is prominent at low frequencies and diminishes as the frequency goes up. In

the high frequency range, the curves asymptotically approach a constant level as in the uniform strain case. This is due to the fact that the penetration depth of the Rayleigh waves is small; therefore, these waves are virtually insensitive to small changes in material properties with depth. An observation in Fig. 4.3 is that the relative change of the Rayleigh wave speed due to dispersion is small in comparison with the surface strain. If the surface strain difference is 300 micro strain, for example, as in the first two curves, the relative change of the Rayleigh wave speed will be $0.274 * 300 * 10^{-6} = 0.822 * 10^{-4}$. However, even when using very low frequency Rayleigh waves, the relative changes of speed are still less than $0.5 * 10^{-4}$ in each of the three cases.

Table 4.2 Wave lengths of Rayleigh waves corresponding to certain frequencies.

Resonant Frequency (MHz)	Wave Length (mm)
1	3.11
2	1.56
3	1.04
5	0.62
10	0.31

Fig. 4.3 and Fig. 4.4 reflect Rayleigh wave dispersion when only b (Fig. 4.3) and c (Fig. 4.4) are different, respectively, in equation (4-81). In Fig. 4.3, dispersion is obvious for frequencies below 5 MHz. Here, the three curves gradually approach to a constant after 10 MHz. This actually agrees with the conclusions drawn previously. As the frequency increases, the relatively change of the Rayleigh wave velocity is only affected by the strain at the surface, i.e., the coefficient a in equation (4-81). In Fig. 4.4, the curves show the same tendency as in Fig. 4.3. However, the threshold of the frequency at which dispersion begins to disappear reduces to about 5 MHz. It can be predicted that, for the higher order coefficient cases, the threshold frequencies that reflect the Rayleigh wave dispersion will become smaller and smaller.

Fig. 4.5 shows the surface strain reconstruction results using Rayleigh waves of 1, 5, and 10 MHz. Since there is no dispersion, the three different measurements give the same relative changes of the Rayleigh wave speeds, thus, b and c are zero. In Fig. 4.6, two different linear strain distributions are reconstructed with both quadratic coefficients set to zero. In Fig. 4.7, three different quadratic strain fields are reconstructed. In Fig. 4.8 to Fig. 4.10, using Rayleigh waves of 2, 3, and 5 MHz, the strain field reconstruction results are almost identical to those derived by using Rayleigh waves of 1, 5, and 10 MHz. These reconstruction results show satisfactory agreement with the theoretical strain distributions.

In order to determine the coefficients of the strain field as expressed in n th order polynomial form in equation (4-79), Rayleigh wave measurements for $2(n+1)$ different

frequencies are needed, and one must solve $2(n+1)$ linear equations. Two approaches can be used: exact or approximate. In order to avoid a singularity in the coefficient matrix, only one frequency beyond the threshold frequency can be selected to determine the surface strain at $X_2 = 0$. Fortunately, the frequency range of scanning acoustic microscopy can be easily adjusted to suit this limitation and the quadratic assumption for strain distribution is sufficiently accurate for many engineering applications.

Finally, as part of the theoretical study, let us consider equation (4-69) which represents the stress-free case to deduce the conventional equation for determining the velocity of the Rayleigh wave in an isotropic material. With the aid of equation (4-67), equation (4-69) yields

$$-(1+n_1^2)^2 n_2 (K-1)^2 + 4n_1 n_2^2 (K-1)^2 = 0 \quad (4-84)$$

The equation can be further simplified to

$$(1+n_1^2)^2 = 4n_1 n_2 \quad (4-85)$$

Substituting equations (4-29) to (4-31) into the above equation and taking the square of both sides, we have

$$(2 - \frac{V_0^2}{V_{T0}^2})^2 = 16(1 - \frac{V_0^2}{V_{T0}^2})(1 - \frac{\mu}{\lambda + 2\mu} \frac{V_0^2}{V_{T0}^2}) \quad (4-86)$$

After algebraic manipulation, we obtain

$$[(\frac{V_0^2}{V_{T0}^2})^6 - 8(\frac{V_0^2}{V_{T0}^2})^4 + 8\frac{3\lambda + 4\mu}{\lambda + 2\mu}(\frac{V_0^2}{V_{T0}^2})^2 - 16\frac{\lambda + \mu}{\lambda + 2\mu}](\frac{V_0^2}{V_{T0}^2}) = 0 \quad (4-87)$$

or

$$\left(\frac{V_0^2}{V_{T0}^2}\right)^6 - 8\left(\frac{V_0^2}{V_{T0}^2}\right)^4 + 8\frac{3\lambda + 4\mu}{\lambda + 2\mu}\left(\frac{V_0^2}{V_{T0}^2}\right)^2 - 16\frac{\lambda + \mu}{\lambda + 2\mu} = 0 \quad (4-88)$$

This is the familiar Rayleigh wave equation from basic elastic theory. It can be shown that only one of the six roots will meet the requirements for the Rayleigh wave from which the Rayleigh wave velocity can be derived.

CHAPTER V

CONCLUSIONS

In the previous chapters, two different ultrasonic approaches for in-plane stress analysis were introduced. In contrast to conventional acoustoelastic techniques, which measure stress-induced wave speed changes, the first approach, introduced in Chapter III employs a new concept, utilizing amplitude information of the ultrasonic wave to characterize in-plane stress. The theoretical study shows that the shear wave interference amplitude yields information about the difference of the principal stresses or, in other words, the maximum shear stress in the plane stress problem. The second approach, discussed in Chapter IV, is a surface wave technique based on the fact that an isotropic medium becomes dispersive for surface waves when subjected to a non-uniform strain or stress. Thus, different frequency surface waves can be utilized to characterize the stress or strain. Even though these two approaches fall into different categories in acoustoelasticity, two common points should be noted: (1) Both of the approaches employ scanning acoustic microscopy to avoid the coupling problems encountered in conventional acoustoelastic techniques and both are suitable for scanning purposes.

(2) First-order perturbation methods are successfully utilized to derive the phase velocities of shear waves and surface waves, respectively.

As far as the first amplitude approach was concerned, it was experimentally proven to be more sensitive than the conventional time delay measurement techniques [29]. However, lack of a sound theoretical base, or more specifically, the explanation of how the resulting scanning microscopy signal relates to the stress to be measured was missing. This study provides an analysis of the problem and quantitative comparisons between the model and experiments. The numerical simulation results are in good agreement with the scanning acoustic microscopy experimental results after a linear calibration. In an effort to provide more realistic stress or strain results in the simulation, a nonlinear FEA study with displacement controlled loading scheme was conducted. For the first-order perturbation approach to solve the Christoffel equations, this study followed a well-known procedure that is equivalent to expanding eigenvalues and eigenvectors into perturbation series due to the perturbation of the corresponding eigenvalue problem, and keeping the leading terms of these series. However, as the unperturbed medium was degenerated (the eigenvalues corresponding to the two shear waves were equal), special care had to be taken to derive the two quasi-shear wave velocities. It should be noted that although the unperturbed medium was degenerated, the specification of the polarization vectors was unique. It was controlled by the Christoffel tensor. This procedure was selected because of its mathematical conciseness and elegance.

The theoretical study of the Rayleigh wave dispersion approach was rather complicated and tedious because inhomogeneous strains in governing equations were considered. Even with a first-order perturbation approximation, the full expressions of the solution still appear to be cumbersome. However, formulas for the Rayleigh wave velocity change induced by nonuniform stress or strain in depthwise direction can be somewhat simplified after certain acoustoelastic constants are defined. From the Rayleigh wave dispersion plots, it was concluded that low frequency Rayleigh waves are preferred for stress reconstruction purposes. Care must be taken, however, to ensure the plate thickness to be large enough to avoid Rayleigh-Lamb type guided waves from being evoked. The simulation showed good results in reconstructing synthetic in-plane stress distributions from frequency dependent Rayleigh velocity data.

Obviously, the study of these two new acoustoelastic approaches remains in a preliminary stage. In the first approach, to simplify the problem, an axisymmetric assumption was imposed on the incident longitudinal wave and the two refracted shear waves had to be assumed of the same amplitude. A detailed algorithm for acoustic microscopy is also still unknown. All of the unknown factors have to be compensated for by linear calibration. In the second Rayleigh wave approach, experimental support is still missing to verify the theoretical predictions. Much more research is needed to mature the techniques into a practical residual stress measurement tool.

REFERENCES

1. D.S. Hughes and J.L. Kelly, "Second-Order Elastic Deformation of Solids", *Phys. Rev.*, Vol. 92, pp. 1145-1149, 1953.
2. R.A. Toupin and B. Bernstein, "Sound Waves in Deformed Perfectly Elastic Materials. Acoustoelastic Effect", *J. Acoust. Soc. Amer.*, Vol. 33, pp. 216-225, 1961.
3. R.N. Thurston and K. Brugger, "Third-Order Elastic Constants and the Velocity of Small-Amplitude Elastic Waves in Homogeneously Stressed Media", *Phys. Rev.*, Vol. 133, pp. 1604-1610, 1964.
4. Y. Iwashimizu and K. Kubomura, "Stress-Induced Rotation of Polarization Directions of Elastic Waves in Slightly Anisotropic Materials", *Int. J. Solids Struct.*, Vol. 9, pp. 99-114, 1973.
5. K. Okada, "Stress-Acoustic Relations for Stress Measurement by Ultrasonic Techniques", *J. Acoust. Soc. Jap. (E)*, Vol. 1, No. 3, pp. 193-200, 1980.
6. A.V. Clark and R.B. Mignogna, "A Comparison of Two Theories of Acoustoelasticity", *Ultrasonics*, Vol. 21, pp. 217-226, 1983.
7. A. Arora, "Ultrasonic Measurement of Residual Stress in Textured Materials", *J. Test. Eval.*, Vol. 10, No. 5, pp. 212-216, 1982.
8. R.B. King and C.M. Fortunko, "Determination of In-plane Residual Stress States in Plates Using Horizontally Polarized Shear Waves", *J. Appl. Phys.*, Vol. 54(6), pp. 3027-3035, 1983.

9. R.B. Thompson, J.F. Smith, and S.S. Lee, "Absolute Measurement of Stress in Textured Materials", *Rev. Progress in Quantitative Nondestructive Evaluation*, 2B, pp. 1339-1354, 1983.
10. D.R. Allen and C.M. Sayers, "The Measurement of Residual Stress in Textured Steel Using an Ultrasonic Velocity Combinations Technique", *Ultrasonics*, Vol. 22, No. 4, pp. 179-188, 1984.
11. D.M. Egle and A.M. Koshti, "Stress Measurement via the Acoustoelastic Effect and Water-coupled Ultrasonic Waves", Paper Presented at the Conference on Nondestructive Testing and Evaluation for Manufacturing and Construction, Univ. of Illinois, Urbana-Champaign, Illinois, Aug. 9-12, 1988.
12. A. Sinaie, "An Analytical Approach to Oblique Incidence Acoustoelasticity", Ph.D. Dissertation, University of Oklahoma, 1990.
13. G.C. Johnson, "Acoustoelastic Theory for Elastic-Plastic Materials", *J. Acoust. Soc. Amer.*, Vol. 70, pp. 591-595, 1981.
14. M. Kobayashi, "Analysis of Acoustic Phenomena in Elastic-Plastically Deformed Condition", *Trans. JSME. A* 48, No. 432, pp. 1072-1080, 1982.
15. Y. Pao, "Theory of Acoustoelasticity and Acoustoplasticity", *Solid Mechanics Research for Quantitative NDE*, Eds, J.D. Achenbach and Y. Rajapakse, Kluwer Academic Publishers, pp. 257-273, 1986.

16. R.H. Bergman and R.A. Shahbender, "Effect of Statically Applied Stresses on the Velocity of Propagation of Ultrasonic Waves", *J. Appl. Phys.*, Vol. 29, pp. 1736-1738, 1958.
17. R.W. Benson, and V.J. Raelson, "Acoustoelasticity", *Product Eng.*, Vol. 30, pp. 56-59, 1959.
18. R.A. Kline, "Wave Propagation in Fiber Reinforced Composites for Oblique Incidence", *J. Comp. Mat.*, Vol. 22, pp. 287-303, 1988.
19. D.I. Crecraft, "The Measurement of Applied and Residual Stresses in Metals Using Ultrasonic Waves", *J. Sound Vib.*, Vol. 5, pp. 173-192, 1967.
20. D.M. Egle and D.E. Bray, "Measurement of Acoustoelastic and Third-Order Elastic Constants for Rail Steel", *J. Acoust. Soc. Amer.*, Vol. 60, pp. 741-744, 1976.
21. A.V. Clark, "On the Use of Acoustic Birefringence to Determine Components of Plane Stress", *Ultrasonics.*, Vol. 23, pp. 21-30, 1985.
22. H. Fukuoka, H. Toda, and H. Naka, "Nondestructive Residual-Stress Measurement in a Wide-Flanged Rolled Beam by Acoustoelasticity", *Exp. Mech.*, Vol. 23, pp. 120-128, 1983.
23. K.C. Wu and L. Jiang, "An Acoustoelastic Method for Measuring Residual Stresses in Slightly Orthotropic Material", *Acta Mech. Solida Sinica*, Vol. 4, No. 4, pp. 355-362, 1991.

24. K.C. Wu and L. Jiang, "Two-Dimensional Acoustoelastic Analysis of Residual Stress in a Seam Welded Plate", *Proc. 6th Inter. Cong. Exp. Mech.*, pp. 509-511, U.S.A. 1988.
25. H. Toda "R-Value Acoustoelastic Analysis of Residual Stress in a Welded Plate", *J. Appl. Phys. Jap.*, Vol. 23, pp. 86-88, 1984.
26. G.S. Kino, "Acoustoelasticity", *Elastic Waves and Nondestructive Testing of Materials*, ASME Publication, AMD-29, 1978.
27. G.V. Blessing, N.N. Hsu and T.M. Proctor, "Ultrasonic Shear-Wave Measurement of Known Residual Stress in Aluminum", *Exp. Mech.*, Vol. 24, pp. 218-224, 1984.
28. E. Drescher-Krasicka, "Scanning Acoustic Imaging of Stress in the Interior of Solid Material", *J. Acoust. Soc. Amer.*, Vol. 94, No. 1, pp. 453-464, 1993.
29. E. Drescher-Krasicka and J.R. Willis, "Mapping Stress with Ultrasound", *Nature*, Vol. 384. No. 7, pp. 52-55, 1996.
30. M. Hayes and R. S. Rivlin, "Surface Waves in Deformed Elastic Materials", *Archive Mech.*, Vol. 8, pp. 358-380, 1961.
31. Y. Iwashimizu and O. Kobori, "The Rayleigh Wave in a Finitely Deformed Isotropic Elastic Material", *J. Acoust. Soc. Amer.*, Vol. 64, No. 3, pp. 910-916, 1978.
32. G.B. Martin, "Rayleigh-Wave Velocity, Stress and Preferred Grain Orientation in Aluminum", *Nondestructive Testing Inter.*, Vol. 32, pp. 199-203, 1974.
33. L. Adler, "The Relationship Between Ultrasonic Rayleigh Waves and Surface Residual Stress", *Mat. Eval.*, Vol. 35, pp. 93-96, 1977.

34. Y.C. Lee, J.O. Kim, and J.D. Achenbach, "Measurement of Stresses by Line-Focus Acoustic Microscopy", *Ultrasonics.*, Vol. 32, No. 5, pp. 359-365, 1994.
35. M. Hirao, H. Fukuoka, and K. Hori, "Acoustoelastic Effect of Rayleigh Surface Wave in Isotropic Material", *J. Appl. Mech.*, Vol. 48, pp. 119-124, 1981.
36. S.W. Meek, D. Peter, D. Horne, K. Young, and V. Novotny, "Microscopic Imaging of Residual Stress Using a Scanned Phase Measuring Acoustic Microscopy", *Appl. Phys. Lett.*, Vol. 55, pp. 1835-1837, 1989.
37. T. Narita, K. Miura, L. Ishikawa, and T. Ishikawa, "Measurement of Residual Thermal Stress and Its Distribution on Silicon Nitride Ceramics Jointed to Metals with Scanning Acoustic Microscopy", *J. Jap. Inst. Metals*, Vol. 54, pp. 1142-1146, 1990.
38. J. Jech and I. Psencik, "First-Order Perturbation Method for Anisotropic Media", *Geophys. J. Int.*, Vol. 99, pp. 369-376, 1989.
39. M.M. Frocht, *Photoelasticity*, Vol. II, Wiley, New York, 1948
40. A.C. Eringer and E.S. Suhubi, *Elastodynamics*, Academic Press, New York, 1974.
41. Y.H. Pao, W. Sachse, and H. Fukuoka "Acoustoelasticity and Ultrasonic Measurement of Residual Stresses", *Phy. Acous.*, Eds. W.P. Mason and R.N. Thurston, Academic Press, New York, Vol. 17, pp. 61-143, 1984.
42. R.A. Lemons and C.F. Quate, "Acoustic Microscopy", *Phy. Acous.*, Vol. 14, pp. 2-92, 1979.

43. B.T. Khuri-Yakub and P.A. Reinholdtsen, "QNDE Using Low-Frequency Acoustic Microscopy", *Solid Mechanics Research for Quantitative NDE*, Eds. J.D. Achenbach and Y. Rajapakse, Kluwer Academic Publishers, pp. 171-184, 1986.
44. H. Fukuoka, "Ultrasonic Measurement of Residual Stress", *Solid Mechanics Research for Quantitative NDE*, Eds. J.D. Achenbach and Y. Rajapakse, Kluwer Academic Publishers, pp. 275-299, 1986.
45. X. Zhao, "Experimental Investigation of the Separation of Texture and Residual Stress Induced Anisotropy Via Oblique Incidence Acoustoelasticity", Ph.D. Dissertation, University of Oklahoma, 1994.
46. K. Okada, "Acoustoelastic Stress Analysis on a Rolled Plate Under Plane Stress State", *Proc. Inter. Conf. Exp. Mech.*, pp. 584-589, Beijing, China, 1985.
47. A.V. Clark, "Acoustoelastic Measurement of Stress and Stress Intensity around Crack Tips", *Ultrasonics.*, Vol. 21, pp. 57-64, 1983.
48. A.V. Clark and H. Fukuoka, "Characterization of Residual Stress and Texture in Cast Steel Railroad Wheels", *Ultrasonics.*, Vol. 24, pp. 281-288, 1986.
49. R.A. Kline, L. Jiang, and E. Drescher-Krasicka, "Application of Scanning Acoustic Microscopy to Residual Stress Analysis: Theory vs. Experiment", *Review of Progress of Quantitative Nondestructive Evaluation*, Vol. 14, pp. 1907-1914, 1995.
50. L. Jiang, "Two-Dimensional Acoustoelastic Analysis of Residual Stress in a Seam Welded Slight Orthotropic Plate", Master's Thesis, Huazhong University of Science and Technology, 1988.

51. R.A. Kline, *Nondestructive Characterization of Composite Media*, Technomic Publishing Company, Inc., Lancaster, PA, 1992.
52. K.F. Graff, *Wave Motion in Elastic Solids*, Dover Publications, Inc., New York, 1991.
53. S.I. Rokhlin, T.K. Bolland, and L. Adler, "Reflection and Refraction of Elastic Wave on a Plane Interface Between Two Generally Anisotropic Media," *J. Acoust. Soc. Amer.*, Vol. 79, pp. 906-919, 1986.

APPENDIX A

RAYLEIGH WAVE DISPERSION EQUATIONS

If the strains in the thickness direction of a plane stress problem may be expressed in an n th order polynomial as in equation (4-73), the relative change of the Rayleigh wave velocities is obtained:

$$\begin{aligned} \Delta V / V_0 = & \beta_0 a_0 + \beta_1 a_1 / k + \beta_2 a_2 / k^2 + \beta_3 a_3 / k^3 + \dots + \beta_n a_n / k^n \\ & + \gamma_0 b_0 + \gamma_1 b_1 / k + \gamma_2 b_2 / k^2 + \gamma_3 b_3 / k^3 + \dots + \gamma_n b_n / k^n \end{aligned} \quad (\text{A} - 1)$$

where

$$\beta_0 = C_1 S_{10}^{(1)} + C_2 S_{20}^{(1)} + C_3 S_{30}^{(1)} + C_4 S_{40}^{(1)} \quad (\text{A} - 3)$$

$$\beta_1 = C_1 S_{11}^{(1)} + C_2 S_{21}^{(1)} + C_3 S_{31}^{(1)} + C_4 S_{41}^{(1)} \quad (\text{A} - 4)$$

$$\beta_2 = C_1 S_{12}^{(1)} + C_2 S_{22}^{(1)} + C_3 S_{32}^{(1)} + C_4 S_{42}^{(1)} \quad (\text{A} - 5)$$

$$\beta_3 = C_1 S_{13}^{(1)} + C_2 S_{23}^{(1)} + C_3 S_{33}^{(1)} + C_4 S_{43}^{(1)} \quad (\text{A} - 6)$$

$$\beta_n = C_1 S_{1n}^{(1)} + C_2 S_{2n}^{(1)} + C_3 S_{3n}^{(1)} + C_4 S_{4n}^{(1)} \quad (\text{A} - 7)$$

$$\gamma_0 = C_1 S_{10}^{(2)} + C_2 S_{20}^{(2)} + C_3 S_{30}^{(2)} + C_4 S_{40}^{(2)} \quad (\text{A} - 8)$$

$$\gamma_1 = C_1 S_{11}^{(2)} + C_2 S_{21}^{(2)} + C_3 S_{31}^{(2)} + C_4 S_{41}^{(2)} \quad (\text{A} - 9)$$

$$\gamma_2 = C_1 S_{12}^{(2)} + C_2 S_{22}^{(2)} + C_3 S_{32}^{(2)} + C_4 S_{42}^{(2)} \quad (\text{A} - 10)$$

$$\gamma_3 = C_1 S_{13}^{(2)} + C_2 S_{23}^{(2)} + C_3 S_{33}^{(2)} + C_4 S_{43}^{(2)} \quad (\text{A} - 11)$$

$$\gamma_n = C_1 S_{1n}^{(2)} + C_2 S_{2n}^{(2)} + C_3 S_{3n}^{(2)} + C_4 S_{4n}^{(2)} \quad (\text{A-12})$$

and

$$C_1 = -\left(\frac{V_{T0}^2}{2V_0^2}\right) \frac{G_{22}}{G_{11}a_{22} + G_{22}a_{11} - G_{12}a_{21} - G_{21}a_{12}} \quad (\text{A-13})$$

$$C_2 = -\left(\frac{V_{T0}^2}{2V_0^2}\right) \frac{G_{11}}{G_{11}a_{22} + G_{22}a_{11} - G_{12}a_{21} - G_{21}a_{12}} \quad (\text{A-14})$$

$$C_3 = \left(\frac{V_{T0}^2}{2V_0^2}\right) \frac{G_{21}}{G_{11}a_{22} + G_{22}a_{11} - G_{12}a_{21} - G_{21}a_{12}} \quad (\text{A-15})$$

$$C_4 = \left(\frac{V_{T0}^2}{2V_0^2}\right) \frac{G_{12}}{G_{11}a_{22} + G_{22}a_{11} - G_{12}a_{21} - G_{21}a_{12}} \quad (\text{A-16})$$

$$\begin{aligned} S_{10}^{(1)} = & U_{11}^{(1)} + h(K-1)n_2 \left\{ (1+n_1^2) \left[\frac{L_1^{(1)} + 2n_1 M_1^{(1)}}{2n_1} - M_1^{(1)} \right] \right. \\ & \left. - 2n_1 n_2 \left[\frac{L_1^{(1)} + (n_1 + n_2) M_1^{(1)}}{n_1 + n_2} - M_1^{(1)} \right] \right\} \end{aligned} \quad (\text{A-17})$$

$$\begin{aligned} S_{10}^{(2)} = & U_{11}^{(2)} + h(K-1)n_2 \left\{ (1+n_1^2) \left[\frac{L_1^{(2)} + 2n_1 M_1^{(2)}}{2n_1} - M_1^{(2)} \right] \right. \\ & \left. - 2n_1 n_2 \left[\frac{L_1^{(2)} + (n_1 + n_2) M_1^{(2)}}{n_1 + n_2} - M_1^{(2)} \right] \right\} \end{aligned} \quad (\text{A-18})$$

$$\begin{aligned} S_{11}^{(1)} = & V_{11}^{(1)} + h(K-1)n_2 \left\{ (1+n_1^2) \left[\frac{L_1^{(1)} + 2n_1 M_1^{(1)}}{4n_1^2} \right] \right. \\ & \left. - 2n_1 n_2 \left[\frac{L_1^{(1)} + (n_1 + n_2) M_1^{(1)}}{(n_1 + n_2)^2} \right] \right\} \end{aligned} \quad (\text{A-19})$$

$$\begin{aligned}
S_{11}^{(2)} = & V_{11}^{(2)} + h(K-1)n_2 \left\{ (1+n_1^2) \left[\frac{L_1^{(2)} + 2n_1 M_1^{(2)}}{4n_1^2} \right] \right. \\
& \left. - 2n_1 n_2 \left[\frac{L_1^{(2)} + (n_1 + n_2) M_1^{(2)}}{(n_1 + n_2)^2} \right] \right\}
\end{aligned} \tag{A-20}$$

$$\begin{aligned}
S_{12}^{(1)} = & W_{11}^{(1)} + h(K-1)n_2 \left\{ (1+n_1^2) \left[\frac{L_1^{(1)} + 2n_1 M_1^{(1)}}{4n_1^3} \right] \right. \\
& \left. - 4n_1 n_2 \left[\frac{L_1^{(1)} + (n_1 + n_2) M_1^{(1)}}{(n_1 + n_2)^3} \right] \right\}
\end{aligned} \tag{A-21}$$

$$\begin{aligned}
S_{12}^{(2)} = & W_{11}^{(2)} + h(K-1)n_2 \left\{ (1+n_1^2) \left[\frac{L_1^{(2)} + 2n_1 M_1^{(2)}}{4n_1^3} \right] \right. \\
& \left. - 4n_1 n_2 \left[\frac{L_1^{(2)} + (n_1 + n_2) M_1^{(2)}}{(n_1 + n_2)^3} \right] \right\}
\end{aligned} \tag{A-22}$$

$$\begin{aligned}
S_{13}^{(1)} = & h(K-1)n_2 \left\{ 3(1+n_1^2) \left[\frac{L_1^{(1)} + 2n_1 M_1^{(1)}}{8n_1^4} \right] \right. \\
& \left. - 12n_1 n_2 \left[\frac{L_1^{(1)} + (n_1 + n_2) M_1^{(1)}}{(n_1 + n_2)^4} \right] \right\}
\end{aligned} \tag{A-23}$$

$$\begin{aligned}
S_{13}^{(2)} = & h(K-1)n_2 \left\{ 3(1+n_1^2) \left[\frac{L_1^{(2)} + 2n_1 M_1^{(2)}}{8n_1^4} \right] \right. \\
& \left. - 12n_1 n_2 \left[\frac{L_1^{(2)} + (n_1 + n_2) M_1^{(2)}}{(n_1 + n_2)^4} \right] \right\}
\end{aligned} \tag{A-24}$$

$$\begin{aligned}
S_{1n}^{(1)} = & h(K-1)n_2 \left\{ (1+n_1^2) \frac{(L_1^{(1)} + 2n_1 M_1^{(1)})n!}{(2n_1)^{n+1}} \right. \\
& \left. - 2n_1 n_2 \frac{[L_1^{(1)} + (n_1 + n_2) M_1^{(1)}]n!}{(n_1 + n_2)^{n+1}} \right\}
\end{aligned} \tag{A-25}$$

$$S_{in}^{(2)} = h(K-1)n_2 \left\{ (1+n_1^2) \frac{(L_1^{(2)} + 2n_1 M_1^{(2)})n!}{(2n_1)^{n+1}} - 2n_1 n_2 \frac{[L_1^{(2)} + (n_1 + n_2)M_1^{(2)}]n!}{(n_1 + n_2)^{n+1}} \right\} \quad (\text{A-26})$$

$$S_{20}^{(1)} = U_{22}^{(1)} + h(K-1)n_1 n_2 \left\{ 2 \left[\frac{L_2^{(1)} + (n_1 + n_2)M_2^{(1)}}{n_1 + n_2} - M_2^{(1)} \right] - (1+n_1^2) \left[\frac{L_2^{(1)} + 2n_2 M_1^{(1)}}{2n_2} - M_2^{(1)} \right] \right\} \quad (\text{A-27})$$

$$S_{20}^{(2)} = U_{22}^{(2)} + h(K-1)n_1 n_2 \left\{ 2 \left[\frac{L_2^{(2)} + (n_1 + n_2)M_2^{(2)}}{n_1 + n_2} - M_2^{(2)} \right] - (1+n_1^2) \left[\frac{L_2^{(2)} + 2n_2 M_2^{(2)}}{2n_2} - M_2^{(2)} \right] \right\} \quad (\text{A-28})$$

$$S_{21}^{(1)} = V_{22}^{(1)} + h(K-1)n_1 n_2 \left\{ 2 \left[\frac{L_2^{(1)} + (n_1 + n_2)M_2^{(1)}}{(n_1 + n_2)^2} \right] - (1+n_1^2) \left[\frac{L_2^{(1)} + 2n_2 M_2^{(1)}}{4n_2^2} \right] \right\} \quad (\text{A-29})$$

$$S_{21}^{(2)} = V_{22}^{(2)} + h(K-1)n_1 n_2 \left\{ 2 \left[\frac{L_2^{(2)} + (n_1 + n_2)M_2^{(2)}}{(n_1 + n_2)^2} \right] - (1+n_1^2) \left[\frac{L_2^{(2)} + 2n_2 M_2^{(2)}}{4n_2^2} \right] \right\} \quad (\text{A-30})$$

$$S_{22}^{(1)} = W_{22}^{(1)} + h(K-1)n_1 n_2 \left\{ 4 \left[\frac{L_2^{(1)} + (n_1 + n_2)M_2^{(1)}}{(n_1 + n_2)^3} \right] - (1+n_1^2) \left[\frac{L_2^{(1)} + 2n_2 M_2^{(1)}}{4n_2^3} \right] \right\} \quad (\text{A-31})$$

$$S_{22}^{(2)} = W_{22}^{(2)} + h(K-1)n_1n_2 \left\{ 4 \left[\frac{L_2^{(2)} + (n_1 + n_2)M_2^{(2)}}{(n_1 + n_2)^3} \right] \right. \\ \left. - (1 + n_1^2) \left[\frac{L_2^{(2)} + 2n_2M_2^{(2)}}{4n_2^3} \right] \right\} \quad (\text{A-32})$$

$$S_{23}^{(1)} = h(K-1)n_1n_2 \left\{ 12 \left[\frac{L_2^{(1)} + (n_1 + n_2)M_2^{(1)}}{(n_1 + n_2)^4} \right] \right. \\ \left. - 3(1 + n_1^2) \left[\frac{L_2^{(1)} + 2n_2M_2^{(1)}}{8n_2^4} \right] \right\} \quad (\text{A-33})$$

$$S_{23}^{(2)} = h(K-1)n_1n_2 \left\{ 12 \left[\frac{L_2^{(2)} + (n_1 + n_2)M_2^{(2)}}{(n_1 + n_2)^4} \right] \right. \\ \left. - 3(1 + n_1^2) \left[\frac{L_2^{(2)} + 2n_2M_2^{(2)}}{8n_2^4} \right] \right\} \quad (\text{A-34})$$

$$S_{2n}^{(1)} = h(K-1)n_1n_2 \left\{ 2 \frac{(L_2^{(1)} + (n_1 + n_2)M_2^{(1)})n!}{(n_1 + n_2)^{n+1}} \right. \\ \left. - (1 + n_1^2) \frac{(L_2^{(1)} + 2n_2M_2^{(1)})n!}{(2n_2)^{n+1}} \right\} \quad (\text{A-35})$$

$$S_{2n}^{(2)} = h(K-1)n_1n_2 \left\{ 2 \frac{[L_2^{(2)} + (n_1 + n_2)M_2^{(2)}]n!}{(n_1 + n_2)^{n+1}} \right. \\ \left. - (1 + n_1^2) \frac{(L_2^{(2)} + 2n_2M_2^{(2)})n!}{(2n_2)^{n+1}} \right\} \quad (\text{A-36})$$

$$S_{30}^{(1)} = U_{12}^{(1)} + h(K-1)n_2 \left\{ (1 + n_1^2) \left[\frac{L_2^{(1)} + (n_1 + n_2)M_2^{(1)}}{n_1 + n_2} - M_2^{(1)} \right] \right. \\ \left. - 2n_1n_2 \left[\frac{L_2^{(1)} + 2n_2M_2^{(1)}}{2n_2} - M_2^{(1)} \right] \right\} \quad (\text{A-37})$$

$$\begin{aligned}
S_{30}^{(2)} = & U_{12}^{(2)} + h(K-1)n_2 \left\{ (1+n_1^2) \left[\frac{L_2^{(2)} + (n_1+n_2)M_2^{(2)}}{n_1+n_2} - M_2^{(2)} \right] \right. \\
& \left. - 2n_1n_2 \left[\frac{L_2^{(2)} + 2n_2M_2^{(2)}}{2n_2} - M_2^{(2)} \right] \right\}
\end{aligned} \tag{A-38}$$

$$\begin{aligned}
S_{31}^{(1)} = & V_{12}^{(1)} + h(K-1)n_2 \left\{ (1+n_1^2) \left[\frac{L_2^{(1)} + (n_1+n_2)M_2^{(1)}}{(n_1+n_2)^2} \right] \right. \\
& \left. - n_1 \left[\frac{L_2^{(1)} + 2n_2M_2^{(1)}}{2n_2} \right] \right\}
\end{aligned} \tag{A-39}$$

$$\begin{aligned}
S_{31}^{(2)} = & V_{12}^{(2)} + h(K-1)n_2 \left\{ (1+n_1^2) \left[\frac{L_2^{(2)} + (n_1+n_2)M_2^{(2)}}{(n_1+n_2)^2} \right] \right. \\
& \left. - n_1 \left[\frac{L_2^{(2)} + 2n_2M_2^{(2)}}{2n_2} \right] \right\}
\end{aligned} \tag{A-40}$$

$$\begin{aligned}
S_{32}^{(1)} = & W_{12}^{(1)} + h(K-1)n_2 \left\{ 2(1+n_1^2) \left[\frac{L_2^{(1)} + (n_1+n_2)M_2^{(1)}}{(n_1+n_2)^3} \right] \right. \\
& \left. - n_1 \left[\frac{L_2^{(1)} + 2n_2M_2^{(1)}}{2n_2^2} \right] \right\}
\end{aligned} \tag{A-41}$$

$$\begin{aligned}
S_{32}^{(2)} = & W_{12}^{(2)} + h(K-1)n_2 \left\{ 2(1+n_1^2) \left[\frac{L_2^{(2)} + (n_1+n_2)M_2^{(2)}}{(n_1+n_2)^3} \right] \right. \\
& \left. - n_1 \left[\frac{L_2^{(2)} + 2n_2M_2^{(2)}}{2n_2^2} \right] \right\}
\end{aligned} \tag{A-42}$$

$$\begin{aligned}
S_{33}^{(1)} = & h(K-1)n_2 \left\{ 6(1+n_1^2) \left[\frac{L_2^{(1)} + (n_1+n_2)M_2^{(1)}}{(n_1+n_2)^4} \right] \right. \\
& \left. - 3n_1 \left[\frac{L_2^{(1)} + 2n_2M_2^{(1)}}{4n_2^4} \right] \right\}
\end{aligned} \tag{A-43}$$

$$S_{33}^{(2)} = h(K-1)n_2 \{6(1+n_1^2) \left[\frac{L_2^{(2)} + (n_1+n_2)M_2^{(2)}}{(n_1+n_2)^4} \right] - 3n_1 \left[\frac{L_2^{(2)} + 2n_2 M_2^{(2)}}{4n_2^4} \right] \} \quad (\text{A-44})$$

$$S_{3n}^{(1)} = h(K-1)n_2 \{ (1+n_1^2) \frac{[L_2^{(1)} + (n_1+n_2)M_2^{(1)}]n!}{(n_1+n_2)^{n+1}} - n_1 \frac{(L_2^{(1)} + 2n_2 M_2^{(1)})n!}{(2n_2)^n} \} \quad (\text{A-45})$$

$$S_{3n}^{(2)} = h(K-1)n_2 \{ (1+n_1^2) \frac{[L_2^{(2)} + (n_1+n_2)M_2^{(2)}]n!}{(n_1+n_2)^{n+1}} - n_1 \frac{(L_2^{(2)} + 2n_2 M_2^{(2)})n!}{(2n_2)^n} \} \quad (\text{A-46})$$

$$S_{40}^{(1)} = U_{21}^{(1)} + h(K-1)n_1 n_2 \{ 2 \left[\frac{L_1^{(1)} + 2n_1 M_1^{(1)}}{2n_1} - M_1^{(1)} \right] - (1+n_1^2) \left[\frac{L_1^{(1)} + (n_1+n_2)M_1^{(1)}}{n_1+n_2} - M_1^{(1)} \right] \} \quad (\text{A-47})$$

$$S_{40}^{(2)} = U_{21}^{(2)} + h(K-1)n_1 n_2 \{ 2 \left[\frac{L_1^{(2)} + 2n_1 M_1^{(2)}}{2n_1} - M_1^{(2)} \right] - (1+n_1^2) \left[\frac{L_1^{(2)} + (n_1+n_2)M_1^{(2)}}{n_1+n_2} - M_1^{(2)} \right] \} \quad (\text{A-48})$$

$$S_{41}^{(1)} = V_{21}^{(1)} + h(K-1)n_2 \{ \left[\frac{L_1^{(1)} + 2n_1 M_1^{(1)}}{2n_1} \right] - (1+n_1^2) \left[\frac{L_1^{(1)} + (n_1+n_2)M_1^{(1)}}{(n_1+n_2)^2} \right] \} \quad (\text{A-49})$$

$$\begin{aligned}
S_{41}^{(2)} = & V_{21}^{(2)} + h(K-1)n_2 \left\{ \left[\frac{L_1^{(2)} + 2n_1 M_1^{(2)}}{2n_1} \right] \right. \\
& \left. - (1+n_1^2) \left[\frac{L_1^{(2)} + (n_1 + n_2) M_1^{(2)}}{(n_1 + n_2)^2} \right] \right\}
\end{aligned} \tag{A-50}$$

$$\begin{aligned}
S_{42}^{(1)} = & W_{21}^{(1)} + h(K-1)n_2 \left\{ \left[\frac{L_1^{(1)} + 2n_1 M_1^{(1)}}{2n_1^2} \right] \right. \\
& \left. - 2(1+n_1^2) \left[\frac{L_1^{(1)} + (n_1 + n_2) M_1^{(1)}}{(n_1 + n_2)^3} \right] \right\}
\end{aligned} \tag{A-51}$$

$$\begin{aligned}
S_{42}^{(2)} = & W_{21}^{(2)} + h(K-1)n_2 \left\{ \left[\frac{L_1^{(2)} + 2n_1 M_1^{(2)}}{2n_1^2} \right] \right. \\
& \left. - 2(1+n_1^2) \left[\frac{L_1^{(2)} + (n_1 + n_2) M_1^{(2)}}{(n_1 + n_2)^3} \right] \right\}
\end{aligned} \tag{A-52}$$

$$\begin{aligned}
S_{43}^{(1)} = & h(K-1)n_2 \left\{ 3 \left[\frac{L_1^{(1)} + 2n_1 M_1^{(1)}}{4n_1^3} \right] \right. \\
& \left. - 6(1+n_1^2) \left[\frac{L_1^{(1)} + (n_1 + n_2) M_1^{(1)}}{(n_1 + n_2)^4} \right] \right\}
\end{aligned} \tag{A-53}$$

$$\begin{aligned}
S_{43}^{(2)} = & h(K-1)n_2 \left\{ 3 \left[\frac{L_1^{(2)} + 2n_1 M_1^{(2)}}{4n_1^3} \right] \right. \\
& \left. - 6(1+n_1^2) \left[\frac{L_1^{(2)} + (n_1 + n_2) M_1^{(2)}}{(n_1 + n_2)^4} \right] \right\}
\end{aligned} \tag{A-54}$$

$$\begin{aligned}
S_{4n}^{(1)} = & h(K-1)n_2 \left\{ \frac{(L_1^{(1)} + 2n_1 M_1^{(1)})n!}{(2n_1)^n} \right. \\
& \left. - (1+n_1^2) \frac{[L_1^{(1)} + (n_1 + n_2) M_1^{(1)}]n!}{(n_1 + n_2)^{n+1}} \right\}
\end{aligned} \tag{A-55}$$

$$\begin{aligned}
S_{4n}^{(2)} = & h(K-1)n_2 \left\{ \frac{[L_2^{(2)} + 2n_1 M_2^{(2)}]n!}{(2n_1)^n} \right. \\
& \left. - (1+n_1^2) \frac{(L_2^{(2)} + (n_1+n_2)M_2^{(2)})n!}{(n_1+n_2)^{n+1}} \right\}
\end{aligned}
\tag{ A-56 }$$

APPENDIX B

STRESS RESULTS OF FEA SIMULATION

Along the transverse center line of the disk, the stress components for a 716 N compression load were:

NODE	SX	SY	SZ	SXY	SYZ	SXZ
2	-164.69	-293.05	.00000	4.2739	.00000	.00000
43	-141.11	-287.85	.00000	8.6066	.00000	.00000
44	-82.167	-265.66	.00000	24.109	.00000	.00000
45	-20.373	-222.62	.00000	27.750	.00000	.00000
46	-5.6094	-179.78	.00000	18.516	.00000	.00000
47	-.49097	-146.42	.00000	13.630	.00000	.00000
48	1.7352	-120.54	.00000	9.8830	.00000	.00000
49	2.7717	-101.08	.00000	7.2719	.00000	.00000
50	3.2762	-86.268	.00000	5.4721	.00000	.00000
51	3.5329	-74.724	.00000	4.2080	.00000	.00000
52	3.6674	-65.537	.00000	3.3015	.00000	.00000
53	3.7394	-58.082	.00000	2.6363	.00000	.00000
54	3.7784	-51.930	.00000	2.1381	.00000	.00000
55	3.7995	-46.778	.00000	1.7576	.00000	.00000
56	3.8106	-42.410	.00000	1.4621	.00000	.00000
57	3.8161	-38.667	.00000	1.2292	.00000	.00000
58	3.8185	-35.429	.00000	1.0430	.00000	.00000
59	3.8191	-32.605	.00000	.89243	.00000	.00000
60	3.8189	-30.124	.00000	.76965	.00000	.00000
61	3.8182	-27.932	.00000	.66924	.00000	.00000
62	3.8170	-25.985	.00000	.58706	.00000	.00000
63	3.8154	-24.250	.00000	.51911	.00000	.00000
64	3.8139	-22.697	.00000	.46147	.00000	.00000
65	3.8128	-21.304	.00000	.41137	.00000	.00000
66	3.8119	-20.049	.00000	.36720	.00000	.00000
67	3.8113	-18.916	.00000	.32799	.00000	.00000
68	3.8107	-17.894	.00000	.29298	.00000	.00000
69	3.8101	-16.969	.00000	.26154	.00000	.00000
70	3.8095	-16.134	.00000	.23313	.00000	.00000
71	3.8089	-15.380	.00000	.20731	.00000	.00000
72	3.8083	-14.702	.00000	.18367	.00000	.00000
73	3.8076	-14.094	.00000	.16188	.00000	.00000
74	3.8069	-13.552	.00000	.14161	.00000	.00000
75	3.8061	-13.072	.00000	.12258	.00000	.00000
76	3.8053	-12.654	.00000	.10451	.00000	.00000
77	3.8044	-12.295	.00000	.08713	.00000	.00000
78	3.8035	-11.996	.00000	.07015	.00000	.00000
79	3.8027	-11.757	.00000	.05325	.00000	.00000
80	3.8019	-11.581	.00000	.03614	.00000	.00000
81	3.8013	-11.472	.00000	.01849	.00000	.00000
42	3.8010	-11.434	.00000	.09249	.00000	.00000

The stress components for a 910 N compression load were:

NODE	SX	SY	SZ	SXY	SYZ	SEX
2	-170.28	-293.73	.00000	6.1470	.00000	.00000
43	-154.82	-289.25	.00000	7.7561	.00000	.00000
44	-102.30	-270.92	.00000	19.444	.00000	.00000
45	-35.422	-235.28	.00000	23.887	.00000	.00000
46	-14.423	-198.11	.00000	17.614	.00000	.00000
47	-5.9755	-166.29	.00000	13.710	.00000	.00000
48	-1.6083	-140.15	.00000	10.371	.00000	.00000
49	.80883	-119.67	.00000	7.8933	.00000	.00000
50	2.2177	-103.54	.00000	6.1016	.00000	.00000
51	3.0772	-90.638	.00000	4.7947	.00000	.00000
52	3.6215	-80.147	.00000	3.8279	.00000	.00000
53	3.9774	-71.488	.00000	3.1001	.00000	.00000
54	4.2166	-64.242	.00000	2.5432	.00000	.00000
55	4.3811	-58.107	.00000	2.1104	.00000	.00000
56	4.4966	-52.857	.00000	1.7693	.00000	.00000
57	4.5792	-48.323	.00000	1.4970	.00000	.00000
58	4.6392	-44.376	.00000	1.2771	.00000	.00000
59	4.6833	-40.915	.00000	1.0977	.00000	.00000
60	4.7164	-37.863	.00000	.95030	.00000	.00000
61	4.7414	-35.155	.00000	.82901	.00000	.00000
62	4.7600	-32.742	.00000	.72923	.00000	.00000
63	4.7739	-30.585	.00000	.64636	.00000	.00000
64	4.7847	-28.651	.00000	.57578	.00000	.00000
65	4.7934	-26.912	.00000	.51418	.00000	.00000
66	4.8004	-25.343	.00000	.45968	.00000	.00000
67	4.8061	-23.925	.00000	.41114	.00000	.00000
68	4.8107	-22.642	.00000	.36769	.00000	.00000
69	4.8142	-21.482	.00000	.32857	.00000	.00000
70	4.8170	-20.433	.00000	.29314	.00000	.00000
71	4.8192	-19.485	.00000	.26088	.00000	.00000
72	4.8207	-18.631	.00000	.23129	.00000	.00000
73	4.8218	-17.865	.00000	.20397	.00000	.00000
74	4.8225	-17.182	.00000	.17852	.00000	.00000
75	4.8228	-16.577	.00000	.15460	.00000	.00000
76	4.8228	-16.049	.00000	.13187	.00000	.00000
77	4.8226	-15.597	.00000	.10997	.00000	.00000
78	4.8221	-15.219	.00000	.08856	.00000	.00000
79	4.8216	-14.917	.00000	.06724	.00000	.00000
80	4.8210	-14.695	.00000	.04564	.00000	.00000
81	4.8204	-14.557	.00000	.02336	.00000	.00000
42	4.8201	-14.510	.00000	.01168	.00000	.00000

The stress components for a 1110 N compression load were:

NODE	SX	SY	SZ	SXY	SYZ	SXZ
2	-161.48	-301.83	.00000	2.0002	.00000	.00000
43	-152.97	-299.29	.00000	4.5636	.00000	.00000
44	-142.75	-290.39	.00000	9.0460	.00000	.00000
45	-87.965	-270.41	.00000	18.284	.00000	.00000
46	-23.957	-235.54	.00000	20.596	.00000	.00000
47	-7.8874	-202.73	.00000	15.144	.00000	.00000
48	-1.3279	-175.57	.00000	12.369	.00000	.00000
49	2.0272	-151.30	.00000	9.9463	.00000	.00000
50	3.7824	-131.00	.00000	7.8173	.00000	.00000
51	4.7259	-114.48	.00000	6.1857	.00000	.00000
52	5.2449	-100.96	.00000	4.9396	.00000	.00000
53	5.5381	-89.798	.00000	3.9911	.00000	.00000
54	5.7071	-80.478	.00000	3.2624	.00000	.00000
55	5.8064	-72.614	.00000	2.6966	.00000	.00000
56	5.8654	-65.911	.00000	2.2519	.00000	.00000
57	5.9007	-60.144	.00000	1.8984	.00000	.00000
58	5.9219	-55.142	.00000	1.6142	.00000	.00000
59	5.9345	-50.771	.00000	1.3833	.00000	.00000
60	5.9420	-46.926	.00000	1.1944	.00000	.00000
61	5.9462	-43.524	.00000	1.0395	.00000	.00000
62	5.9480	-40.500	.00000	.91249	.00000	.00000
63	5.9481	-37.802	.00000	.80732	.00000	.00000
64	5.9476	-35.388	.00000	.71802	.00000	.00000
65	5.9471	-33.219	.00000	.64030	.00000	.00000
66	5.9468	-31.266	.00000	.57172	.00000	.00000
67	5.9464	-29.503	.00000	.51080	.00000	.00000
68	5.9460	-27.910	.00000	.45637	.00000	.00000
69	5.9455	-26.470	.00000	.40747	.00000	.00000
70	5.9448	-25.169	.00000	.36327	.00000	.00000
71	5.9441	-23.995	.00000	.32307	.00000	.00000
72	5.9432	-22.938	.00000	.28627	.00000	.00000
73	5.9423	-21.990	.00000	.25232	.00000	.00000
74	5.9412	-21.145	.00000	.22075	.00000	.00000
75	5.9400	-20.398	.00000	.19110	.00000	.00000
76	5.9388	-19.745	.00000	.16295	.00000	.00000
77	5.9374	-19.186	.00000	.13585	.00000	.00000
78	5.9361	-18.719	.00000	.01093	.00000	.00000
79	5.9348	-18.347	.00000	.08304	.00000	.00000
80	5.9336	-18.072	.00000	.05636	.00000	.00000
81	5.9327	-17.902	.00000	.02884	.00000	.00000
42	5.9321	-17.844	.00000	.01442	.00000	.00000

The stress components for a 1310 N compression load were:

NODE	SX	SY	SZ	SXY	SYZ	SXZ
2	-171.64	-302.27	.00000	1.7106	.00000	.00000
43	-163.22	-299.76	.00000	4.6544	.00000	.00000
44	-149.63	-291.54	.00000	8.0105	.00000	.00000
45	-102.94	-274.78	.00000	15.399	.00000	.00000
46	-37.525	-245.34	.00000	18.092	.00000	.00000
47	-15.668	-215.79	.00000	14.321	.00000	.00000
48	-6.8589	-190.05	.00000	11.975	.00000	.00000
49	-1.7060	-166.48	.00000	9.9454	.00000	.00000
50	1.3554	-146.12	.00000	8.0267	.00000	.00000
51	3.2368	-129.11	.00000	6.4925	.00000	.00000
52	4.4281	-114.88	.00000	5.2814	.00000	.00000
53	5.2059	-102.92	.00000	4.3337	.00000	.00000
54	5.7273	-92.781	.00000	3.5886	.00000	.00000
55	6.0853	-84.117	.00000	2.9985	.00000	.00000
56	6.3361	-76.653	.00000	2.5270	.00000	.00000
57	6.5151	-70.174	.00000	2.1467	.00000	.00000
58	6.6449	-64.513	.00000	1.8371	.00000	.00000
59	6.7405	-59.533	.00000	1.5830	.00000	.00000
60	6.8120	-55.130	.00000	1.3731	.00000	.00000
61	6.8658	-51.216	.00000	1.1998	.00000	.00000
62	6.9064	-47.724	.00000	1.0568	.00000	.00000
63	6.9370	-44.598	.00000	.93777	.00000	.00000
64	6.9606	-41.792	.00000	.83614	.00000	.00000
65	6.9795	-39.265	.00000	.74727	.00000	.00000
66	6.9947	-36.985	.00000	.66850	.00000	.00000
67	7.0069	-34.923	.00000	.59824	.00000	.00000
68	7.0167	-33.056	.00000	.53527	.00000	.00000
69	7.0244	-31.367	.00000	.47851	.00000	.00000
70	7.0305	-29.839	.00000	.42707	.00000	.00000
71	7.0352	-28.458	.00000	.38018	.00000	.00000
72	7.0388	-27.213	.00000	.33715	.00000	.00000
73	7.0415	-26.097	.00000	.29739	.00000	.00000
74	7.0433	-25.100	.00000	.26034	.00000	.00000
75	7.0444	-24.219	.00000	.22549	.00000	.00000
76	7.0450	-23.449	.00000	.19236	.00000	.00000
77	7.0451	-22.788	.00000	.16044	.00000	.00000
78	7.0449	-22.237	.00000	.12921	.00000	.00000
79	7.0443	-21.797	.00000	.09812	.00000	.00000
80	7.0436	-21.473	.00000	.06661	.00000	.00000
81	7.0429	-21.272	.00000	.03408	.00000	.00000
42	7.0425	-21.203	.00000	.01705	.00000	.00000

The stress components for a 1510 N compression load were:

NODE	SX	SY	SZ	SXY	SYZ	SXZ
2	-181.18	-302.11	.00000	1.5236	.00000	.00000
43	-172.53	-299.78	.00000	4.5159	.00000	.00000
44	-155.02	-292.50	.00000	6.9338	.00000	.00000
45	-115.85	-278.67	.00000	12.353	.00000	.00000
46	-52.826	-255.52	.00000	16.010	.00000	.00000
47	-23.008	-228.49	.00000	13.790	.00000	.00000
48	-12.444	-203.26	.00000	11.488	.00000	.00000
49	-5.5568	-180.56	.00000	9.8348	.00000	.00000
50	-1.1863	-160.37	.00000	8.1603	.00000	.00000
51	1.6493	-143.03	.00000	6.7451	.00000	.00000
52	3.5295	-128.21	.00000	5.5850	.00000	.00000
53	4.8052	-115.54	.00000	4.6484	.00000	.00000
54	5.6889	-104.65	.00000	3.8938	.00000	.00000
55	6.3128	-95.234	.00000	3.2843	.00000	.00000
56	6.7607	-87.050	.00000	2.7893	.00000	.00000
57	7.0871	-79.892	.00000	2.3846	.00000	.00000
58	7.3283	-73.597	.00000	2.0515	.00000	.00000
59	7.5088	-68.033	.00000	1.7755	.00000	.00000
60	7.6456	-63.091	.00000	1.5459	.00000	.00000
61	7.7502	-58.683	.00000	1.3550	.00000	.00000
62	7.8303	-54.737	.00000	1.1967	.00000	.00000
63	7.8918	-51.195	.00000	1.0642	.00000	.00000
64	7.9400	-48.010	.00000	.95073	.00000	.00000
65	7.9785	-45.136	.00000	.85108	.00000	.00000
66	8.0095	-42.538	.00000	.76245	.00000	.00000
67	8.0344	-40.185	.00000	.68317	.00000	.00000
68	8.0545	-38.054	.00000	.61190	.00000	.00000
69	8.0705	-36.122	.00000	.54753	.00000	.00000
70	8.0834	-34.372	.00000	.48906	.00000	.00000
71	8.0937	-32.791	.00000	.43567	.00000	.00000
72	8.1017	-31.365	.00000	.38659	.00000	.00000
73	8.1080	-30.084	.00000	.34118	.00000	.00000
74	8.1128	-28.941	.00000	.29881	.00000	.00000
75	8.1163	-27.929	.00000	.25892	.00000	.00000
76	8.1187	-27.045	.00000	.22094	.00000	.00000
77	8.1202	-26.286	.00000	.18433	.00000	.00000
78	8.1210	-25.652	.00000	.14849	.00000	.00000
79	8.1213	-25.147	.00000	.11278	.00000	.00000
80	8.1211	-24.774	.00000	.07657	.00000	.00000
81	8.1206	-24.543	.00000	.03918	.00000	.00000
42	8.1202	-24.463	.00000	.01961	.00000	.00000

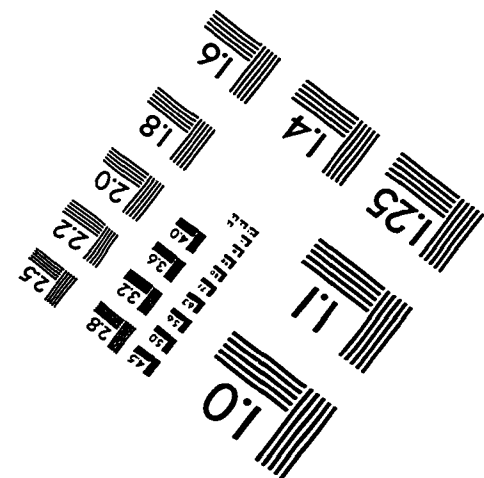
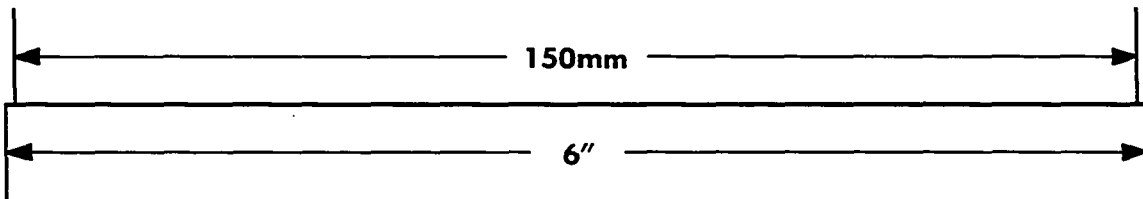
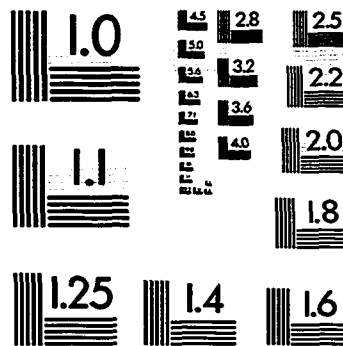
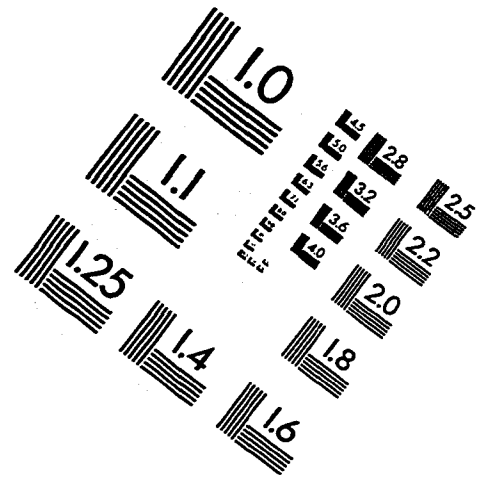
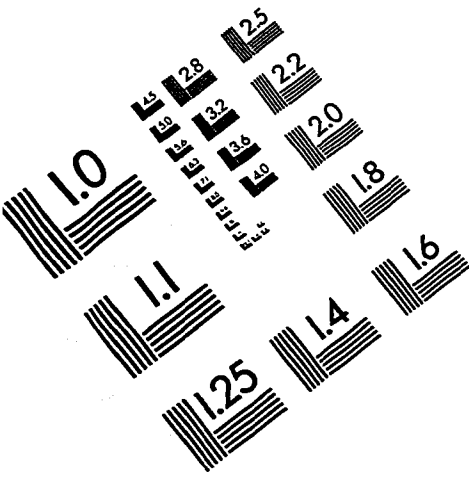
The stress components for a 1700 N compression load were:

NODE	SX	SY	SZ	SXY	SYZ	SXZ
2	-189.39	-301.46	.00000	1.6353	.00000	.00000
43	-180.25	-299.47	.00000	4.0669	.00000	.00000
44	-159.01	-293.39	.00000	5.8341	.00000	.00000
45	-128.81	-282.36	.00000	10.218	.00000	.00000
46	-67.373	-263.89	.00000	13.932	.00000	.00000
47	-30.246	-239.61	.00000	13.062	.00000	.00000
48	-18.171	-215.17	.00000	10.898	.00000	.00000
49	-9.5643	-193.57	.00000	9.6211	.00000	.00000
50	-3.8620	-173.75	.00000	8.2280	.00000	.00000
51	-.04899	-156.22	.00000	6.9509	.00000	.00000
52	2.5391	-140.92	.00000	5.8548	.00000	.00000
53	4.3266	-127.61	.00000	4.9377	.00000	.00000
54	5.5827	-116.02	.00000	4.1795	.00000	.00000
55	6.4796	-105.90	.00000	3.5545	.00000	.00000
56	7.1296	-97.037	.00000	3.0388	.00000	.00000
57	7.6070	-89.233	.00000	2.6119	.00000	.00000
58	7.9621	-82.334	.00000	2.2570	.00000	.00000
59	8.2294	-76.209	.00000	1.9604	.00000	.00000
60	8.4328	-70.750	.00000	1.7119	.00000	.00000
61	8.5889	-65.866	.00000	1.5043	.00000	.00000
62	8.7093	-61.483	.00000	1.3313	.00000	.00000
63	8.8024	-57.542	.00000	1.1861	.00000	.00000
64	8.8755	-53.991	.00000	1.0611	.00000	.00000
65	8.9339	-50.783	.00000	.95112	.00000	.00000
66	8.9808	-47.879	.00000	.85300	.00000	.00000
67	9.0186	-45.246	.00000	.76501	.00000	.00000
68	9.0490	-42.858	.00000	.68576	.00000	.00000
69	9.0736	-40.693	.00000	.61404	.00000	.00000
70	9.0933	-38.731	.00000	.54880	.00000	.00000
71	9.1091	-36.956	.00000	.48914	.00000	.00000
72	9.1217	-35.354	.00000	.43424	.00000	.00000
73	9.1316	-33.915	.00000	.38337	.00000	.00000
74	9.1393	-32.631	.00000	.33587	.00000	.00000
75	9.1452	-31.493	.00000	.29112	.00000	.00000
76	9.1495	-30.499	.00000	.24848	.00000	.00000
77	9.1525	-29.645	.00000	.20735	.00000	.00000
78	9.1543	-28.933	.00000	.16706	.00000	.00000
79	9.1554	-28.364	.00000	.12690	.00000	.00000
80	9.1557	-27.945	.00000	.08616	.00000	.00000
81	9.1555	-27.684	.00000	.04409	.00000	.00000
42	9.1551	-27.595	.00000	.02207	.00000	.00000

The coordinates of the listed nodes were as follows:

NODE	X	Y	Z	THXY	THYZ	THZX
2	.12246E-14	20.000	.00000	.00	.00	.00
43	.12124E-14	19.800	.00000	.00	.00	.00
44	.11996E-14	19.591	.00000	.00	.00	.00
45	.11863E-14	19.374	.00000	.00	.00	.00
46	.11724E-14	19.148	.00000	.00	.00	.00
47	.11580E-14	18.911	.00000	.00	.00	.00
48	.11429E-14	18.666	.00000	.00	.00	.00
49	.11272E-14	18.409	.00000	.00	.00	.00
50	.11109E-14	18.142	.00000	.00	.00	.00
51	.10938E-14	17.864	.00000	.00	.00	.00
52	.10761E-14	17.574	.00000	.00	.00	.00
53	.10576E-14	17.271	.00000	.00	.00	.00
54	.10383E-14	16.956	.00000	.00	.00	.00
55	.10182E-14	16.628	.00000	.00	.00	.00
56	.99720E-15	16.286	.00000	.00	.00	.00
57	.97536E-15	15.929	.00000	.00	.00	.00
58	.95261E-15	15.557	.00000	.00	.00	.00
59	.92889E-15	15.170	.00000	.00	.00	.00
60	.90418E-15	14.766	.00000	.00	.00	.00
61	.87842E-15	14.346	.00000	.00	.00	.00
62	.85158E-15	13.907	.00000	.00	.00	.00
63	.82361E-15	13.451	.00000	.00	.00	.00
64	.79446E-15	12.975	.00000	.00	.00	.00
65	.76409E-15	12.478	.00000	.00	.00	.00
66	.73243E-15	11.961	.00000	.00	.00	.00
67	.69944E-15	11.423	.00000	.00	.00	.00
68	.66506E-15	10.861	.00000	.00	.00	.00
69	.62923E-15	10.276	.00000	.00	.00	.00
70	.59189E-15	9.6663	.00000	.00	.00	.00
71	.55298E-15	9.0308	.00000	.00	.00	.00
72	.51242E-15	8.3685	.00000	.00	.00	.00
73	.47016E-15	7.6783	.00000	.00	.00	.00
74	.42612E-15	6.9591	.00000	.00	.00	.00
75	.38023E-15	6.2096	.00000	.00	.00	.00
76	.33240E-15	5.4284	.00000	.00	.00	.00
77	.28255E-15	4.6144	.00000	.00	.00	.00
78	.23061E-15	3.7661	.00000	.00	.00	.00
79	.17647E-15	2.8820	.00000	.00	.00	.00
80	.12006E-15	1.9607	.00000	.00	.00	.00
81	.61268E-16	1.0006	.00000	.00	.00	.00
42	.00000	.00000	.00000	.00	.00	.00

IMAGE EVALUATION TEST TARGET (QA-3)



APPLIED IMAGE, Inc
1653 East Main Street
Rochester, NY 14609 USA
Phone: 716/482-0300
Fax: 716/288-5989

© 1993, Applied Image, Inc., All Rights Reserved

